INVESTIGATION IN TO THE USE OF THERMOPLASTIC NANOCHANNELS FOR TIME OF FLIGHT (TOF) DETECTION OF NUCLEOTIDE MONOPHOSPHATES: TOWARDS SINGLE MOLECULE DNA SEQUENCING

Colleen Erin O'Neil

A dissertation submitted to the faculty at the University of North Carolina at Chapel Hill in partial fulfillment of the requirements for the degree of Doctor of Philosophy in the Department of Chemistry (Analytical) in the College of Arts and Sciences

Chapel Hill
2016

Approved by:

Steven A. Soper

James W. Jorgenson

Mathew Lockett

Frances Ligler

Shawn Gomez

ABSTRACT

Because of the unique properties that arise when the column size is comparable to either the length scale of electrostatic interactions or the size of the molecules being transported through them, nanochannel-based devices have garnered attention for many applications, especially nanoelectrophoresis. One essential application looking to exploit unique phenomena that occur at the nanoscale is Single Molecule Sequencing (SMS). SMS offers advantages over conventional ensemble-based sequencing platforms. Our proposed SMS device looks to identify nucleotides based on their molecular-dependent flight times as they migrate through a nanochannel, termed Time-of-Flight (ToF) detection. This research looked to understand the use of thermoplastic substrates for the fabrication of nanochannels to utilize in nanoelectrophoresis experiments for ToF detection. Differences in the migration properties of dNMPs under varying pH, buffer additives and buffer concentration to enhance the resolution of the separation and ultimately result in a high base calling accuracy were explored as well. Super Resolution Fluorescence data indicated non-uniform distributions of -COOH functional groups for both COC and PMMA thermoplastics with the degree of heterogeneity being dose dependent. In addition, COC demonstrated relative higher surface density of functional groups compared to PMMA for both UV/O_3 and O_2 plasma treatment. The spatial distribution of -COOH groups secured from super-resolution imaging were used to simulate non-uniform patterns of electroosmotic flow in thermoplastic nanochannels. Simulations were compared to single-particle tracking of fluorescent nanoparticles within thermoplastic nanoslits to demonstrate the effects of surface functional group heterogeneity on the electrokinetic transport process. Furthermore, results showed that increased norbornene content within COC led to the generation of more oxygen containing functionalities such as alcohols, ketones, aldehydes and carboxyl groups when activated with either

UV/O_3 or O_2 plasma. Specifically, COC 6017 (~60% norbornene content) showed a significantly higher –COOH functional group density when compared to COC 6013 (~50% norbornene content) and COC 8007 (~35% norbornene content) following UV/O_3 or O_2 plasma activation. Furthermore, COC 6017 showed a smaller average RMS roughness (0.65 nm) when compared to COC 8007 (0.95 nm) following activation making this substrate especially suited for nanofluidic applications, which require smooth surfaces to minimize effects arising from dielectrophoretic trapping or non-specific adsorption. Although all COC substrates showed >90% transparency at wavelengths >475 nm, COC 6017 showed significantly less transparency at wavelengths below 475 nm following activation, making optical detection in this region difficult. Our data showed distinct physiochemical differences in activated COC that was dependent upon the ethylene/norbornene content of the thermoplastic and thus, careful selection of the particular COC grade must be considered for micro- and nanofluidics. Finally, we determined that nanoscale columns introduce unique surface interactions differences of the dNMPs allowing for resolutions ranging from 0.42-0.94 and changes in the pH that can further enhance resolutions up to 2.7. Furthermore, it was determined that low buffer concentrations resulting in EDL overlap decrease the resolution. In addition, nanoscale electrophoresis was performed on the sub-second time scale, resulting in highly efficient separations. Ultimately, our research shows great promise for the use of nanoelectrophoresis within thermoplastic columns for the separation of dNMPs among many other molecules, not achievable on the microscale.

ACKNOWLEDGEMENTS

I would like to begin by thanking my advisor Dr. Steven Soper for his mentorship, guidance and support throughout my PhD. He has allowed me to explore various topics that interested me while still providing a clear path of success towards the completion of my degree.

I would also like to thank my lab mates here at UNC who truly understand the frustration, struggle and amazing reward this PhD has been for me (and us all!). Thank you to Dr. Maggie Witek, Dr. Swathi Pullagurla, Dr. Kumuditha Ratnayake, Dr. Matt Jackson, Dr. Varshni Singh and Dr. Franklin Uba. I greatly appreciate your time, intellectual support and friendship throughout this entire process. Go team Nano!

The support of my friends throughout this process has been one of the strongest sources of motivation for me. I cannot thank them enough for listening to me as I struggled to make sense of my place in this program as well as provide me with such love and humor to push me through the hard times. Katie, Monica, Alyssa, Leanne and Katherine, all friends from before my time at UNC, have continued to show their love and support through phones calls or weekend visits and have truly exemplified friendship. I cannot thank them enough. To Maria Lindell, my first friend I ever made here at UNC, although you may be miles away, you are still very close to me and such an amazing friend and support. To Kristina Herrera, Mike Schotzinger and James Taylor, all friends from my time here at UNC, thank you for your encouragement, support and most of all your understanding when science just did not make sense! I look forward to our continued friendship and the day I can see you all graduate!

To my father, there are not enough words I can say to thank you and show you just how much I love you. My entire life you have encouraged me to push through what seemed like insurmountable odds in all aspects of my life. This PhD has been no exception. You were the first person I would call

when I felt defeated, which was very often, and you knew that there was no greater gift you could give me besides your love and support. Every time I would say I wanted to quit you allowed me to explore the possibility and conclude for myself what you knew all along, that I was strong and capable enough to reach for my dream. You have always known, before I ever do, what I am capable of and I thank you for allowing me to explore. Because of your strength, I can be who I am today and there is no greater gift. Forever and Always. Look Dad, I did it, I went through the “black door”. I cannot wait to share with you what my next challenge will be.

To my fiancé, Dr. Will Black, the love I never thought I would find, thank you so much for knowing that there was nothing you could do for me but listen and simply be there. You knew the strength and intelligence I had inside of me and allowed space and support for me to find it myself. You are the best humor donor I could ever ask for and I smile knowing the adventures we will have in our lives. There is no better partner and teammate that I could dream of for this journey through life. Thank you!

TABLE OF CONTENTS

LIST OF TABLES

LIST OF FIGURES

LIST OF ABBREVIATIONS

AC	Alternating Current
ATR-FTIR	Attenuated Total Reflectance Fourier Transform Infrared Spectroscopy
B	Bandwidth (Hz)
C_{eq}	Equivalent circuit
C_i	Bulk Ionic Concertation of solution (mol/dm^3
Cyt C	Cytochrome C
DC	Direct Current
DL	Diffusive Layer
DLVO	Derjaguin, Landau, Verwey and Overbeek
DNA	Deoxyribonucleic acid
DRIE	Deep Reactive Ion etching
D_u	Dukhun number
E	Electric Field Strength (V/cm)
EDL	Electric Double Layer
EDTA	Ethylene Diamine Tetra Acetic Acid
EKP	Electrokinetic Phenomena
EOF	Electroosmotic Flow
eV	Electron Volt (1 eV= 1.6026 x 10 $^{-19}$ J)
F	Farady's Constant (96,485 C/mol)
F_d	Drag Force (N)
F_e	Electrical Force (N)
FIB	Focused ion Beam
FITC	Fluorescein Isothicyanate

G	Conductance (Ω^{-1})
g	Acceleration due to gravity (9.8 ms^{-2}
G_B	Conductivity of Buffer
I	Ionic strength of electrolytes
$I_{cond,bulk}$	Conduction current from bulk solution conductivity (A)
$I_{cond, surf}$	Conduction Current from Surface conductivity (A)
I_t	Tunneling current
k_B	Boltzmann's Constant (1.38 x 10^{-23} JK^{-1})
l_p	Persistence length
L_{cont}	Contour Length
m	Mass of electron (9.10938188 x 10^{-31} kg)
N_A	Avogadro's number (6.022 x 10^{23})
PDMS	Poly(dimethylsiloxane)
Q	Volume Flow Rate (L/min)
R	Molar Gas Constant ($JK^{-1}mol^{-1}$)
RMS	Root-mean Square
SL	Stern Layer
T	Kelvin Temperature
TBE	Tris(hydroxymehtyl)aminomethane-borate-EDTA
μ_i	Effective Ionic Mobility (m^2/sV)
μ_i^{∞}	Absolute Ionic Mobility
V	Applied Voltage (Volts)
v_{eof}	Electroosmotic velocity (cm/s)
v_{ep}	Electrophoretic velocity (cm/s)

z_i	Ionic Charge
ΔG	Change in Conductivity
Δp	Pressure drop (Atm)
ΔV	Voltage drop (Atm)
ε_0	Electrical permittivity of vacuum
ε_e	Electrical permittivity of a medium
ε_r	Relative dielectric constant
ε_w	Dielectric permittivity of solvent
ζ	Zeta Potential (mV)
η	Viscosity
κ	Electrical Conductivity
k_b	Bulk electrolyte conductivity ($\Omega^{-1}m^{-1}$)
k_d	Debye-Huckel parameter
k_s	Surface conductivity ($\Omega^{-1}m^{-1}$)
λ_d	Debye Length
μ_{eof}	Electroosmotic Flow (cm^2/Vs)
μ_{ep}	Electrophoretic Mobility (cm^2/Vs)
ρ	Resistivity at a temperature (T) (Ωcm)
σ	Density (gcm^{-3})
h	Planck's Constant
XPS	X Ray Photoelectron Spectroscopy
TOF-SIMS	Time of Flight Secondary Ion Mass Spectrometry
AFM	Atomic Force Microscopy
dNMPs	deoxynucleotide monophosphates

T_g	Glass transition Temperature
TEM	Transverse electro migration
NIL	Nanoimprint Lithography
-COOH	carboxy functional group
PSF	Point Spread Function
STED	Stimulated Emission Depletion
STORM	Stochastic Optical Reconstruction Microscopy
PALM	Photo-activated Localization Microscopy
Δ_{loc}	Localization Precision
SDS	Sodium dodecyl Sulfate
CTAB	Cetrimonium Bromide
NA	Numerical Aperture

CHAPTER 1. THERMOPLASTIC NANOFLUIDIC DEVICES FOR BIOMEDICAL APPLICATIONS

1.1 Introduction

Nanofluidic devices have become an ideal platform for investigating fundamental physical and chemical phenomena that are not readily accessible at the micro-scale. These include such phenomena as concentration polarization,[1-3] nonlinear electrokinetic flow and ion focusing,[4,5] mass transport in geometrically confined spaces,[6,7] nanocapillarity,[8] and electrical double layer (EDL) overlap effects.[1,9-11] Interestingly, these phenomena can be used to carry out unique processing capabilities to enable bioassays that cannot be realized using microfluidic devices. As such, rigorous research efforts have been implemented to realize the unique process capabilities associated with nanofluidics for many biomedical applications.

Early nano-based experiments utilized nanopores – structures whose depth is comparable to its diameter – as candidates for studying the transport properties of ions or molecules in confined spaces and the analysis of biomolecules.[12-19] However, more recently, nanofluidic devices with one or two dimensions in the nanometer scale, nanoslits or nanochannels, respectively, are being utilized for a number of applications due to their flexibility in terms of shape and size with surface properties that can be tuned based on the required function.[20,21]

Because of the unique properties that arise when the channel size is comparable to either the length scale of electrostatic interactions in solution or the size of the molecules being transported through them, nanochannel-based devices have garnered attention for applications such as single-molecule analysis,[17,22-24] molecular pre-concentration,[5] chemical analyses of mass-limited samples,[4,25] DNA electrophoresis,[26-28] desalination,[29] nanofluidic diodes,[30] real-time probing of biomolecules,[31-35]

ionic transport,[36] entropic trapping for DNA separations,[37] electrophoretic separations,[37,38] manipulation and detection of single molecules,[39] and control of molecular transport and wall interactions.[40,41]

For several years, inorganic-based substrates, such as silicon, glass and fused silica, were the most commonly used substrates for the fabrication of nanofluidic devices. Glass possesses well-established surface chemistry, hydrophilic surfaces allowing for favorable wetting when using aqueous solvents, good insulating properties, minimal surface defects, non-deformability at high pressures and well-established top-down fabrication techniques.[42,43] However, the challenge with the use of inorganic substrates for nanofluidic devices is the sophisticated, and high-cost fabrication technologies required to make the prerequisite devices; the fabrication technologies include ion beam milling, electron beam lithography to produce nanochannels in which the lateral dimension and depth are below 100 nm.

Recently, thermoplastics such as poly (methylmethacrylate), PMMA, polycarbonate, PC, cyclic olefin copolymer, COC, and polyethylene terephthalate, PET, have become viable substrates for fluidic applications, especially micro- and nanofluidics. The use of thermoplastics is attractive due to the diverse and simple fabrication techniques that can be employed to produce devices in a high production mode and at low-cost using such techniques as injection molding or hot embossing.[44-46] Even nanofluidic devices can take advantage of high production mode fabrication technologies to produce the relevant devices including nanoimprint lithography (NIL) or compression injection molding.[47-49] These replication-based technologies obviate the need for producing nanofluidic devices using direct writing with a focused ion beam instrument, for example.[50-53] In addition, thermoplastics' diverse physiochemical properties and the availability of a wide range of simple activation techniques can be employed to generate surface-confined functional groups[54-58] to produce surfaces to accommodate the intended application as well as increase wettability for fluidic applications. Common surface activation protocols for these devices include UV/O_3 and O_2 plasmas.[59-61] These activation techniques generate a host of

surface oxygen-containing species, such as carbonyls (aldehydes, ketones and carboxylic acids) and alcohols following a sequence of free-radical photo-initiated oxidation reactions.[60,62]

In spite of the various fabrication techniques available for producing nanochannels in thermoplastics, it is not until recently that thermoplastics are being adopted as substrates for nanofluidics. The slow evolution of these devices have been due to challenges associated with channel deformation and collapse encountered during device assembly – sealing a cover plate to the patterned fluidic substrate – and insufficient understanding of surface charge effects on the transport properties of charged molecules through thermoplastic nanochannels. In this review, we describe the fabrication of nanofluidic devices using thermoplastic substrates, assembly of nanofluidic devices, basic phenomena associated with the use of nanochannels for molecular assays, and several applications for the analysis of biomolecules using nanofluidic devices.

1.1.1 Scaling Effects on Transport

While microfluidics involves flows in channels with dimensions ranging from 150 nm to 100 µm, nanofluidics entails flow in slits with at least one dimension (channels = two dimensions) ranging from 1 to 150 nm.[63] A distinct feature of nanofluidics is that the relevant length scale is comparable to the range of surface and interfacial forces in liquids, such as electrostatic, van der Waals and steric interactions. As the dimensions of fluidic devices approach the nanoscale, changes in the dominating forces as well as the physics of the processes for fluid/particle transport diverge from what is typically seen in channels with dimensions >150 nm.[64,65]

Transport processes unique to the nanoscale arise from an increase in the surface-to-volume ratio of the channel.[64,65] Consequently, forces resulting from pressure, inertia, viscosity or gravity that usually play a dominant role in microscale flows become less dominant in nanofluidic devices while interfacial forces such as surface tension, become dominant. As shown in Figure 1–1, Conlisk *et al.*[65] provided a graphical representation of the pressure drop (Δp) and applied potential (V) as a function of

channel height for a nanoslit. The author revealed that as the channel height reduces from 80 nm to 10 nm and for a flow-rate of 1 μL/min, the pressure drop increases from 0.006 to 3 atm (~50000% increase), while the voltage required to maintain this volume flow rate increases by ~560% (0.05 V to 0.33 V). Therefore, it becomes difficult to transport fluids in nanoscale systems via pressure driven flow and easier to utilize electrokinetic (EK) flow.

Because the reduction in channel size increases the surface area to volume ratio, surface reactions are prevalent and surface roughness gradually begins to contribute to the overall flow dynamics.[4,7,66-70] Previous theories on EK flow in microchannels utilizing Boltzmann distributions and the Poisson-Boltzmann equation cannot be directly applied to nanochannels because the concentration of co- and counter ions in nanochannels are unequal and electrical double layer (EDL) overlap can occur.[69] This requires the development of new theories to explain EK flows in nanochannels. Furthermore, new theories are required to explain EK flow within thermoplastic nanochannels due to the non-uniformity of surface charge generated through the previously mentioned activation protocols.[71]

At the nanoscale, the EDL leads to non-uniformity in the motion of the bulk/neutral solvent as well as large non-uniform transverse electric fields resulting in Poiseuille-like flow.[4,66,68,70] This non-uniformity has dramatic effects on separations within nanochannels due to the fact that analytes spend a significant time migrating through the EDL.[68] Counter-ions are more attracted to the wall and their flow is impeded, while co-ions are repelled from the wall and are thus, transported faster.[4,66] In addition, differences in flow based on size can be observed in nanofluidic channels because smaller molecules approach the wall to a greater degree and experience slower velocities compared to larger molecules.[4] Also, at the nanometer

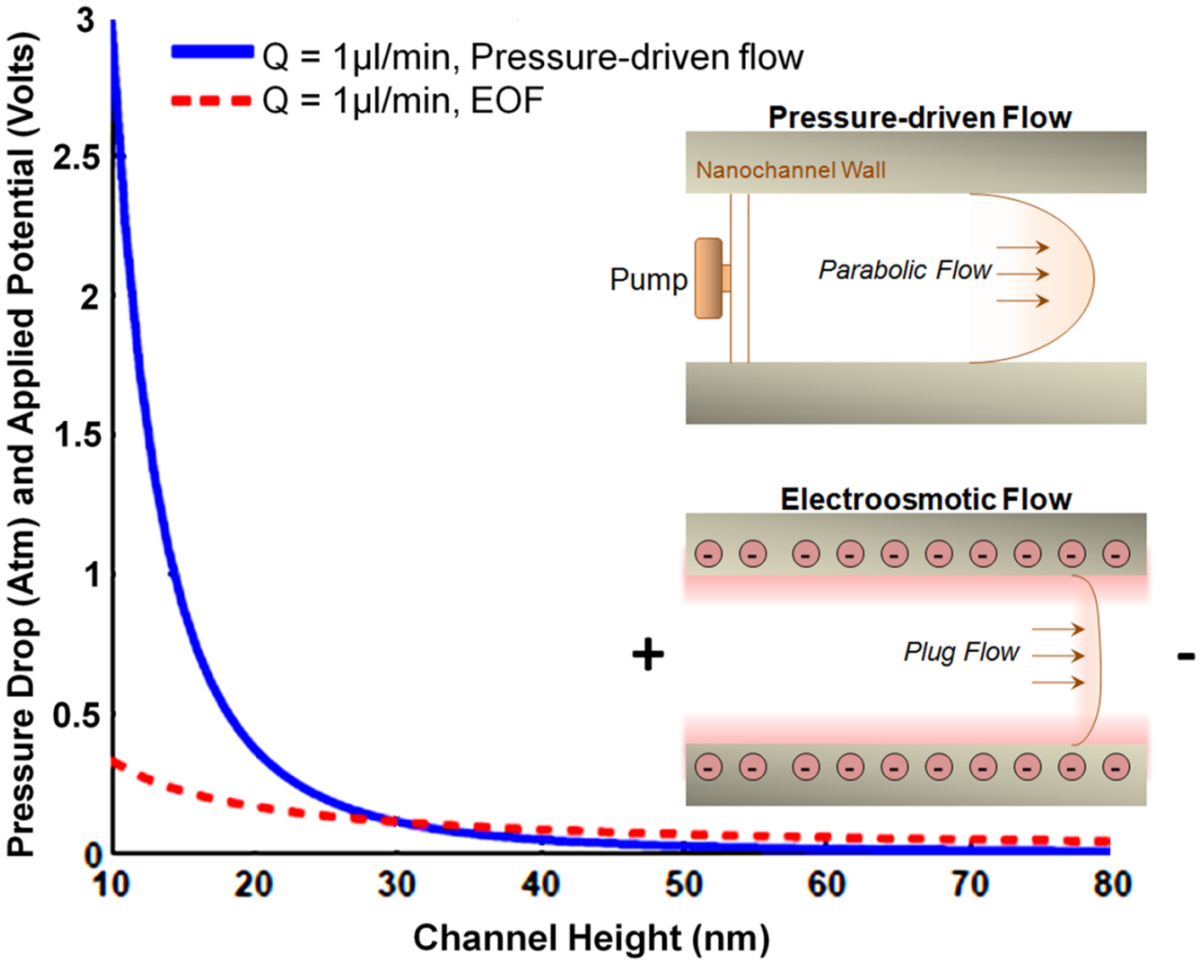

Figure 1–1 Required pressure drop and voltage drop for nanochannels with different channel heights. Nanochannel length and width are 3.5 µm and 2.3 µm, respectively; zeta potential is -11 mV for 1 M NaCl solution. Reproduced with permission from Conlisk et al. Copyright 2005 Wiley-VCH. Inset shows the comparison between the parabolic and plug flow profiles from the pressure-driven and electroosmotic flow, respectively.

scale, the kinetics of adsorption/desorption approach the time required for diffusion forcing considerations of wall adsorption.[68]

Furthermore, concentration polarization is observed at the interface between microchannels and nanochannels due to the increased flux of ions in the nanochannel resulting from the enhanced transport of selected ions within the EDL.[4,66,68] When the EDL spans the dimensions of the nanochannel, counterions are able to pass through the channel while co-ions are excluded resulting in the accumulation of co-ions at the inlet of the nanochannel with an increased transport of counterions.

Lower velocities may also be observed within nanochannels when compared to microchannels due to EDL overlap[66] and electro-viscosity effects.[66,72-74] The decrease in channel dimensions can cause the ratio of the apparent to true viscosities to become as high as 1.3 depending on the material of the channel wall, spatial size and shape of the channel, ionic concentration, zeta potential, temperature, dielectric constant and other properties associated with the liquid. This increase in viscosity can result in an apparent decrease in the electroosmotic flow (EOF) within nanochannels.[73]

1.1.2 Fabrication of Nanofluidic Devices

Several review articles have discussed different techniques for the fabrication of nanofluidic devices.[75-80] As such, in this review article we will only briefly introduce some common fabrication modalities used for creating nanofluidic slits or channels. For the most part, the fabrication technique adopted depends on the substrate of choice, which may be inorganic (fused silica, glass, silicon nitride or silicon) or organic (elastomers or thermoplastics), and the desired dimension of the nanostructures.

1.1.2.1 Fabricating Nanofluidic Devices in Inorganic Substrates

Inorganic substrates have been widely used as substrates for the fabrication of nanofluidic devices due to their established surface chemistry, excellent optical properties and well-entrenched fabrication techniques.[77] Prominent techniques for the fabrication of nanochannels in inorganic substrates utilize a top-down approach with direct writing via Electron Beam Lithography (EBL) followed

by dry etching or Focused Ion Beam (FIB) milling. Over the years, several research groups have utilized EBL and/or FIB to develop nanofluidic devices in inorganic substrates for the analysis of biomolecules or evaluating transport properties in nanofluidic channels.[24,28,81-83]

Other techniques for making nanofluidic devices in inorganic substrates include the use of nanowires as sacrificial templates,[84] conventional machining by etching of a sacrificial strip separating a substrate and the capping layer[42] and self-enclosing of nanochannels using a UV laser pulse.[51] A relatively new technique for the direct writing of sub-10 nm structures into Si or other inorganic substrates is He ion beam writing.[85,86] In this case, low atomic mass He ions are used instead of gallium with the concomitant less scattering of He ions with respect to Ga ions resulting in the ability to form nanostructures with much smaller dimensions.

The challenge with using inorganic substrates is the fact that EBL or FIB must be used, in many cases, to make each device making the use of these nanofluidic devices prohibitive for most applications based on accessibility of the patterning equipment and the cost of producing the device. While a commercial entity does market glass-based nanofluidic devices using deep UV lithography, the structure size is limited to around 100 nm and the cost is still somewhat high (www.bionanogenomics.com). Thus, alternative fabrication strategies must be considered to realize better accessibility of nanofluidic devices into the general research and commercial sectors, especially in the diagnostic regime where disposable devices are required due to the issues arising from cross-contamination giving rise to false negative results.

1.1.2.2 Fabricating Thermoplastic Nanofluidic devices

Thermoplastics are high molecular weight, linear or branched polymers with a higher Young's modulus and a wider range of physicochemical properties compared to the elastomer, PDMS. The deformability of thermoplastics makes them useful substrates for the fabrication of microfluidic channels via hot embossing, injection molding, compression molding, thermal forming or casting

techniques. Typical thermoplastics, including PMMA, PC, COC and PET, possess glass transition temperatures (T_g) that are significantly lower than that of glass allowing for the fabrication of nanostructures at high production rates, low cost and high fidelity using techniques such as NIL. Furthermore, copolymers can be used as a substrate for nanofluidic devices that have a range of T_g arising from differences in the ratio of monomeric components used allowing precise selection of both the substrate and cover plates' T_g to ensure that deformation of the nanostructures does not occur.[87]

Since its first report in the 1990s,[88-90] NIL has been used for the production of nanochannels in thermoplastics and has demonstrated the ability to fabricate sub-10 nm structures. The main advantage of NIL is the ability to build multi-scale patterns in a single imprinting step. Further details on NIL are presented in a recent review by Chantiwas *et al.*[77] Additional techniques for the fabrication of nanochannels in thermoplastics includes direct proton beam writing,[91] thermomechanical deformation,[92] compression of microchannels,[93] sidewall lithography and hot embossing,[94] UV-lithography/O_2 plasma etching,[95] hot embossing with PMMA molds,[96] refill of polymer microchannels,[97] and the use of silica nanowire templates.[98]

For NIL-based fabrication of nanofluidic devices, the process begins by patterning access microchannels in a Si substrate using conventional optical lithography (see Figure 1–2A).[99] This is followed

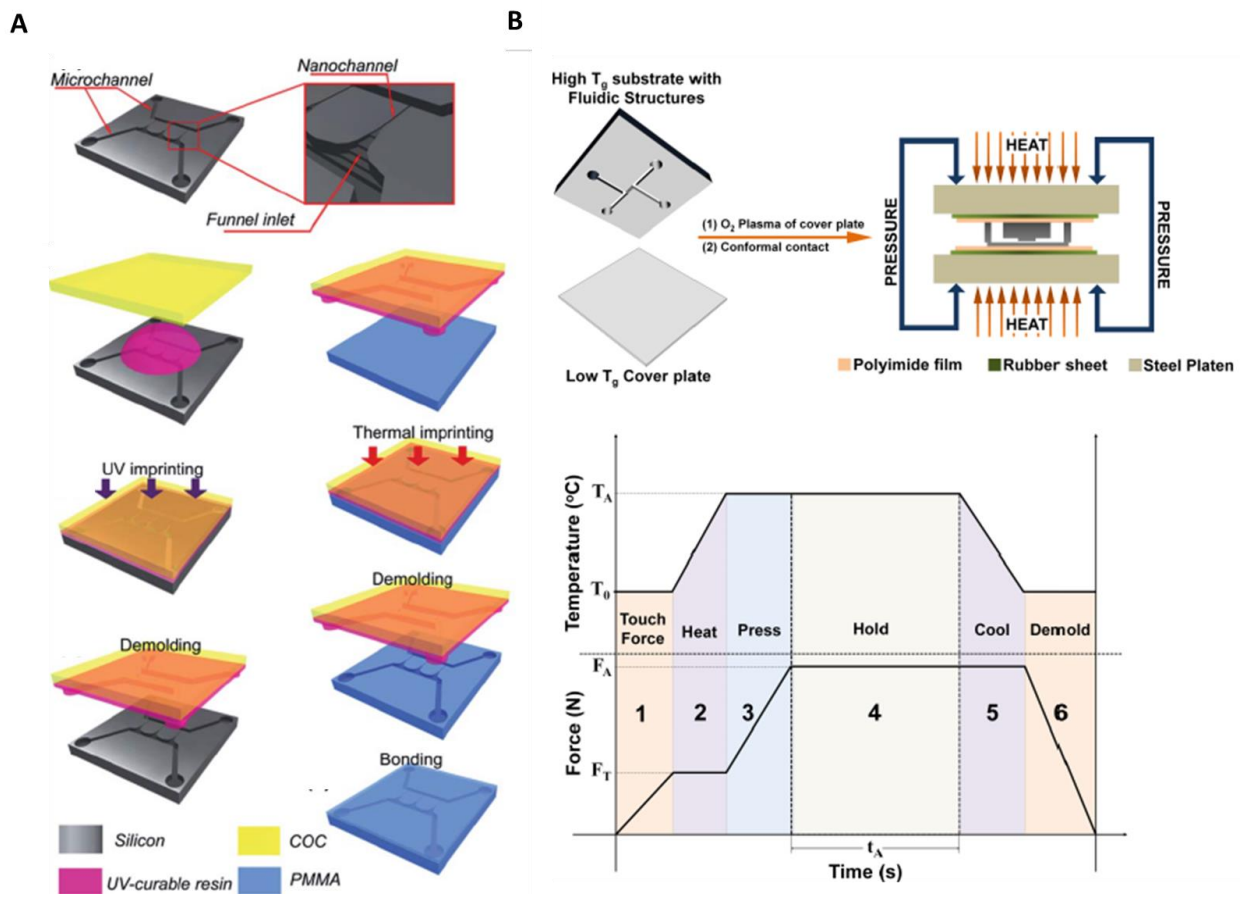

Figure 1–2 (A) A schematic of the design and fabrication processes for the polymer-based nanofluidic device. (a) Silicon master, which consisted of micron-scale transport channels and a funnel-like inlet for the nanochannels; (b)-(d) fabrication steps to produce a protrusive polymer stamp in a UV-curable resin by imprinting from the silicon master; (e)-(g) fabrication steps to generate nanofluidic structures in PMMA by imprinting from the UV-curable resin stamp; (h) bonding step with a PMMA cover slip to build the enclosed mixed-scale polymer device with microchannels and nanochannels. (B) (a) Schematic of the protocol used for assembly of the hybrid-based fluidic devices and the thermal press instrument. (b) Temperature-pressure process profile showing the six stages for the thermal fusion bonding cycle. See main text for a description of the 6 stages of bonding.

by FIB writing of nanochannels in the same Si substrate containing the microchannels; this Si wafer is used as a mold master and has the same polarity as the desired finished thermoplastic device. Once the Si mold master is produced, UV-NIL is undertaken to produce resin stamps with the reverse polarity as the thermoplastic device. These resin stamps are then used in a thermal-NIL step to generate the finished thermoplastic device. The advantage of this production process is that a number of nanofluidic

devices (>100) can be produced from the same Si mold master without requiring to return to the optical lithography and FIB patterning tools, significantly reducing the cost of generating nanofluidic devices.

The aforementioned techniques for producing nanostructures in thermoplastics employ a top-down approach and as such, an assembly step is required to enclose the fluidic network. This consists of bonding a cover plate to the substrate possessing the fluidic network, which typically involves heating the cover plate and substrate to a temperature near the T_g of the material. This assembly step can involve thermal- or solvent-assisted fusion bonding.[100] Typically, thermal fusion bonding is achieved by either heating the substrate and cover plate to a temperature slightly above their T_g under a constant pressure and time or bonding at a temperature lower than the T_g of the material by UV/O_3 or O_2 plasma treatment of the surfaces prior to assembly.[47,53,99,101,102] The former approach has been known to result in significant nanochannel deformation while the latter results in devices with weak bond strength. Similarly, solvent-assisted bonding frequently result in dimensional instability due to material embrittlement or dissolution.[100] Unfortunately, these assembly issues can generate low process yield rates, typically <40% (process yield rate = percentage of devices that possess dimensions comparable to design parameters).

In a recent report (see Figure 1–2B), functional thermoplastic nanofluidic devices were developed at process yield rates >90% using a robust assembly scheme in which a high T_g thermoplastic substrate was thermally fusion bonded to a cover plate with a T_g lower than that of the substrate.[87] Device assembly was achieved by bonding a O_2 plasma treated cover plate to an untreated substrate at a temperature ~5^{o}C lower than the T_g of the cover plate using a total processing time of 16 min. COC (T_g = 75^{o}C) was used as the cover plate for a PMMA substrate due to its excellent optical transmissivity, low autofluorescence,[103,104] low moisture uptake (< 0.01%), high temperature tolerance, and chemical resistance. Examples of nanofluidic devices made from thermoplastics and assembled using this method are shown in Figure 1–3.

1.2 Relevant Electrokinetic Parameters

Electrokinetic transport of molecules in thermoplastic nanochannels is influenced by several physical parameters that include the EDL, zeta potential, surface charge density, uniformity and electroosmotic flow. In the sections that follow, these parameters will be discussed in the context of electrokinetic transport in nanochannels. A summary of electrokinetic parameters for PMMA nanochannels can be found in Table 1-1.

1.2.1 Electric Double Layer (EDL)

Many solid surfaces in contact with aqueous electrolyte solutions gain surface charge density arising from differences in electron (or ion) affinities between the surface and the solution, ionization of surface groups or reaction equilibria such as protonation or deprotonation. For instance, a glass surface immersed in an electrolyte at pH ≥3[105] will acquire negative charges with a layer of electrolyte cations that strongly associates to the solid surface. Outside this layer, another layer of mobile cations is generated. These two layers form a single shielding layer that is referred to as the EDL or Debye Layer.

For a channel filled with a symmetrical 1:1 electrolyte, such as KCl, with ionic concentration *c*, the EDL thickness or λ_D can be represented as;

$$\lambda_D = \left(\frac{\epsilon_0 \epsilon_r R T}{2 F^2 c}\right)^{1/2} \quad (1.1)$$

Device	Terminating groups	σ_s (mC/m^2)	ζ (mV)	μ_{eof} (cm^2/Vs) × 10^{-4}	
				Expected*	Measured
Nanoslit	O_2-PMMA	- 38.3	- 57.1	4.53	0.93 ± 0.025
	NH_2-PMMA	28.4	45.8	- 3.63	- 0.82 ± 0.012
Nanochannel	O_2-PMMA	- 40.5	- 59.8	4.74	1.02 ± 0.017
	NH_2-PMMA	22.9	38.3	- 3.04	- 0.75 ± 0.021

Table 1-1 Measured and expected EOF values as well as surface charge and zeta potentials for the plasma activated and amine terminated devices investigated at pH 7.8.[74]

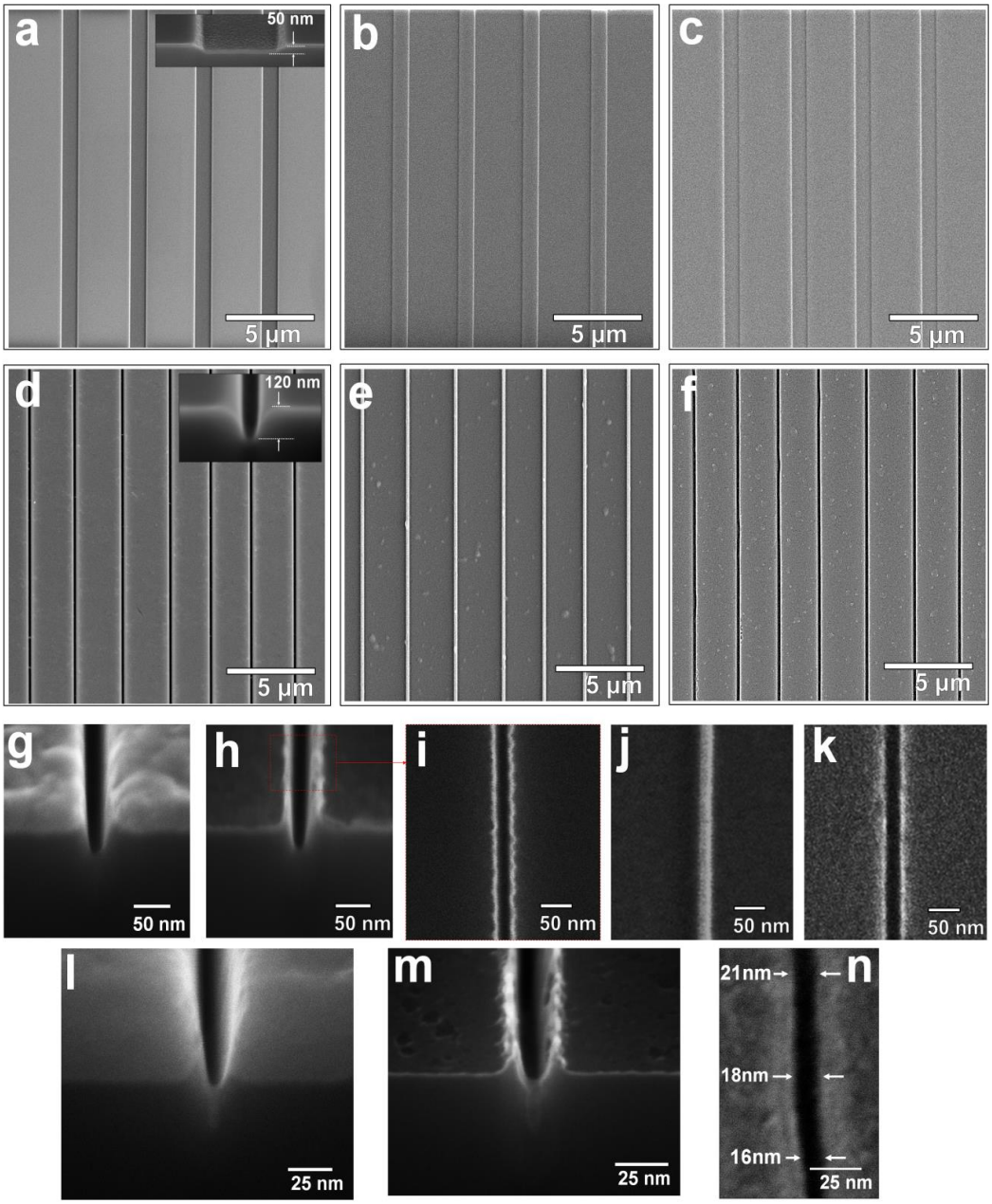

Figure 1–3 SEMs of Si masters (a, d, g, h, i, l, m), resin stamps (b, e, j) and the fluidic devices imprinted in PMMA (c, f, k, n). The device in a – c is a nanoslit device with a width of 1 µm and depth of 50 nm. In d – f, a device with a 120 nm × 120 nm channel is shown. In g – k, a nanofluidic device with 40 × 40 nm channel is shown with a 40 nm thick Al layer deposited on the Si master prior to milling. Finally, in l – n, a nanofluidic device with ~20 × 20 nm channel is shown with a 80 nm thick Al deposited on the Si master prior to milling. In all cases, the substrate used in all cases was PMMA (Tg = 105oC). Figures a – f, m – n were reproduced with permission from Uba et al.74, Copyright Royal Society of Chemistry. Figures g – k and l are unpublished

where R is the gas constant ($J \cdot mol^{-1}K^{-1}$), ϵ_0 is the permittivity of vacuum ($F \cdot m^{-1}$), ϵ_r is the dielectric constant of the medium, F is the Faraday constant ($C \cdot m^{-1}$), and T is the temperature (K). λ_D can range between 1 and100 nm for electrolyte concentrations between 10 and 0.01 mM.[63]

The ratio of κa, where κ is $1/\lambda_D$ and a is the channel radius, has been used to describe the state of electroneutrality of the bulk solution within the channel/slit.[4,67] When $\kappa a \gg 1$, the solution towards the center of the channel is electrically neutral (*i.e.,* equal concentration of co-ions and counter-ions) with a neutral electric potential and displays the classically observed plug-like flow. However, in the case of $\kappa a \approx 1$, there is overlap of the EDL leading to an excess of counter-ions in the channel and loss of electroneutrality. In this case, the flow profile adopts a parabolic shape and is regarded as Poiseuille like flow.

1.2.2 Zeta Potential

The zeta potential, ζ, which measures the electric charge developed on a solid surface in contact with an aqueous solution, is the electric potential at the boundary dividing the Stern and diffuse layer, also known as the shear plane. Typically, the values of ζ vary between -200 *m*V to +200 *m*V depending on the chemistry of the solid/liquid interface. Also, it is a property that depends on the ion concentration, ion valency, ion size, pH and temperature of the solution.[106] As a result, each solid-liquid interface will have its own unique and measureable ζ.

ζ has been an important parameter in a number of applications,[107,108] such as the characterization of membrane efficiency,[109] biopolymers[110,111] and electrokinetic transport of particles and biological cells.[112] Typically, it has been evaluated indirectly from other electrokinetic parameters.[113,114,115] ζ can be mathematically represented as;[60,74]

$$\zeta = \frac{2\,k\,\mathrm{T}}{e}\,ln\left[\frac{2\,e\,\sigma_s\,\lambda_D}{\epsilon_r\,\epsilon_0\,k_B\,\mathrm{T}} + \sqrt{1+\left[\frac{\left(e\,\lambda_D/\epsilon_r\,\epsilon_0\,k\,\mathrm{T}\right)^2}{4}\right]}\right] \qquad (1.2)$$

where σ_s is the surface charge density and *k* is the Boltzmann's constant. Sze *et al.*[116] reported that ζ for surfaces in KCl solutions varied between -88 to -66 mV and -110 to -68 mV for glass and PDMS surfaces, respectively. As a comparison, ζ for PMMA-based plasma modified nanochannel devices was reported to be -59.8 mV, as seen in Table 1-1[74]

1.2.3 Surface Charge Density

Electrical conductance measurements across nanochannels filled with ionic salt solutions have been used to evaluate the surface charge density, σ_s. When an external electric field is applied across a nanochannel filled with an ionic salt solution, the measured electrical conductance (G_T) has been represented as;

$$G_T = 10^3\left(\mu_{K^+} + \mu_{Cl^-}\right) c\, N_A\, e \cdot \frac{n\, w\, h}{L} + 2\,\mu_{opp}\sigma_s\, n\,\frac{(w+h)}{L} \qquad (1.3)$$

where *w, L* and *h* are the nanochannel width, length and height, respectively, N_A is Avogadro's number, *c* is the electrolyte concentration in mol/L, *n* is the number of nanochannels in the device and μ_{K+} and μ_{Cl^-} are the ion mobilities of K^+ and Cl^- ions, respectively ($\mu_{K+} = 7.619 \times 10^{-8}$ m^2/V s and $\mu_{Cl^-} = 7.912 \times 10^{-8}$ m^2/V s). At high salt concentrations, G_T is dominated by ions in the bulk solution and the measured electrical conductance depends primarily on the nanochannel dimensions and electrolyte concentration.[117,7,118] However, at low salt concentrations, the nanochannels become predominantly filled with counterions and σ_s governs the total ion conductance in the nanochannel.

As reported by Uba *et al*,[74] the measured $|\sigma_s|$ of O_2-modified PMMA nanoslits (1 μm × 50 nm; width × depth) was ~38.2 *m*C/m^2. This value was less than 60 *m*C/m^2 reported by Stein *et al.*[119] and 214 *m*C/m^2 reported by Schoch *et al.*[117] for glass-based nanoslits measured at pH 8. However, surface charge measurements performed in a nanoslit hybrid device – PMMA substrate bonded to oxygen plasma treated COC cover plate – showed a $|\sigma_s|$ of 57.3 mC/m^2.[87] The difference in surface charge density was attributed to more carboxyl groups generated on COC compared to PMMA when treated under similar oxygen plasma conditions.[120,121] UV/O_3 activation of the device post-assembly was reported to result in a

4.5% higher surface charge due to the increase in the density of surface carboxylates upon UV/O_3 activation of the PMMA substrate. The measured $|\sigma_s|$ in PMMA NH_2-modified nanoslits was 28.4 *m*C/m^2. In the case of the 120 nm × 120 nm nanochannels, the surface charge densities were 40.5 *m*C/m^2 and 22.9 *m*C/m^2 for the O_2- and NH_2-PMMA devices, respectively.

1.2.4 Electroosmotic Flow (EOF)

When an external electric field is applied across a channel containing counter- and co-ions, there is bulk movement of ions. The positive ions (counter) in solution are attracted towards the cathode while the negative ions (co-ions) are attracted towards the anode when the surface is negatively charged. The movement of the excess counter ions will result in a viscous drag of the surrounding liquid molecules inducing a bulk flow of ions under the influence of the external electric field. This is referred to as the EOF. For a thin EDL and/or large channel height, the EOF has a 'Plug-like' (or flat) profile. Unlike hydrodynamic flow, which has a 'parabolic' profile, this flat flow profile has been reported to result in high-efficiency electrokinetic separations due to the significant reduction in Taylor dispersion (see inserts in Figure 1–1).[122,123,124]

The direction of the EOF depends on the type of charge (positive or negative) on the channel wall. For a negatively charged wall under the influence of an external electric field (E; V/cm), the bulk liquid flows toward the cathode while it is reversed in a positively charged wall. The EOF can be described in terms of a mobility, $\boldsymbol{\mu}_{eof} = \boldsymbol{\upsilon}_{eof}/E$, where $\boldsymbol{\upsilon}_{eof}$ is the steady-state bulk velocity. Assuming the Debye length is significantly smaller than the width of a fluidic channel and the surface charge density is uniform along both the axial and radial dimensions, $\boldsymbol{\mu}_{eof}$ can be represented in terms of the bulk solvent viscosity η_o, and ζ by the Helmholtz-Smoluchowski relation:[125]

$$\boldsymbol{\mu}_{eof} = \frac{\epsilon_0 \epsilon_r \zeta}{\eta_o} \qquad (1.4)$$

Several articles have reported the $\boldsymbol{\mu}_{eof}$ of nanochannels measured using the current monitoring method.[126] Uba *et al*[74] recently showed that the EOF of O_2- and NH_2-modified PMMA nanochannels were

1.02 ±0.02 × 10^{-4} cm^2/Vs and -0.75 ±0.02 × 10^{-4} cm^2/Vs, respectively, as seen in Table 1-1. The values reported for the O_2-PMMA nanochannels were shown to be similar to that reported by Menard *et al*.[28] for fused silica nanochannels (≤100 nm in width and depth) measured using 2× TBE with 2% polyvinylpyrrolidone acting as an EOF suppressor (0.79 ±0.01 × 10^{-4} cm^2/Vs) and ~35.8 ±4.4% lower when compared to fused silica channels measured with 2× TBE only (1.58 ±0.01 × 10^{-4} cm^2/Vs).

1.3 Nanochannels for the Analysis of Biopolymers

Nanofluidic channels have been used for the analysis of biopolymers with DNA being the most reported. Most applications for DNA analysis begins with DNA linearization by confinement induced by the nanofluidic device. DNA linearization has been achieved using a variety of nano-systems that include nanoslits,[101] nanochannels,[127] staggered densely packed circular or diamond shaped nanopillars[83,128,129] and reconfigurable-tunable elastomeric nanochannels.[130,131] Unlike other linearization techniques, which exert a high stretching force at an anchored end that decreases along the length of the molecule, nanoconfinement allows the entire confined DNA molecule to be exposed to the same confinement force.[78]

1.3.1 DNA as a Model Biopolymer

The physical properties involved in the molecular dynamics of DNA molecules can be described by three parameters; the contour length, L_c, persistence length, l_p, and the effective width, w_{eff}.[132] The contour length refers to the total length of the DNA when it is fully stretched while the persistence length describes the local rigidity of DNA imposed by its double helical structure. On length scales smaller than l_P, a DNA molecule is considered rigid, while it is flexible at length scales larger than l_P. The intrinsic persistence length and width, w_0, of dsDNA in 0.1 M aqueous NaCl are ~50 nm (150 bp) and 2 nm, respectively.[133]

In solution, a highly negative-charged polymer like DNA will occupy a finite volume of space, with an excluded volume around itself preventing other molecules to enter this excluded volume due to

steric hindrance, repulsive effects and interactions with the solvent. This self-avoidance was introduced by Flory[134, 135] and later generalized to the semi-flexible case by Schaefer *et al*.[136] According to Flory-Pincus, a biopolymer in solution is characterized by the radius of gyration,

$$R_G \cong \frac{R_F}{\sqrt{6}} \qquad (1.5)$$

where R_F, which is the end-to-end length, is represented as $(l_p \times w_{eff})^{1/5} L_c^{3/5}$. Based on the values reported by Reisner *et al.*,[137] for 20 mM TBE buffer, w_o is 3 nm and w_{eff}, or the width including the hydration layer, was estimated to be 12 nm. Based on equation 1.5, the radii of gyration would be ~560 nm and 1,140 nm for λ (48.5 kbp) and T4 (160 kbp) DNA, respectively.

1.3.2 DNA Confinement in Nanochannels

Previous reports have shown that a DNA molecule confined in a nanochannel will stretch along the channel axis to a substantial fraction of its full contour length.[137] Confinement elongation of genomic-length DNA has several advantages over alternative techniques for extending DNA, such as flow stretching or stretching based on tethering. Confinement elongation does not require the presence of a known external force because a molecule in a nanochannel will remain stretched in its equilibrium configuration allowing for continuous measurements of length.[81]

In confined spaces, where R_G is much larger than the geometrical average depth, D_{av}, of the nanochannel, the number of available configurations of the polymer is reduced. Two main confinement regimes exist that depend on differences between the D_{av} and l_p. When $D_{av} >> l_p$, the molecule is free to coil within the nanochannel and stretching is entirely due to excluded volume interactions between different coiled segments of the polymer separated along the backbone. Coiling of the molecule can be envisioned to be broken up into a series of blobs with diameter L_b, while the stretching is a result of repulsion between the blobs; this is known as the deGennes regime.[138] Within the blobs, the confinement force is only a weak perturbation while each blob retains the property of the bulk polymer. The extension length of the molecule, R_x, can be calculated using;

$$R_x = L_c \left(\frac{w_{eff}\, l_p}{D_{av}^2}\right)^{1/3} \quad (1.6)$$

where $D_{av} = \sqrt{D \times h}$ and is the geometrical average of the two confining dimensions in the nanochannel.

As the channel width decreases and $D_{av} << l_p$, the stretching is no longer a result of volume exclusion but an interplay between confinement and the intrinsic elasticity of the DNA molecule. The strong confinement prevents the molecule from forming loops within the nanochannel. Back folding becomes energetically unfavorable and stretching becomes a result of deflection of the molecules with the channel walls. The average length between these deflections is of the order of the Odijk length scale; $\lambda_p \cong (D_{av}^2\, l_p)^{1/3}$. This regime is referred to as the Odijk regime.[139, 140] For a small average deflection, θ, R_x is represented as;

$$R_x = L_{cont} \cos\theta \cong L_{cont} \left[1 - 0.361 \left(\frac{D_{av}}{l_p}\right)^{2/3}\right] \quad (1.7)$$

Recent reports have revealed the existence of an intermediate region between the deGennes and Odijk regimes – extended deGennes regime – where the excluded volume interaction is weaker than the thermal energy.[141,142]

1.3.3 Effect of Ionic Environment on DNA Stretching

According to Reisner *et al.*,[137] variations in the ionic strength affect the configuration of a DNA molecule by modulating the range of electrostatic interactions between the charges on the phosphate backbone. As previously discussed, electrostatic interactions in electrolyte solutions are screened over a characteristic scale known as the Debye length. The geometry of the polymer results in two types of electrostatic interactions:[81] (i) Interactions between charges separated in contours that create repulsion between back looping segments resulting in an effective DNA width (w_{eff}) that is larger than the intrinsic width w_0; and (ii) local repulsive interactions between charges separated by less than the Debye length in contour resulting in an increase in the persistence length to a new value for l_p. The mechanisms of these interactions determine the ionic strength variation of the extension over an ionic strength range.

The Odijk-Skolnick-Fixman[143] equation, based on single-molecule elasticity, has suggested that the persistence length of a DNA when in solution relates to the ionic strength by;

$$l_p = l_{p_o} + \frac{0.0324\ \text{M}}{I}\ \text{nm} \qquad (1.8)$$

where l_{p_o} and I are the high salt value of the persistence length (~50 nm) and electrolyte ionic strength, respectively. According to equation 1.8, l_p is roughly equal to l_{p_o} until the ionic strength drops below 10 mM. l_p increases up to ~80 nm between 10 mM and 1 mM.

Although theory indicates that changing the ionic strength can result in DNA stretching, experimental results have shown that nanoconfinement is required for these effects to be observed. Krishnan *et al.*[144] showed nanoslits can be used to extend DNA by variations in the ionic strength of the buffer.

1.4 Applications of Thermoplastic Nanochannels

1.4.1 DNA Analysis in Polymer Nanofluidic Devices

Over the past decade, researchers have become interested in using polymer nanochannel devices for DNA analyses due to their biocompatibility,[63] surface modification ability,[74] ease of fabrication and low cost devices with high production rates.[74,87] While there are many studies and reviews dealing with DNA analyses using glass-based nanochannel devices, in this manuscript we will focus on reviewing DNA analyses using thermoplastic nanochannel devices.

In 2004, Guo and coworkers studied the stretching of DNA in size-controllable PDMS-PMMA devices at 3 different nanochannel dimensions. T5 phage DNA was stretched in densely packed nanochannel arrays with dimensions of 300 nm × 700 nm, 300 nm × 500 nm and 75 nm × 120 nm. They observed stretching of 15%, 30% and 95%, respectively, in these devices showing channel size dependence on stretching as predicted from the de Gennes and Odijk.[145]

In 2007, Takayama and coworkers demonstrated a tunable nanochannel device capable of stretching DNA.[146] They were able to enhance DNA elongation by applying a force on the triangular

shaped PDMS device to reduce the size of the elastomeric nanochannels. Huh *et al.*[130] from the same group demonstrated this concept by investigating the stretching of λ-DNA inside elastomeric nanochannels and controlling their dimensions in the presence of a force. DNA stretching was achieved in oxidized PDMS nanochannel arrays made with UV curable epoxy. Reported nanochannels (in the absence of a force) consisted of isosceles triangle shaped channels with an average base length of 688 nm and an average height of 78 nm. When λ-DNA was electrophoretically driven into these uncompressed nanochannels, they observed stretching of up to 30% of the DNA's full contour length (~5.6 μm). While applying a pressure of 22 kPa, DNA stretching was increased up to ~13.6 μm, which is ~73% from its full contour length. Once the force was removed, the DNA returned to its original stretching in <1 min (see Figure 1–4).

Valbusa and coworkers investigated the DNA extension using PDMS nanofluidic devices with both optical and electrical detection modalities.[147-151] Angeli *et al.*[147] fabricated nanochannel devices in hard PDMS (h-PDMS) to investigate several separation mechanisms, such as entropic trapping, entropic recoiling and stretching of λ-DNA using 130 nm deep and 650 nm wide nanochannels as well as 60 nm and 600 nm deep entropic traps by fluorescence detection. These devices were adopted to explore the stretching of λ-DNA using fluorescence. They did not observe significant variation in the elongation of single DNA molecules within a nanochannel that were 280 nm deep and 1 μm wide. Furthermore, their investigation revealed that when a DNA molecule translocated through a thin nanochannel region, it stretched due to confinement effects and once it reached a deeper region of the channel, it changed its confirmation to a relaxed configuration (see Figure 1–5A and B). They were able to achieve similar entropic trapping and stretching results using polymer-based devices compared to the results concluded by Han and Craighead on glass-based nanochannel devices.[152,153]

Fanzio *et* al.[148] used electrical detection to reveal that DNA inside nanochannels would transition to the Odijk regime from the deGennes regime by applying a stress on top of the device to make the

nanochannels compress. They used a double replica molding process to produce the final device. It consisted of 3 layers of polymeric material as shown in Figure 1–5C, a thick PDMS 10:1 slab, a thin PDMS 3:1 layer and an oxidized layer (~100 nm) covered with a glass coverslip. The cross-sectional profile as shown in the figure was triangular with a depth of 70 ±5 nm and with of 1 ±0.3 µm. The devices consisted of two microchannels with cylindrical pillars (h = 50 µm, d = 50 µm) separated by a distance of 15 µm. The nanochannel (h = 790 nm, w = 290 nm) was milled to connect the two microchannels. They controlled the size of the nanochannel by applying a force from the top of the device with a calibrated moving screw.

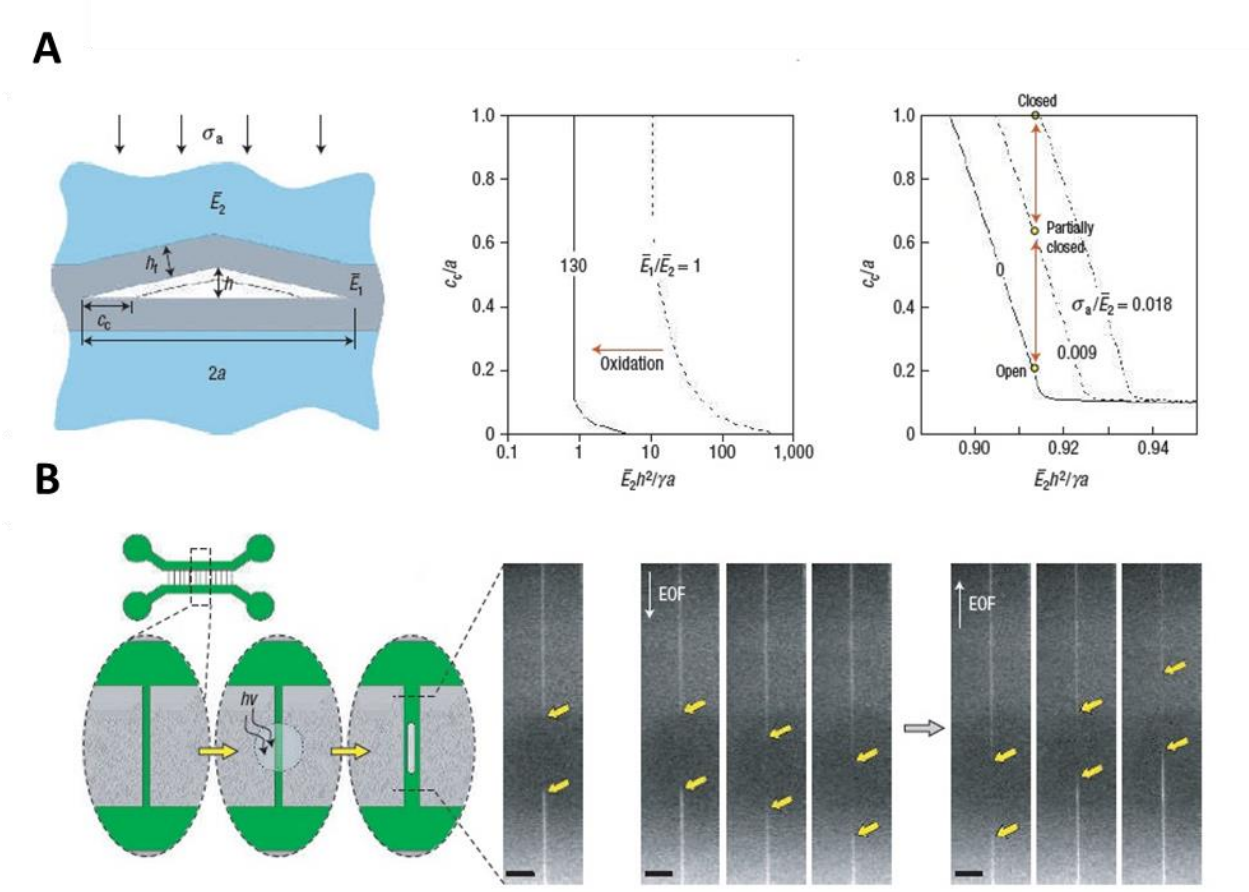

Figure 1–4. (A) Fabrication of structurally stable elastomeric nanochannels. c, the cross-section of relaxed nanochannels can be approximated as an isosceles triangle with an average base length of 688 nm (2a) and an average height of 78 nm (h). d, Normalized closure distance (cc/a) plotted against E.2h2/γ a for both the non-oxidized (E.1/ E.2 =1) and oxidized (E.1/ E.2 =130) states when there is no applied compressive stress (σa/ E.2 =0). e, the solid and dashed lines indicate the closure distance for

relaxed and compressed nanochannels, respectively. Note that E.1/ E.2 =130. Reversible closure of the nanochannels is demonstrated by the reversible vertical jumps to and from the dashed lines (shown with red arrows) when remote stresses are applied or removed, respectively (σa/ E.2 =0.018 and 0.009, corresponding to σa =22 and 42 kPa, respectively). (B) DNA manipulation and in situ fabrication of movable nanostructures. d, the nanochannels are constricted by the compressive stress of 22 kPa. e, a target area is selectively polymerized by ultraviolet. Subsequently, strong illumination photobleaches the polymerized region. f, Restoration of the channel size releases the polyacrylamide nanofilament. In fluorescence imaging, the filament appeared as a dark segment. Yellow arrows represent the extremities of the filament. g, the nanofilament can be manipulated to move along the nanochannel by electro-osmotic flow (EOF). h, the motion is reversed when the direction of electro-osmotic flow changes. Scale bars: 10 μm. Copyrights Nature Publishing Group

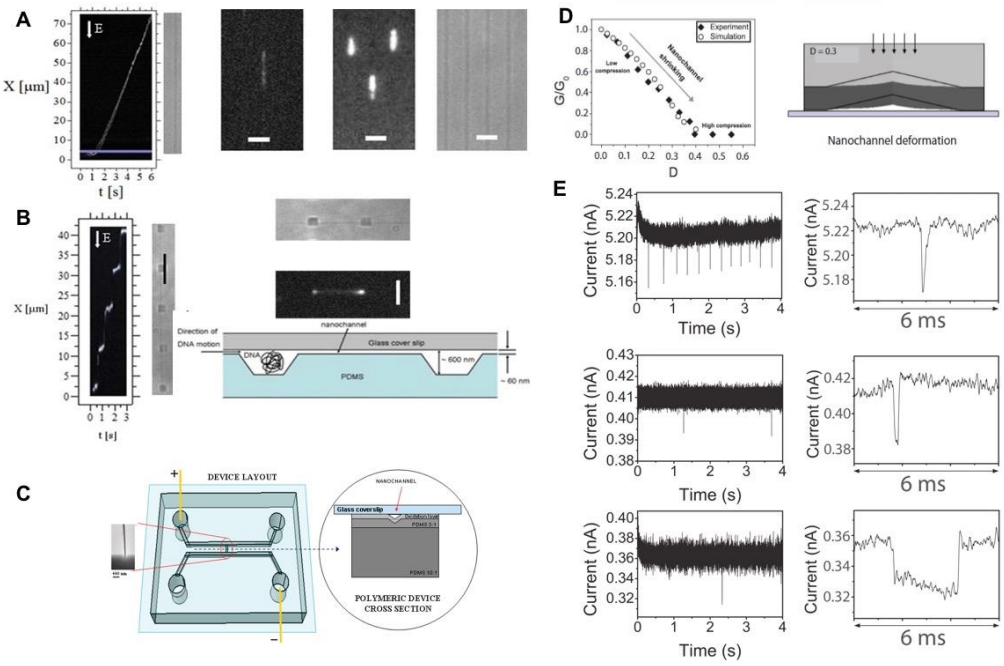

Figure 1–5 (A) Intensity time trace of a single l-DNA molecule entering and passing through a nanochannel (nearly 280 nm deep and 1 mm wide) reported in the bright field image on the right of the graph. The image shows the entrance of the nanostructures. The plot shows the intensity along the channel (X axis) versus time t. At t . 0 the molecule approaches the entrance (blue line) and starts to stretch to enter the nanochannel driven by an electric field of 130 V cm_1, at t . 1.5 s the molecule is completely inserted inside the nanostructure, where it acquires a stretched configuration, then it passes along the entire length of the nanochannel with nearly constant speed. l-DNA molecule elongated inside a nanochannel nearly 130 nm deep and 650 nm wide (scale bar 3 mm). Three l-DNA molecules confined by nanochannels (nearly 280 nm deep and 1 mm wide, scale bar 3 mm (B) Intensity time trace of a single l-DNA molecule migrating through a sequence of shallow and deep regions (a bright field image is reported on the right of the graph). At t = 0 the molecule is inserted in a deep region where it has a coiled conformation, then it stretches to pass through a thin nanochannel (nearly 60 nm deep), once it reaches a deep region it tends to recover a coiled configuration and its migration speed slows down. This behavior repeats regularly along the nanostructures sequence driven by an external voltage of V = 50 V. A bright field image of this periodic nanofluidic system is reported on the right of the graph.

Snapshot of a l-DNA molecule passing through the structure reported in (scale bar 3 mm) Cross sectional diagram of the nanostructures. (C) Device layout. On the left, sketch of the top view of the device layout: two microchannels are connected by a single nanochannel (which is shown in the SEM image) and two electrodes (yellow) allow applying the voltage and collecting the ionic current. On the right, a cross section of the polymeric device in correspondence of the blue arrow (where the triangular nanochannel is present): a thick PDMS 10:1 layer supports a thin PDMS 3:1 layer which reproduces the nano and micro features. An oxygen plasma treatment causes the formation of an oxidation layer and allows bonding the polymer with a glass cover slip in order to close the fluidics. Squeezing experiment. (D) Conductance G normalized to its zero-displacement value G0 plotted versus compressive strain D, experimental data (squares) and simulations of the device (circles) Simulated profile of the nanochannel for D = 0.3; the bulk PDMS layer and the oxidation layer domains are represented in light and dark grey, respectively. The not deformed channel shape is indicated by a black line. E) DNA detection. Current traces recorded after the insertion of a solution containing l-DNA molecules for (a) D = 0, (b) D = 0.3 and (c) D = 0.35. Magnification of a single translocation event for (d) D = 0, (e) D = 0.3 and (f) D = 0.35. All current traces were acquired applying a voltage bias of 200 mV. Copyright Lab-on-a-Chip

Compression stress was defined as, $D = \Delta L/L_0$ where L_0 is the initial position when there's no force applied and ΔL is the displacement from the initial position (see Figure 1–5D). The device was filled with 1 M KCl solution and ionic current was measured using a patch clamp with two Ag/AgCl electrodes. Translocation of λ-DNA was detected at 3 different strain levels (D = 0.0, 0.30 and 0.35) under a 200 mV bias voltage and the peak shape was analyzed (Figure 1–5E). It was shown that the peak width corresponding to a translocation time (Δt) increased with the applied strain. Also, from their findings, they deduced that Δt decreased with the applied bias voltage (V) due to enhanced molecule velocity. From these results, they were able to conclude that increasing the strain on the device, thus reducing the channel dimensions, could increase the translocation times of the DNA. Accordingly, they suggested that the DNA molecule changed its conformation when it passed through the nanochannel, which may directly translate to its translocation times. When there was no compression on the nanochannels, DNA molecules changed their structure to a blob configuration, suggested by the de Gennes model. Conversely, at a higher nanochannel compression, DNA changed to a more linear configuration as predicted by the Odijk model. They speculated that when the DNA molecule unwound, its blobs when entering narrower nanochannels, spent more time to pass through the nanochannel increasing the translocation time.

In another study, Manneschi *et al.*[150,151] reported the role of surface charge of the nanochannels and ionic strength of the buffer effecting the elongation of confined DNA. Their numerical simulations suggested that electrostatic interactions with the nanochannel wall was crucial in increasing the elongation of DNA. For the DNA experiments, they used PDMS devices populated with nanochannel arrays that were 200 nm deep and 2 μm wide. Nanochannels were triangular shaped and negatively charged. DNA solutions were prepared in KCl (pH= 8) with 0.1 μg/mL concentration. Buffer molarity was varied (0.1 M, 0.01 M and 0.001 M) and as expected they observed an increase in DNA elongation with decreased ionic strength of the buffer. They suggested the DNA molecule could be completely stretched even in a 200 nm nanochannel by decreasing the ionic strength of the buffer. Moreover, this effect was higher in triangular shaped nanochannels due to the depletion zones near the nanochannel walls, especially in sharp corners.

PMMA and COC nanofluidic devices have been used for DNA elongation as well. Thamdrup *et al.*[154] measured the extension of DNA compared to theoretical models using T4 DNA (166 kbp; 54 μm in length). According to their theoretical calculations, dye-labeled T4 DNA (1 dye: 5 bp) has a contour length of 70 μm and a persistence length of 62 nm. For their experiments, DNA was electrophoretically driven one at a time into PMMA nanochannels (250 nm x 250 nm). DNA extension (L_{ext}) was recorded at three different locations from the entrance of the nanochannel (100, 250 and 400 μm) for 10 different molecules (Figure 1–6A). The average extension length (L_{av}) of λ-DNA was found to be 13.5 ± 0.5 μm, which agreed well with the calculated extension length (13.6 μm; 24% of the dye labeled T4) predicted from the deGennes model. The uncertainty of the average extension length was given by u_{av}; $u_{av} = \sigma_{av}/\sqrt{N}$, where N is the number of frames analyzed. As they suggested, average DNA extension deviation (σ_{av}) was strongly dependent on small thermal fluctuations around L_{av} that could be suppressed by analyzing multiple frames. Other factors such as variation of cross-sectional dimensions of the polymer

nanochannels, variation of the degree of interaction and the existence of several different lengths of DNA molecules may also contribute to the variation of L_{av}.

In 2011, Utko *et al*.[49] was able to produce different nanoscale arrays of channels by injection molding onto a thick COC disk (diameter = 50 mm). Three different arrays of nanochannels were produced, each

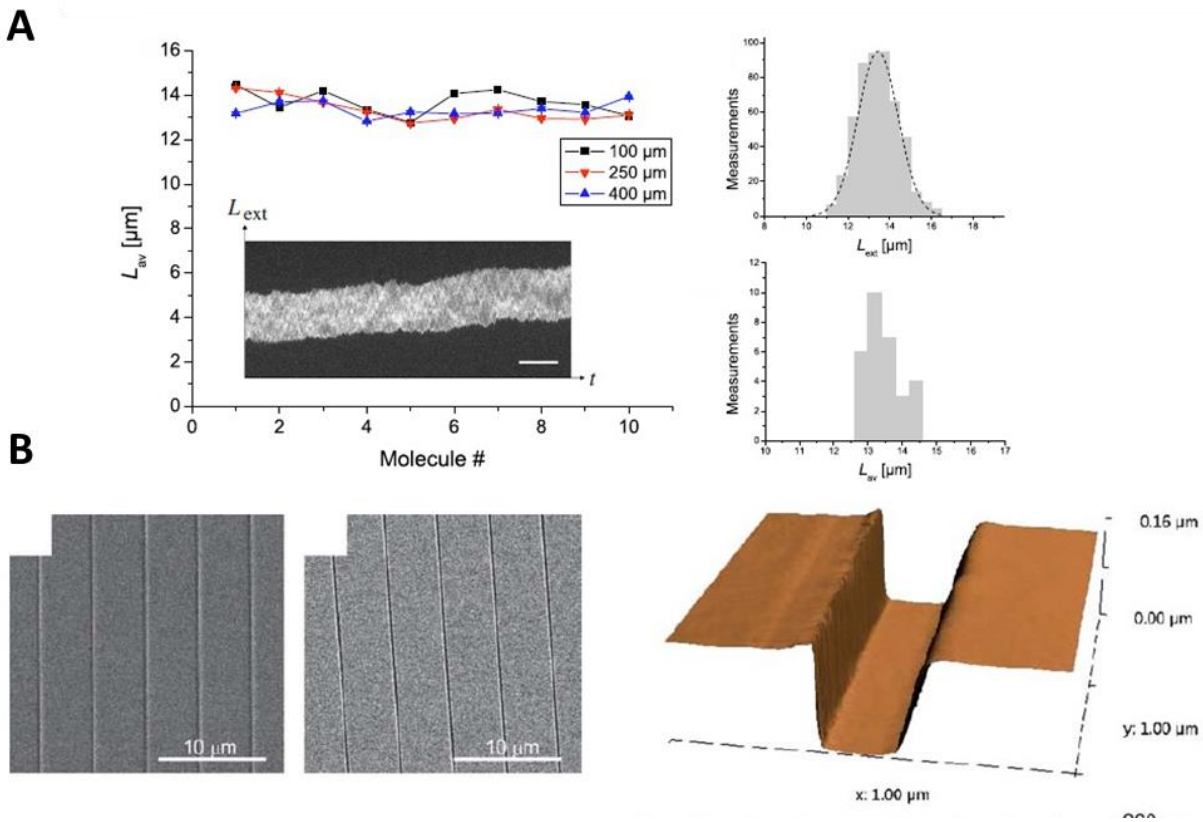

Figure 1–6 (A) (a) Graphs showing the average extension length Lav of 10 different T4 DNA molecules. Lav has been measured 100, 250 and 400 µm from the nanochannel entrance for each molecule. The inset shows a typical intensity time-trace of a T4 molecule confined inside a PMMA nanochannel. The scale bar is 10 µm and the time span is 50 s. (b) Histogram of the measured extension lengths Lext of DNA molecule 2 positioned 100 µm from the nanochannel entrance. The average extension length, based on an analysis of 500 consecutive frames, Lav = 13.4 µm and the standard deviation σav = 1.0 µm. The dashed line shows the Gaussian curve fit. (c) Histogram of the measured average extensions lengths Lav presented in (a). The overall average extension length is 13.5 µm with a standard deviation of 0.5 µm. (B) (a) SEM micrograph of a nickel plate with an array of 240 nm wide and 150 nm high protrusions. (b) Corresponding nanochannel array injection molded in Topas 5013. To avoid charging effects during

SEM imaging, the chip surface was sputtered with 5 nm of gold. (c) Three dimensional AFM image of a channel segment, taken for the same array as in (b). Copyright IOP publishing group

with an array consisting of 80 nanochannels; 400 nm wide straight channels, 240 nm wide straight channels and tapered nanochannels with decreasing width from 1040 nm to 140 nm; in all cases the depth was 150 nm (Figure 1–6B). Nanochannels were sealed with a 150 μm thick COC plate using thermal annealing. For the extension experiments, λ-DNA in 0.5x TBE buffer was used and the DNA were electrophoretically moved into the channel and the field was turned off to leave the molecule stationary within the nanochannel. Fluorescence data was recorded at 10 frames-per-second per 100 frames per molecule. Intensity over the DNA molecule in each frame was fit to a Gaussian point-spread function to extract its position and extension in each frame, which was then mapped to a specific location in the nanochannel. To verify the usability of COC, they studied the autofluorescence intensity of COC by bleaching nanochannel areas by exposing it to a 200 W halide lamp for 20 min and did not find significant bleaching. Their DNA stretching results suggested that the difference in the DNA extension was not only due to thermal fluctuations along the nanochannel, but also associated with the imperfection of the nanochannel profiles. The cross sectional geometric average of the rectangular channel was given by, D_{av} = √d*w (square root of the multiplication of width and depth of the channel). Extension of the molecule (r) can be represented as a function of D_{av}. The average extension of the DNA (r) was increased with the decreasing channel heights according to the results obtained from the tapered nanochannels. They measured the extension of DNA at 3 different locations (D_{av}= 181, 212 and 250 nm) and calculated the power law dependence according to the equation $r \propto D_{av}^{-\alpha}$. They found α = 0.76 ± 0.05, which agreed very well with the results collected using fused silica devices (α = 0.85 ± 0.01), thus confirming COC as an ideal substrate for DNA elongation experiments.

Soper and coworkers explored DNA stretching in thermoplastic nanofluidic devices using both PMMA and COC substrates. Chantiwas *et al.*[53] and Wu *et al.*[99] illustrated the use of thermoplastic

nanoslits (COC) and nanochannels (PMMA), respectively, for DNA stretching. Chantiwas *et al*.[53] reported that the low EOF in COC devices negated the need for an EOF suppressor compared to glass-based devices. At 25 V/cm, translocation velocities of λ-DNA were found to be 8.23 ±0.74 × 10^{-4} cm^2/Vs for PMMA and for COC devices, it was 7.62 ±0.65 × 10^{-4} cm^2/Vs in 7 μm wide and 100 nm deep nanoslits. DNA extension lengths were measured to be 46% for PMMA and 53% for COC nanoslit devices compared to the full contour length of a dye-labeled (5:1) λ-DNA. Wu *et al.*[99] observed increased elongation of DNA in 100 nm × 100 nm (~50%) and 75 nm × 75 nm (~81%) nanochannels compared to PMMA nanoslits as would be expected because of the smaller size of the nanochannel devices compared to nanoslit devices.

Uba *et al*.[74] recently discussed differences in the transport dynamics of λ-DNA in surface modified thermoplastic nanoslits and nanochannels compared to glass nanofluidic devices. Stretching of DNA in its relaxed state was measured in the absence of an electric field. According to the deGennes theory, stretching of ~25% for λ-DNA would be predicted in a 100 nm × 100 nm nanochannel. They observed an elongation length of 6.88 μm (34%), which was higher than that predicted according to the deGennes theory. The authors suggested that the increased stretching was due to interfacial surface forces arising from the charged nanochannel walls. One interesting discovery in this study was the presence of "stick-slip" motion at low electric fields and low buffer concentrations. In 0.5x (44.5 mM) TBE, the thickness of the EDL was calculated to be ~30 nm where they observed "stick-slip" motion with field strengths <150 V/cm suggesting the possibility for dielectrophoretic trapping. At low buffer concentrations, there would be an increase in the electric double layer thickness. From classical theory, it was predicted ~30 nm for 0.5x and ~8 nm for 2x TBE. When a charged molecule is in intermittent motion inside a nanochannel with a thick EDL, the interfacial forces could likely be higher than the driving force, resulting in "stick-slip" motion. At higher buffer concentrations (2x TBE, 180 mM), DNA

velocity had a linear increase with electric field strength suggesting the absence of dielectrophoretic trapping due to smooth channel walls.

1.4.2 Nanofibers for DNA Analysis

Bellan *et al.*[155] used a different approach to stretch DNA using a polymeric nanofiber. Polyethylene oxide (PEO) nanofibers were electrospun using a scanned electrospinning method. The resulting fibers, ranging from 100 – 350 nm, were spun onto a glass cover slip and the stretching of λ-DNA within these PEO nanofibers were imaged. The lengths of λ-DNA stretched inside these nanofibers were collected and measured. With a labeling ratio of (4:1) the full contour length of the DNA is expected to be 18.8 μm. They noted that the stretched length is roughly a constant along the length of a given fiber. Variations between the fibers are resulting from the electrospinning setup and the jet velocity. To understand the DNA behavior in PEO they performed an experiment in a fused silica microchannel (50 μm wide and 750 nm deep) filling the viscous electrospinning solution with DNA. Under an applied electric field (100 -200 V/cm), DNA was elongated and once the field is off, it relaxes in to a blob. This behavior was recorded and the time it takes to relax in the channel was found to be 2.1 – 19.0 s over 20 samples with a mean relaxation time of 8 ±5 s. The overall strain from the electrospinning jet are above the order of the required magnitude for the DNA to scission while elongating thus it is expected some fragmentation during the spinning process. If this method could be improved to embed DNA molecules linearly preventing any fragmentation, it is possible to perform biological studies such as Fiber-FISH using polymer nanofibers.

1.4.3 Genomic Mapping within Thermoplastic Nanochannels

One application of DNA stretching within nanochannels is genomic mapping.[156-158] Genomic (genetic) mapping can provide valuable information such as diseases transmitted from generation to generation, which are related to one or more genes. It also provides evidence about which chromosomes are carried in the gene and precisely where the gene is located in the chromosome. This

provides a perfect platform to identify disease stages accurately by mapping the relevant disease-associated genes. For mapping, molecular markers are used to label specific sites within the genomic DNA extracted from patient samples. Increasing the resolution of the map and preventing it from being saturated increases the quality of the genetic maps.

In order to facilitate mapping of specific sites within genomic DNA, it is important to stretch the DNA to near its full contour length. Moreover, it is crucial that the imaging of specific sites within the DNA can be resolved with high optical clarity. Devices with high resolution imaging capabilities to identify specific targeted sites with fluorescent tags would be ideal for this purpose. Currently, commercial devices such as that marketed by BioNano Genomics, are able to fabricate these devices in Si using deep UV lithography.[158,159] For example, Das *et al.*[160] used a Si device bonded with glass to identify specific sequence variations in stretched DNA, which would eventually be applied to map the whole genome. They investigated linearized 115 kbp circular DNA BAC clone of MCF7-3F5 cells in 60 nm × 100 nm nanochannels by achieving ~65% DNA stretching with respect to its full contour length. The authors were able to identify 4 specific nick label sites within a DNA molecule. Even though optical genomic mapping has been reported on Si-based devices, it is yet to be reported in thermoplastics.

In order to fabricate devices for optical genomic mapping in thermoplastics, one needs to build nanofluidic devices with nanochannels smaller than the persistence length of DNA (~50 nm) and should utilize a thermoplastic with high optical clarity to enhance the resolution. Soper and coworkers recently developed a simple hybrid bonding method in order to facilitate thermoplastic devices with nanochannels on the order of less than 50 nm that could be used for genomic optical mapping.[87] They used a substrate with high T_g where the structures are imprinted and used a lower T_g material to seal the devices thus ensuring no deformation of the nanochannels. Figure 1–7A shows the stretching of T4 DNA in different sizes of nanochannels. In all cases the signal-to-noise (SNR) ratio was improved in the hybrid device with a COC cover plate compared to devices with a PMMA cover plate due to the lower

autofluorescence properties of COC.[161] Furthermore, as expected, data reveals that the stretching in nanochannels increases with the decreasing channel size, D_{av}. Figure 7B shows the DNA extension (ε) changes with $D_{av.}$ Theoretical de Gennes regimes are shown in red dashed line and Odijk regime was represented in blue dashed line (see Figure 1–7B). When the D_{av} is larger than 200 nm, the experimental extension curve fits well with the de Gennes regime and when the D_{av}= 35 nm, it perfectly fits with the Odijk regime. However, stretching in nanochannels with dimensions of 190 × 95 nm, 150 × 60 nm and 110 × 25 nm, results in stretching that does not fit with either regime, rather it falls between the two regimes Figure 1–7A; nc3 to nc5). Authors suggest the deviation may arise from the surface charge between the channel walls and the molecule. Nanochannels with dimensions of 35 nm × 35 nm showed the highest stretching of T4 DNA, thus proving the usability of the sealed thermoplastic hybrid device for reading specific sites in DNA by stretched them close to the DNA's full contour length.

1.4.4 Nanopore Devices for Biosensing

Much research investigating the use of thermoplastics for non-DNA interrogation seeks to imitate the biological pores located within cell membranes that are comprised of protein complexes that react to stimuli in the environment. Thermoplastic nanodevices have tunable surface chemistry, great physical stability, and mechanical robustness, thus allowing for excellent control to mimic biological ion channels as well as for specific surface functionalization to develop specific biosensors.[162]

Many approaches for interrogating various biological molecules, such as metabolites and proteins, utilize asymmetrical chemical etching of PET films[98,162-164] to generate a carboxyl terminated, conical nanopore with "tip" dimensions of 5-30 nm and base dimensions of 300-1000 nm. Characterization of ligand binding is accomplished by monitoring the current response to an applied voltage. Ali *et al.* utilized the negative charge on the surface of a polymer for the electrostatic self-assembly of a positively

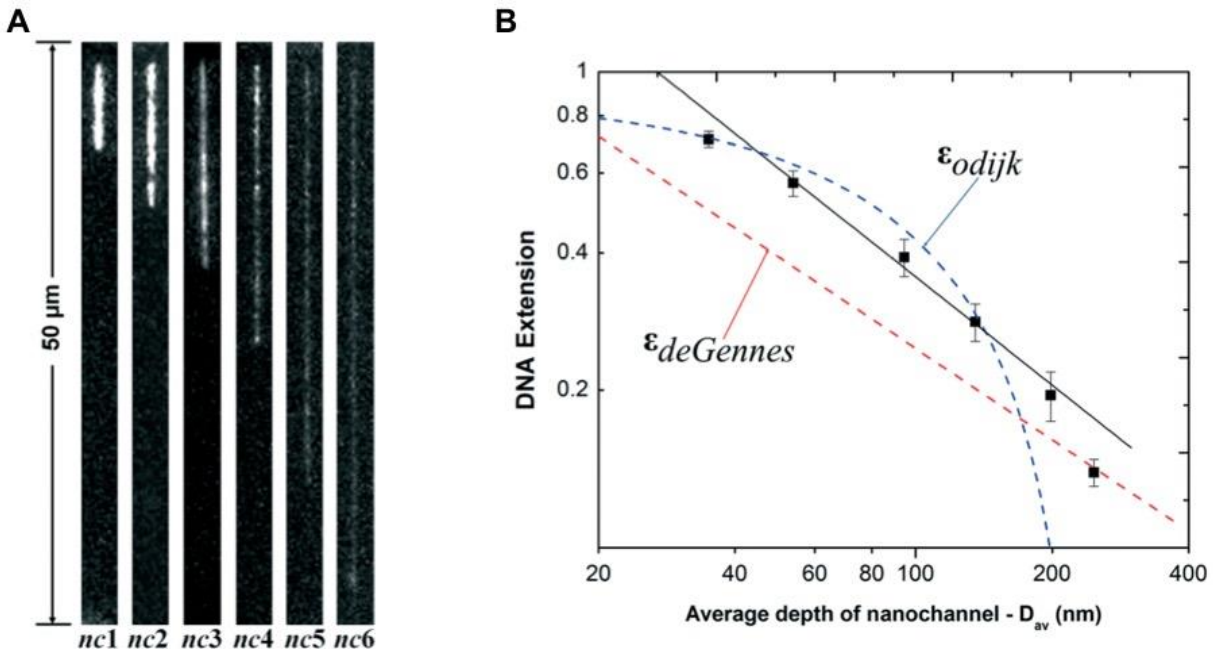

Figure 1–7 (A) Unprocessed representative frames of T4 DNA molecules elongated in enclosed nanochannels for the hybrid devices. Images were acquired at 10 ms exposure time with the driving field turned-off. Note that nc6 = 35 × 35 nm. (B) Log-log plot showing the T4 DNA extension as a function of the geometric average depth of the nanochannels. The DNA extension was normalized to a total contour length (Lc) of 64 µm for the dye-labeled molecules. The red and blue dashed lines are the deGennes and Odijk predictions, respectively. The black solid line is the best power-law fit to the data points obtained from the nanochannels with an average geometric depth range of 53 nm to 200 nm. Copyright Lab-on-a-Chip

charged biorecognition element (Figure 1–8B).[164] Current-potential (I-V) curves confirmed the self-assembly of these biorecognition molecules and the binding of a specific ligand led to a change in the effective cross section and thus a detectable decrease in current for concentrations as low as 1 pM. Hou *et al.*[162] utilized a similar approach to develop a thermoplastic nanopore glucose detector. Glucose oxidase was covalently attached to –COOH functional groups on PET through classically used EDC/NHS chemistry (Figure 1–8A). The I-V plots confirmed the functionalization of the device as well as indicated ligand binding. However, they observed an increase in current upon ligand binding, which was explained by a decrease in the pH after the catalytic enzyme reaction resulted in the protonation of the surface and greater anionic transport. This assembly was selective only for the ligand specific to glucose oxidase.

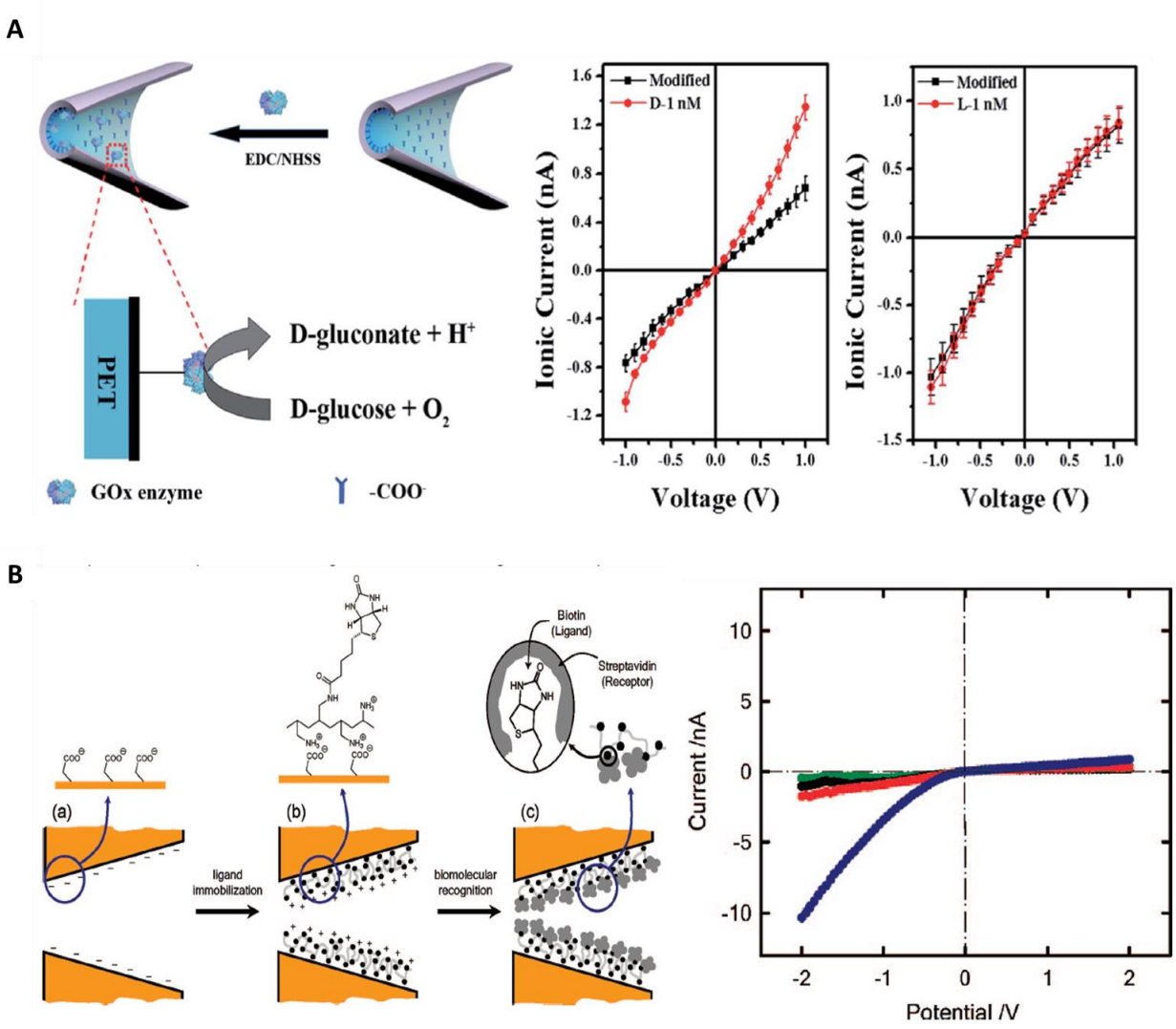

Figure 1–8 (A) Hou et al. schematic representation of an ultratrace D-glucose detector (left panel) with I-V characteristics of a channel filled with 0.1 M KCl and 1 nM D-glucose. (B) Ali et al. carboxylate-terminated nanopore used as a platform for the electrostatic immobilization of the bifunctional macromolecular ligand, b-PAH with the biorecognition event proceeding in the presence of the receptor (streptavidin) (left panel). I-V plots of a b-PAH-modified single conical nanopore in 0.1 KCl in the presence of different concentrations of streptavidin (SAv): (dark blue) no SAv; (red) 1 pM; (black) 10 pM; (green) 100 pM.

Further modification of PET nanopores was reported by Hou *et al.*[163] The resulting device was coined as a "smart" nanopore with an asymmetric design to respond to both changes in pH and temperature. One side of a fabricated PET nanopore was treated by plasma-induced grafting of N-isopropylacrylaminde (NIPA), which is a temperature responsive polymer, poly(N-isopropylacrylamide)

(PNIPA) after polymerization. The other side was treated with acrylic acid (AAc), which is a pH responsive polymer, poly(acrylic acid) (PAA), after polymerization. With this device, they were able to observe both temperature and pH mediated ionic transport of KCl solutions.

Even further complexity was described by Zeng *et al.*[165] who utilized multiple asymmetric nanochannels in both parallel and serial modes to mimic the true multiplex nature of ion channels within a membrane. They were able to regulate the transport of KCl solutions within the network of nanopores even controlling the ionic current rectification.

1.4.5 Thermoplastic Devices for Nanoelectrophoresis

As previously discussed, unique phenomena such as EDL overlap and increased surface area to volume arise in the nano-domain. For this reason, much effort has moved to the investigation of separations on the nanoscale. Research has mainly focused on the use of fused-silica nanochannels due to the well characterized surface chemistry that is highly ordered and homogenous; however, fabrication of these devices is costly and time consuming, thus investigations of thermoplastic nanochannels for nanoelectrophoresis are developing. Furthermore, investigation to understand of the effects of thermoplastic surfaces on nanoscale separations has been performed.

O'Neil et al.[71] utilized Super Resolution Microscopy to explore the heterogeneity of activated COC and PMMA substrates to understand the density and distribution of generated surface confined –COOH groups on these thermoplastics. They show that generated –COOH functional groups are heterogeneous in nature and both the relative density and distribution are dependent on the activating dose used. COC demonstrated relatively higher surface density when compared to PMMA (Figure 1–9A). COMSOL investigations into the contribution of this heterogeneous distribution of surface charge indicated that EOF distortion is possible; however, the lower surface charge density, compared to glass, led to an overall lower EOF, thus an expected minimal contribution to zonal dispersion because the particle's electrophoretic mobility would likely dominate (Figure 1–9B). They confirmed this finding by

performing nanoscale electrophoresis within COC nanoslits of fluorescently labeled polystyrene (PS) particles. Evidence of stick/slip motion was observed at low field strength (200 V/cm) leading to a longer migration time and greater dispersion. At higher field strengths (300 V/cm) particles were seen to transverse the channel with fewer wall interaction leading to a fast translocation time and less dispersion. The translocation of the PS particles from cathode to anode confirmed that the electrophoretic mobility of these particles was greater than the EOF, leading to minimal dispersion effects due to surface charge heterogeneity at higher field strengths.

Weerakoon-Ratnayake *et al.*[166] investigated the separation of silver nanoparticles (AgNP) within nanoscale PMMA columns. Dark field microscopy was used to track the transport of AgNPs within these devices with varying slit dimension, buffer ionic strength and applied field strength. The authors were able to demonstrate the separation of AgNPs based on size without the addition of buffer additives, which was not possible within micro devices. The best resolution was achieved at higher field strengths, which is not possible in micro-scale due to Joule heating where in this case it was minimal (Table 1-2). Lower field strengths (<200 V/nm) caused decrease of resolution and plate numbers due to the presence of stick/slip motion of the AgNPs (Figure 1–10). They also investigated the diffusion effects in the nano-domain by comparing the molecular diffusion coefficient (D_T) to the effective diffusion coefficient (D_{eff}) and calculating the ratio; $\Delta=D_{eff}/D_T$. Other dispersion factors such as Taylor dispersion, wall-particle interactions, Joule heating, which was minimal in the nanochannel, may cause D_{eff} to differ from D_T.

Depth of Nanoslit	150 nm		150 nm		400 nm	
Citrate Buffer Concentration	2.00 mM		0.05 mM		0.05 mM	
Particle Size (nm)	60	100	60	100	60	100
Field Strength (V/cm)	Plate Number (N)					
100	723	694	303	233	422	371
200	987	1,320	486	570	737	1,090
500	2,350	3,000	1,220	1,200	1,750	2,320
1500	6,800	9,270	4,370	4,250	5,100	6,370
Field Strength (V/cm)	Resolution (R)					
100	0.089		0.022		0.58	
200	0.77		0.33		0.26	
500	0.57		0.74		0.51	
1500	0.67		1.1		0.61	

Table 1-2 Electrophoretic Parameters for 60 and 100 nm AgNPs at Different Nanoscale Electrophoresis Operating Conditions

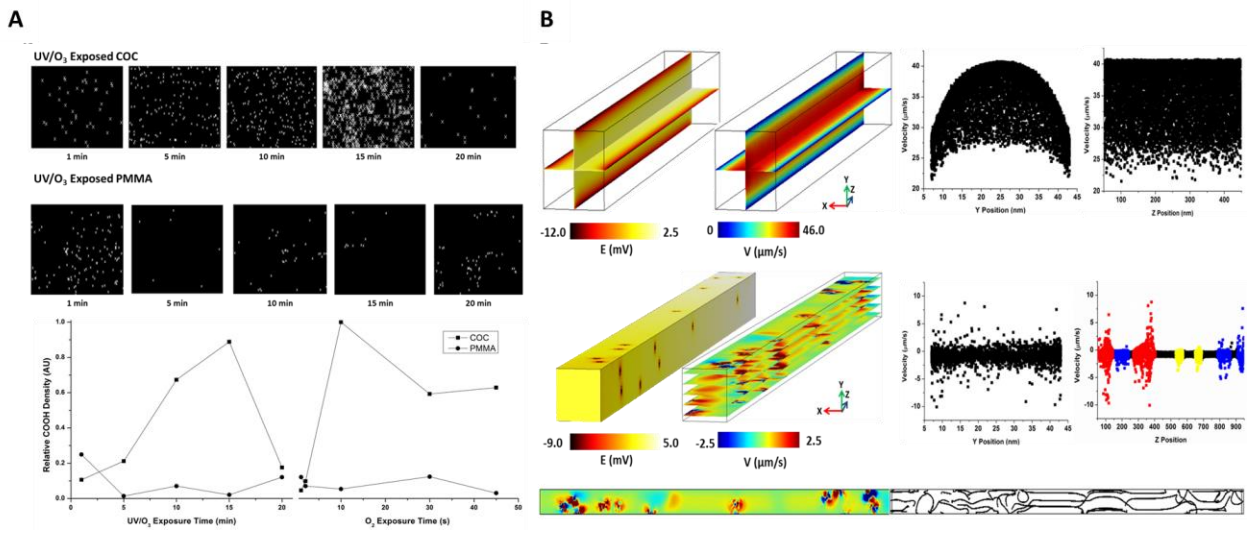

Figure 1–9 (A) Representative STORM images of 1 µm2 (top) COC and (bottom) PMMA exposed to 1, 5, 10, 15, and 20 min UV/O3 radiation, respectively. Relative −COOH density vs exposure time for (left line graph) UV/O3 and (right line graph) O2 plasma-modified COC (closed squares) and PMMA (open circles). Lines are for visual purposes only. UV/O3 and O2 plasma exposure conditions were kept constant (see text for details). All total localizations were normalized to the greatest localization density, COC exposed to 10 s of O2 plasma. (B) (top left) COMSOL simulation showing the electric potential (left) and velocity magnitude (right) for a channel with uniform surface charge; (top right) Velocity vs axial (right) and longitudinal (left) position to show the EOF flow profile for a channel with uniform surface charge; (bottom left) COMSOL simulation showing the electric potential (left) and velocity magnitude (right) where single point charges are mapped onto the nanochannel surfaces using the −COOH locations (centroids) obtained by STORM analysis of a COC surface exposed to 5 min UV/O3 activation. (bottom right) Velocity vs axial (right) and longitudinal (left) position to show the EOF flow profile for the channel with non-uniform surface charge. The colors in the velocity vs Z position graph (right) represent an area in the channel with >5 (red), 3−4 (blue), and 1−2 (yellow) −COOH group(s) within 20 nm of each other; (g) One slice of the velocity profile to show fluid flow recirculation; (h) Streamline of the same velocity slice depicted in (e) to emphasize the fluid recirculation at areas with −COOH. Copyright American Chemical Society

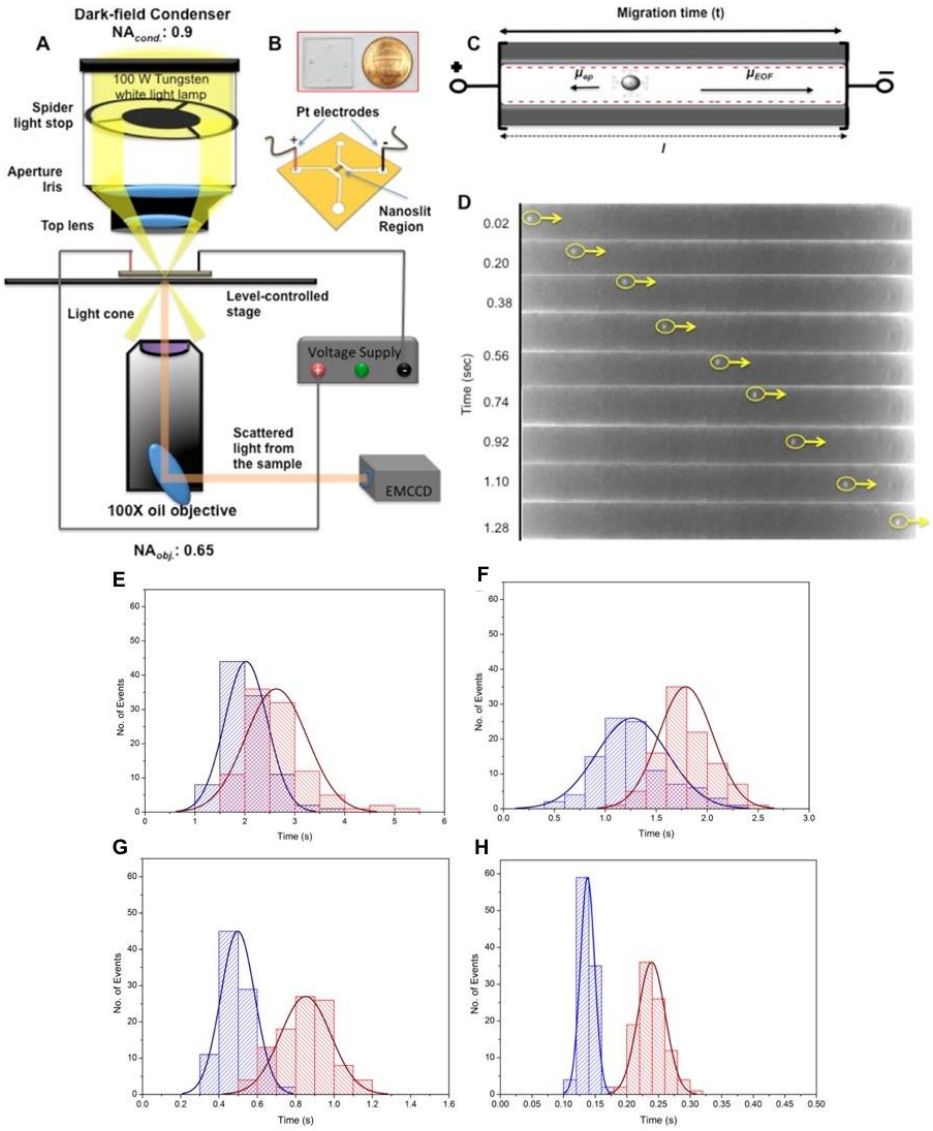

Figure 1–10 (A) Schematic of the dark field microscope and the experimental setup. The sample was mounted on a level-controlled microscope stage. While the spider stop controlled white light missed the objective, only scattered light from the sample entered the objective. (B) Image of the PMMA nanofluidic chip and a schematic of the device with nanoslits. (C) Schematic of the nanoslits when an external electric field was applied. Electroosmotic flow was from anode to cathode while the electrophoretic mobility of negatively charged AgNPs was toward the anode. (D) Representation of a translocation event for a 60 nm AgNP in a nanoslit. Time-lapse image sequence of the single AgNP event at an external field strength of 200 V/cm. The particle translocation direction was from anode to cathode (same direction as EOF) with a translocation time for this event of 1.3 s. Dimensions of the nanoslits were 100 µm in length and 150 nm in deep. Histograms of translocation events for 60 nm AgNPs (blue) and 100 nm AgNPs (red) in 150 nm nanoslits with a running buffer of 0.05 mM citrate. Each histogram includes 100 events at a bias voltage of (E) 100 V/cm, (F) 200 V/cm, (G) 500 V/cm, and (H) 1500 V/cm. Note that the time axes have different scales depending on the electric field. Copyright American Chemical Society

From their results, it was evident that Δ values were >10 for all cases. They suggested that $D_{eff} > D_T$ because of the contribution to zonal variance arising from different zeta potential (ζ) of the particles, Henry's function (f_H), double layer thickness (λ_D) and particle radius (r) values.

Next generation sequencing (NGS) by time-of-flight (ToF) strategies is an immerging field of research. Nano-circuits with entropic traps and pillars capable of manipulating, storing and elongating DNA are of interest for enabling NGS in micro and nanofluidics. Oliver-Calixte *et al.*[167] has shown the capability of immobilizing λ-exonuclease enzyme onto PMMA micropillars to provide a platform for new sequencing strategies by clipping mononucleotides and separating them based on their electrophoretic migration behavior in nano-electrophoresis columns (Figure 1–11A). Several simulation studies have shown the possibility of the electrophoretic separation of single nucleotides using nanochannels smaller than 5 nm.[168,169] Novak *et al.*[168] suggested the possibility of separating deoxynucleotide 5'-monophosphates (dNMPs) within a 5 nm wide channel with hydrophobic (carbon) walls under hydrodynamic flow based on their electrophoretic migration behavior (Figure 1–11B). Their study, based on the adsorption/desorption properties of the dNMPs, was able to demonstrate the separation of most hydrophobic dTMP and most hydrophilic dCMP while transporting through carbon nanotubes, thus suggesting that controlling the wettability of the surface may be a reliable way to separate dNMPs through nanocolumns. In a more recent article, Xia *et al.*[169] showed separation of dNMPs under high electric field strengths and varying roughness of the nanocolumns. They observed a change in the elution order of the dNMPs depending on the roughness of the nanochannels walls. It was evident that by changing the wettability and roughness of the nanochannel walls, dNMPs could be separated based on their molecular dependent electrophoretic migration behavior.

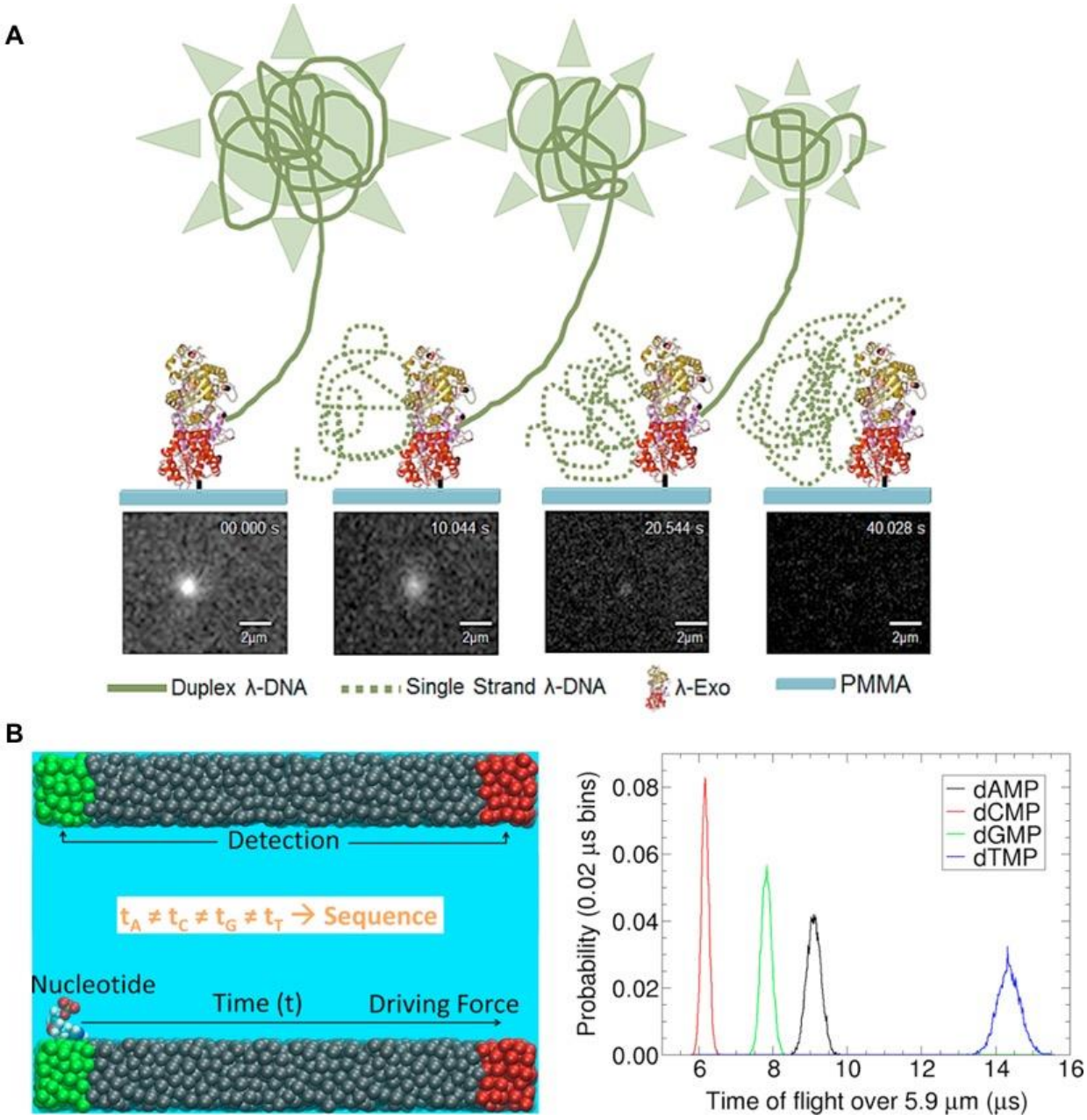

Figure 1–11 (A) Representative schematic of λ exonuclease immobilized on to a PMMA surface as it processively cleaves dNMPs from double stranded DNA to generate single stranded DNA as a product. Fluorescence images showing the digestion of dsDNA by λ exonuclease images showing the digestion of dsDNA by λ exonuclease immobilized onto a PMMA surface. (B) Molecular dynamic simulations of the translocation of dNMPs within nanochannels showing the elution order and subsequent separation of dCMP, dGMP, dAMP and dTMP within a nanochannel. Copyright American Chemical Society

1.4.6 Other Applications of Thermoplastic Nanochannels

Thermoplastic nanofluidic devices have also been used for the electrochemical detection of small molecules,[170] investigation of enzyme reaction kinetics[171] and identification of single nucleotide polymorphisms (SNP).[172]

Liu *et al.*[170] developed a protocol for the integration of microelectrodes on a PMMA nanofluidic device for the electrochemical detection of biotin at concentrations as low as 1 aM. This device was combined with nanoparticle crystals and the use of a PMMA substrate, when compared to glass, showed better signal-to-noise and a higher sensitivity with easy fabrication.

Wang *et al.*[171] fabricated a y-shaped nanofluidic chip in polycarbonate (PC) and sealed the device with polydimethylsiloxane (PDMS). This y-shaped device was used to allow homogenous mixing of an enzyme and ligand to observe "free state" enzyme reaction kinetics in nano-confinement (Figure 1–12B). Glucose oxidase and D-glucose were chosen as the model enzyme-ligand pair. The reaction product, hydrogen peroxide (H_2O_2) was electrochemically detected and it was determined that the "free state" activity increased significantly compared to the immobilized and bulk solution enzyme.

Yang *et al.*[172] fabricated an ultrahigh density array of nanochannels with carboxyl terminated PMMA for the immobilization of molecular recognition agents (MRAs) (Figure 1–12A). An oligodeoxynucleotide (ODN-A) labeled with carboxy-fluorescein was immobilized on nanochannels walls and hybridized with rhodamine labeled ODN-B, forming a 14 base pair double stranded DNA with 5 unhybridized bases to be used as the MRA. Target single stranded DNA molecules were passed through the nanochannels and allowed to interact with the double stranded DNA complexes. Displacement of the

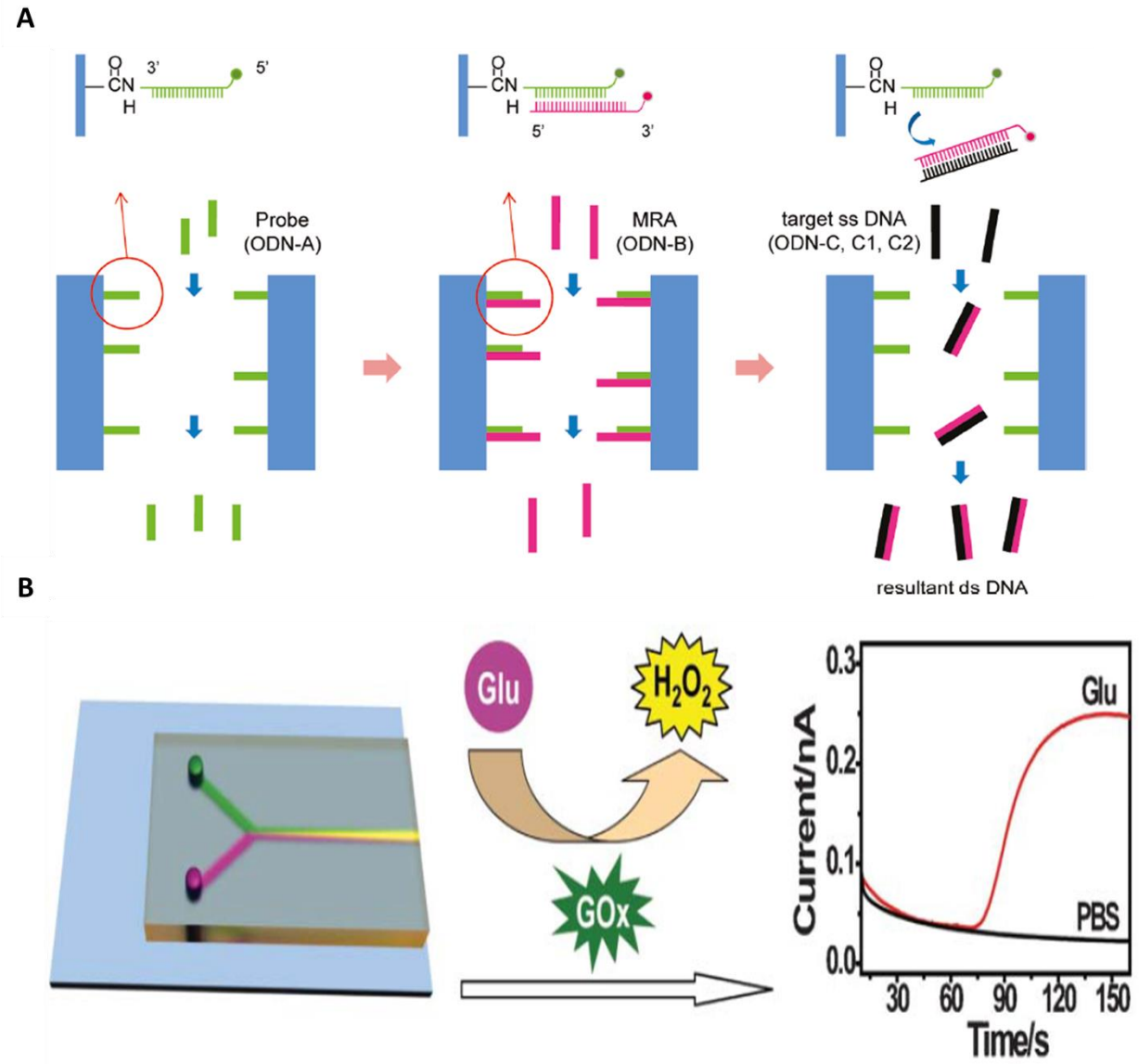

Figure 1–12 (A) Yang et al. schematic illustration for SNP detection based on molecular recognition using DNA-functionalized nanochannels. (B) Wang et al. schematic layout of the nanofluidics chip. Green and pink colors denote enzyme and substrate, respectively; yellow denotes the reaction product. The product of the enzymatic reaction, hydrogen peroxide, can be electrochemically determined as indicated by the rise of the current when the substrate, glucose, is introduced. The working electrode is aligned to the end of the nanochannel with a distance of 20 mm.

ODN-B from the nanochannels varied depending on the thermodynamic stability of the newly formed double stranded DNA, which was determined by the presence and location of SNPs on the target DNA. This device was able to detect SNPs as well as discriminate SNPs at various locations with high sensitivity. They utilized the nanochannels to detect SNP in alcohol dehydrogenase 2 (ALDH2) which can be used for the evaluation of organ susceptibility to alcohol damage. The sequence containing one SNP

showed a 50% higher displacement of the oligodeoxynucleotide probe, thus allowing for the identification of wild type and SNP DNA.

1.5 Conclusions

Nanofluidics is an emerging field offering unique possibilities not afforded when using microscale devices for molecular analysis. Operating in the nano-regime allows for the interrogation of biopolymers such as DNA at the single-molecule level, mimicking of biological pores for the evaluation of various metabolites, separation of various analytes without the addition of buffer additives among many other applications, all of which may be useful in the development of diagnostic devices. Because of the potential for these devices, fabrication of these devices must be realized to deliver devices that are inexpensive and show high fidelity making the use of thermoplastic substrates ideal for nanofluidic applications. This paper has presented an overview of recent advancements in the fabrication, assembly and surface modification and characterization of thermoplastic nanofluidic devices as well as showed the vast applications of such devices.

CHAPTER 2. INTERROGATING SURFACE FUNCTIONAL GROUP HETEROGENEITY OF ACTIVATED THERMOPLASTICS USING SUPER-RESOLUTION FLUORESCENCE MICROSCOPY

2.1 Introduction

Thermoplastics are an attractive material for both microfluidics and nanofluidics.[173-176] The interest in thermoplastics stems from the fact that both microscale and nanoscale structures can be produced with techniques that are conducive to high scale production of devices with high fidelity and high process yield rates.[53,77,87] Indeed, thermoplastic-based microfluidic and nanofluidic devices have been used for a variety of applications, such as microarrays,[177,178] solid-phase enzymatic reactors,[167,179,180] solid-phase extractors for nucleic acids and proteins,[181] affinity selection of biological cells,[57,182,183] chromatography,[184] and microchip electrophoresis.[161,185]

While the benefits of microchip electrophoresis have been well documented,[186-188] new efforts have been devoted to reducing electrophoresis columns to nanometer sizes, because unique phenomena specific to nano-confined domains can be exploited; thus, separations not possible in the microscale can be achieved using nanometer columns.[189-194] For example, as the channel dimensions approach the thickness of the electrical double layer (EDL), EDL overlap results in non-plug, parabolic flow profiles. Furthermore, increased surface area-to-volume ratios result in surface interactions'[4,7,66,68-70,195] giving rise to transverse electromigration (TEM).[70] Because of EDL overlap, parabolic flow profiles can be generated and with the action of TEM, separations can be undertaken that are not possible in microscale electrophoresis.[4,66,117,195-197]

Conventionally, nanoelectrophoresis is carried out using glass-based devices, which have a well characterized surface chemistry that is highly ordered and homogeneous. However, fabrication of such devices is costly and time-consuming, in many cases requiring deep UV lithography or ion beam milling

of each device.[28,33,198] In contrast, multiple thermoplastic nanocolumns can be replicated from a single master by nanoimprint lithography (NIL) reducing cost and simplifying fabrication.[53,77,199]

In general, thermoplastics can be modified to increase their surface charge density and wettability enabling the generation of electroosmotic flow (EOF).[199] Thermoplastic devices can be activated by exposure to UV/O_3 or O_2 plasma,[59] which forms oxygen-containing functionalities, including surface carboxylic acid groups (-COOH) as well as other oxygen-containing groups that are typically less abundant than the -COOH groups. The UV/O_3 activation process uses a quartz Hg lamp, which continually generates and destroys O_3 yielding a steady-state concentration of strongly oxidizing atomic O. The Hg lamp generates both 185 nm and 254 nm wavelength light. The 185 nm light splits oxygen from O_2 resulting in the oxygen atoms reacting with O_2 to form ozone while the 254 nm light breaking the O_3 in to atomic oxygen and O_2, thus yielding a steady-state concentration of atomic O. At sufficiently high energy, both UV exposure and oxidative stress can generate radicals within the polymer, which may break or scission polymer chains into smaller fragments, crosslink polymer chains, cause intramolecular rearrangements, and/or react with water or oxidative species to form carboxyls or other O-containing species.[57] O_2 plasma activation results in a source of highly energetic and reactive species that can interact with the polymer surface. Positive ions, electrons, neutral gas molecules and many other species are formed within the plasma. The energetic oxygen species created in the plasma react with polymer to form mainly water and CO_2, while the active oxygen species (radicals), bind to the active surface sites on the surface. Characterization of these activated surfaces has been demonstrated.[57,200] But, previous measurements produce ensemble results averaged over relatively large areas (1 mm^2),[57] and as such, did not address the spatial distribution of functional groups generated following activation of the polymer.[57,200]

The heterogeneity of surface functional groups following activation can have a profound impact on the electrophoretic performance of a nanoscale device. For example, heterogeneous distributions of

surface charges can generate non-uniform zeta-potentials, which are known to cause recirculation in the EOF that can degrade separation efficiency.[201,202] This issue is exacerbated when the column cross section is significantly reduced, such as is the case for nanoscale electrophoresis, due to increased interaction with the heterogeneous surface.[4,68,69]

Assuming the Debye length is significantly smaller than the width of a fluidic channel and the surface charge density is uniform along both the axial and radial dimensions, the fluid velocity within a channel (υ) can be described by the Helmholtz-Smoluchowski equation:

$$\upsilon = \frac{-\varepsilon E \bar{\zeta}}{\eta} \tag{2.1}$$

where ε is the permittivity of the buffer, E is the applied electric field, $\bar{\zeta}$ is the average zeta potential, and η is the fluid viscosity. This equation describes the classic "plug-like" flow characteristic of microscale electrophoresis.[201,203-206] However, eq. 2.1 is not applicable for the majority of nanoscale electrophoretic separations because the Debye length approaches channel dimensions. Moreover, non-uniform distributions of surface charges modulate the zeta potential so that it can no longer be averaged.

To date, theoretical and experimental investigations into the effects of non-uniform surface charge have been explored only in a few cases.[180,201,203,206,207] For example, Anderson and Idol studied EOF through pores with non-uniformly charged walls and found the mean fluid velocity to be accurately described by the Helmholtz equation when using the average zeta potential; however, recirculation of fluid was observed in regions where ζ deviated from the average.[203] Ajdari explored alternating regions of positive and negative surface charges and showed the presence of steady convective recirculation in the EOF.[206] Surface defects have also been shown to introduce non-uniform ζ with similar hydrodynamic contributions noted.[208] Several other investigations[201,204,207] relied on a step scheme in which ζ of one region was set to zero, while the downstream region had a higher ζ, thus generating recirculation at the junction, but plug-like EOF downstream.[201,206]

All of the aforementioned studies assumed that the surface charge density conforms to an

equilibrium Boltzmann distribution, which assumes thermodynamic equilibrium where the ionic distributions are uniform along the channel wall and unaffected by fluid flow.[207,209] However, this assumption is inaccurate in the case of non-uniform surface charge distribution. In these cases, it is necessary to adopt the Nernst-Plank model to account for the heterogeneity of surface charge. Fu *et al.* observed deviations from the typically used Boltzmann distribution; they also explored the effect of EDL overlap with non-uniform ζ. They showed that the velocity profiles in the regions of high and low ζ is parabolic due to EDL overlap.[207]

Investigations into the non-uniform spatial distribution of functional groups on surfaces with nm-resolution has not been explored to our knowledge. The process of activating thermoplastics with UV/O_3 or O_2 plasma may introduce non-uniform surface charges. Hence, a thorough analysis of surface heterogeneity caused by activating amorphous thermoplastic surfaces is critical to understand the utility of thermoplastics as substrate materials for nanoscale electrophoresis and other applications. Many variables can affect the heterogeneity of surface confined -COOH groups, in particular competitive chemical reactions giving rise to different products, differences in the tacticity of the polymer, and nanoscale roughness, which also has the potential to locally distort ζ.

To assess -COOH surface spatial distributions, it was necessary to precisely locate functional groups with nm resolution. Thus, we applied super-resolution microscopy with the -COOH groups labeled with a fluorescent reporter. Based on theoretical predictions, the -COOH surface density may be as high as 0.83 nmol/cm^2 (5 carboxyl groups/nm^2) for a hexagonally ordered surface.[210] Although polymers are not crystalline in nature, we can still expect the density of fluorescent reporters to be far below the resolution limit of conventional fluorescence due to diffraction.[211] Conventional fluorescence experiments are limited to resolutions of ~250 nm along the x-y axis and ~500 nm in the axis depending the wavelength of light used.[211-213] Thus, if the distance between two fluorescent molecules is much greater than the point spread function (PSF) of the fluorescent molecule ($d >> \Delta x$), two well-separated

spots can be observed; however, as d approaches Δx the PSF overlap and a distinction between the fluorophores can no longer be achieved. This is the minimum separation distance at which two fluorophores can be resolved, this the resolution of the microscope is limited by the PSF.[211] Many super-resolution techniques have been developed to overcome this diffraction barrier including: Stimulated Emission and Depletion (STED), Photo-Activated Localization Microscopy (PALM) and Stochastic Optical Reconstruction Microscopy (STORM).

STED overcomes the resolution limit by introducing sub-diffraction-limit features in the excitation pattern so that small length scale information can be read out.[214] STED uses a second laser to suppress the fluorescence emissions from the fluorophores located off the center of the excitation. This suppression is achieved through stimulated emission. This occurs when an excited state fluorophore encounters a photon that matches the energy difference between the excited and ground state, thus, bringing it back to the ground state before spontaneous emission occurs.[214] The sharpening of the PSF of the excitation light, the center of the STED laser must have zero intensity in the center and non-zero intensity on the periphery. The size of the resulting excitation laser is then limited by the practical power level of the STED laser instead of the diffraction of light. This smaller excitation PSF is then scanned across the image and super-resolution images can be obtained. Resolutions as high as ~30 nm have been achieved with this method; however, the higher the resolution, the smaller the pixel size used on scanning and hence the slower the imaging speed.[215]

Another approach to breaking the diffraction barrier is through high precision localization of single fluorophores. This form of super resolution fluorescence microscopy is utilized in techniques such as Photo-Activated Localization Microscopy (PALM) and Stochastic Optical Reconstruction Microscopy (STORM). These methods take advantage of the fact that the precision of determining the centroid of a fluorophore can be much higher than the diffraction limit as long as the image results from multiple photons emitted from the same fluorophore. Fitting an image consisting of N photons can be viewed as

(2.2)

N number of measurements of the fluorophore position thus leading to a localization precision approximate by equation 2.2

$$\Delta_{loc} \approx \frac{\Delta}{\sqrt{N}}$$

Where Δ_{loc} is the localization precision and Δ is the size of the PSF. This scaling of the localization precision with the number of photons allows resolutions not limited by the diffraction of light.[211,214,215] When multiple molecule are present in a diffraction limited area, however, localization becomes impossible due to the overlapping of each fluorophore's PSF. Using fluorescent probes that can switch between a fluorescent and a dark state, overcomes this spatial barrier by separating these fluorescent molecules in the time domain. Molecules within the diffraction limited area can be activated at different time points so that they can be individually imaged and localized. Key to the precision of these approaches is the number of photons that can be captured from one fluorophore, thus several fluorophore classes have emerged with high stability and photon yield. Furthermore, photoswitching properties should include spectral profiles for the active and inactive species that are sufficiently well separated and thermally stable. Ideally these probes should exhibit high switching stability, low fatigue rates and controllable switching kinetics.[212]

PALM achieves single molecule resolution through the use of fluorescent proteins that can be switched to the "on" and "off" states via activation of an additional laser, while STORM utilizes classic fluorescent dyes, such as cyanine dyes, in the presence of a thiol (mercaptoethylamine) that disrupts the molecule's conjugation. Images are collected over several 10s of thousands of frames to ensure the localization of each fluorophore within the diffraction limited area, thus data collection times can be long for these methods; however, these methods report the highest resolution of any super resolution approach. Increasing the time window will result in more localizations, thereby improving the spatial resolution defined by the Nyquist criterion. Conversely, decreasing the time window for each STORM

snapshot will improve the time resolution at the expense of the spatial resolution.[215] Improving the time resolution may be difficult with the currently available fluorescent proteins as the number of photons detected per switching cycle tends to decrease when the excitation laser intensity was increased to accelerate the switching rate. Hence, the camera frame rate used for imaging photoswitchable/photoactivatable fluorescent proteins is typically not higher than 100 Hz, beyond which the image quality deteriorates rapidly. This difficulty can be overcome with bright, fast switching fluorescent dyes, such as Alexa 647, which give a constant number of photons per switching cycle even when the off-switching rate is as fast as ~1 ms. Hence, STORM images using Alexa 647 could be recorded at the camera frame rate of 500–1,000 Hz, and cellular structures have been imaged in two dimensions with a Nyquist resolution of ~20 nm at time resolutions as high as 0.5 s.[215]

Super-resolution microscopes have classically been used for imaging biological samples with a few demonstrations in synthetic samples,[216] nanoparticles,[217] or nanochannel solution ion distributions.[218] We will show in this work the use of STORM microscopy for the analysis of thermoplastic surfaces activated by UV/O_3 or O_2 plasma and the subsequent coupling of a fluorophore to the pendant –COOH functional groups to examine the heterogeneity in the spatial distribution of these functional groups.

2.2 Experimental Section

2.2.1 Reagents and Materials

Poly(methylmethacrylate), PMMA, was purchased from Goodfellow (Berwyn, PA). Cyclic olefin copolymer (COC 8007 and 6017) were purchased from TOPAS Advanced Polymers (Florence, KY). Si <100> wafers were acquired from University Wafers (Boston, MA). Ethylenediamine (EDA), sodium dodecyl sulfate (SDS), dextrose, glucose oxidase (*aspergillus niger*), Dulbecco's phosphate buffered saline (1X DPBS, pH 7.4), catalase (bovine liver), monoethanolamine (MEA, pH 8.0-8.5), sodium bicarbonate buffer (pH 7.5), tripropylene glycol diacrylate (TPGA), trimethylolpropane triacrylate (TMPA), Irgacure

651 (photo-initiator), and potassium chloride (KCl) were purchased from Sigma-Aldrich (St. Louis, MO) and used as received. Alexa Fluor® 647 NHS ester and 20 nm Nile red (535/575) carboxylate modified polystyrene spheres were secured from Life Technologies (Grand Island, NY). Anti-adhesion (tridecafluoro – 1,1,2,2 – tetrahydrooctyl) tricholorosilane (T-Silane) was purchased from Gelest, Inc. (Morrisville, PA). Tris buffer (pH 8.0) was obtained from Fisher Scientific (Houston, TX). All dilutions were performed using 18 MΩ/cm milliQ water (EMD Millipore, Billerica, MA), with all measurements carried out at 25°C.

2.2.2 Surface Activation and Modification

The protocol used for activating and modifying surfaces has previously been reported and validated.[199] In brief, PMMA and COC (1 cm^2) were sonicated for 30 min in 0.1% SDS and then exposed to either UV/O_3 (31.1 mW/cm^2, λ = 254 nm) or O_2 plasma (50 W, 10 sccm) for various times to generate surface carboxyl groups with different densities. Covalent attachment of Alexa Fluor® 647 NHS Ester to the surface confined -COOH groups was achieved by first generating an amine-terminated surface by incubation of the activated plastic in a solution containing 100 mg EDC and an excess of EDA (134 µL) in 2 mL 0.1 M MES buffer (pH 4.8) for 20 min.[199] The plastic was then removed from this solution, washed thoroughly with DI water, spotted (2 µL) with Alexa Fluor® 647 NHS in 0.1 M sodium bicarbonate (pH 7.5), and incubated in the dark for 1 h. The samples were then thoroughly washed with DI water.

2.2.3 STORM Imaging

All imaging was performed on activated COC or PMMA thin films (100 µm) with the surface confined -COOH groups labeled with the fluorescent reporter. For STORM, the underlying mechanism for photoswitching between 'on' and 'off' states required the addition of a thiol containing molecule. For this reason, the buffer used for imaging was composed of 80% (v/v) 1X DPBS (pH 7.4), 10% (v/v) 1M MEA, 10% (v/v) 50% glucose and 1% (v/v) glucose oxidase/catalase oxygen scavenger. Imaging was performed using a Zeiss Axio Observer Z-1invertro microscope with a 100x oil immersion objective (NA

1.46), an iXON EMCCD camera, and 405, 488, 561 and 640 nm wavelength lasers. For the purposes of these experiments, only the 405 nm and 650 nm laser were used. The laser power was precisely selected to balance photoswitching kinetics and photobleaching. To obtain the best resolution, one must optimize the number of photoswitching cycles as well as the time spent in the 'on' or 'off' state. In order to ensure that two dye molecules were not emitting at the same time within a diffraction limited area, the 'off' time should be much greater than the 'on' time. This was considered in our laser power selection.[219,220] The image pixel size was 10 nm with a camera pixel size of 16 µm. Exposure times were 30 ms to ensure that single fluorescent events were captured with high signal to noise.

Each sample was imaged for 5 min (>10,000 frames). Within this collection time, fluorophores cycle through several 'on' and 'off' states. Image frames capturing the blinking of surface confined fluorophores were then analyzed using Carl Zeiss Zen image processing software adopting the classical super-resolution image processing protocol. In brief, the Zen software performed a peak finding function in all frames based on minimum and maximum photon count thresholds to ensure that both noise and aggregated non-blinking molecules were excluded. Next, peak fitting algorithms were applied to determine the width and centroid position of each peak. Once all localizations were determined, drift correction and peak grouping functions were applied. One 'on' event for a fluorophore can last for several frames with the collection time employed herein.

During the acquisition time, the molecule may appear to drift due to thermal expansion and mechanical vibration. The algorithm used for drift correction breaks the rendered STORM image into smaller, lower quality STORM images. Then, cross-correlation of subsequent images allowed a measurement of sample drift. This method is well documented and widely used.[213,221] Furthermore, because a molecule may appear in several frames, several parameters were used to group these localizations to one molecule. These include maximum "on" time, defined as the maximum number of frames that peaks are allowed to be detected in order to be considered one molecule (5 frames),

maximum off time, defined as the maximum number of frames that a peak can be missing and still considered one molecule (10 frames) as well as capture radius, defined as the pixels within which peaks of consecutive frames must lie in order to be considered as belonging to the same molecule (2 pixels). Lastly, for accurate positioning, if the PSF of two different localizations overlapped and appeared as one distorted spot, these events were discarded. Further parameters such as photon count, point spread function diameter, and localization precision were used to render STORM images, as is classically done in super-resolution post processing. Conventional fluorescence images were collected using the same microscope without reconstruction post-processing.

Control experiments were performed to determine non-specific dye adsorption. Activated surfaces were incubated with just Alexa Fluor® 647 NHS without the amine linker. Control experiments showed <1% non-specific adsorption based on the total number of localizations.

2.2.4 COMSOL Simulations

Fluorophore centroids that were determined from the super-resolution images were mapped as single point charges on otherwise non-charged surfaces of a 50 nm × 50 nm × 1 µm (W × H × L) model nanochannel to approximate the effect of heterogeneous surface charges on the EOF. Geometries were constructed via a MATLAB code and imported into COMSOL Multiphysics (v 5.0) was used to solve for EOF profiles with a two ion buffer system (see modeling for modelling parameters). Notably, oxygen-containing functional groups other than -COOH groups, which were likely generated during activation, were not included in the model due to their unknown densities and positions. However, because these groups would be expected to be uncharged for the pH values used herein, they would not be expected to contribute to the EOF.

Parameter	Uniform Channel	5 min UV/O_3
Diffusivity of Hydrogen	9.31×10^{-9} m^2/s	
Diffusivity of Chlorine	2.03×10^{-9} m^2/s	
Mobility of Hydrogen	3.76×10^{-12} s*mol/kg	
Mobility of Chlorine	8.19×10^{-13} s*mol/kg	
Initial Concentration of Hydrogen	2×10^{-3} M	
Electric Field	50 V/cm	
Debye Length	$6.87 \times 10 \times 10^{-9}$ m	
Initial Concentration of Chlorine	2×10^{-3} M	
Channel Dimensions	50 x 50 x 500 nm	50 x 50 x 1000 nm
Surface Charge Density	-1.2×10^{-3} C/m^2	-1×10^{-12} C/m^2
-COOH Point Charge	-	-1.27 C/m^2

Table 2-1 COMSOL parameters used for fluid modeling

2.2.5 Nanoslit Fabrication

The fabrication of nanoslits in thermoplastics is detailed elsewhere.[53,77] Briefly, a silicon master was fabricated by initially patterning two access microfluidic channels (55 µm wide, 12 µm deep, 1.5 cm long) into a Si <100> wafer using standard photolithography followed by anisotropic etching with 45% KOH. Next, 3 µm x 150 nm nanofluidic slits were patterned by FIB milling of the Si wafer using a Helios NanoLab 600 Dual Beam instrument (FEI, Hillsboro, OR).

An anti-adhesion coating of T-Silane was applied to the Si master from the gas phase in a desiccator under vacuum for 2 h to facilitate demolding. A resin stamp was then made using UV-NIL from a UV-curable polymeric blend containing 68 wt% TPGA as the base, 28 wt% TMPA as the crosslinking agent and 4 wt% Irgacure 651 as the photo-initiator that was coated onto a rigid COC back plate. The stamp was cured by exposure to 365 nm light (10 J/m^2) through the COC back plate for 7 min in a CL-100 Ultraviolet Crosslinker (UVP, LLC, Upland, CA). The UV-cured resin was gently demolded from the Si master.

The stamp was imprinted into a 1.5 mm thick piece of COC by NIL with access holes used as reservoirs. NIL was performed at a pressure of 2888 kN/m^2 for 120 s with the top and bottom plates maintained at a temperature of 95ºC using a Hex03 thermal imprinter (JenOptik AG, Jena, Germany).

Pressure was applied after 30 s and was maintained during imprinting until the system was cooled to 45°C. A 100 µm thick COC sheet of the same type as the substrate was used as the cover plate. Both the COC substrate and cover plate were pre-activated with oxygen plasma. Thermal assembly was performed immediately at 70°C for 900 s using 977 kN/m^2 pressure.

2.2.6 Nanoelectrophoresis of Fluorescent Nanoparticles

All fluorescence imaging for the nanoelectrophoresis were performed using an Axiovert 35 inverted microscope (Carl Zeiss AG, Oberkochen, Germany) equipped with a 100× oil immersion objective (NA 1.3). For imaging, the optical system in Figure 2–1 was used. A Gaussian laser beam (Nd: VYAG; λ_{ex} = 532 nm; P = 0.01-5 W; 2.2 mm beam diameter) was expanded with a 10X Keplerian beam expander to completely back-fill the objective and the wings were knocked out with an iris to ensure uniform laser intensity in the field-of-view. The beam was focused using a lens into the back of a microscope objective to allow irradiation of the entire field of view and passed through a 532 nm laser line filter and dichroic filter. The emission signal was collected by the objective, passed through a dichroic filter, was spectrally selected using longpass and bandpass filters, and was imaged onto an iXon3 897 EMCCD camera (Andor Technology Ltd., Belfast, United Kingdom) controlled by Metamorph software. Trackmate software in Fiji was used for data analysis.

All electrophoresis experiments were conducted in 1× PBS (pH 7.4). A 1.0 fM concentration of polystyrene microspheres was used to increase the likelihood of single particle occupancy within the nanoslit. Polymer nanoslits were primed with buffer and allowed to equilibrate prior to the electrophoresis. The fluorescent nanospheres were loaded into an injection reservoir and various field strengths were applied (100-300 V/cm) to electrokinetically drive the spheres into the nanoslits. Translocation events were captured and processed using the optical system described above.

2.3 Results and Discussion

2.3.1 STORM versus Conventional Fluorescence

Typically, STORM is used to interrogate biological features with sub-diffraction limit resolution.[211] STORM accomplishes sub-diffraction imaging by sequential activation and time-resolved localization of photoswitchable fluorophores. In STORM imaging, fluorophores were heavily biased towards the "off" state by the inclusion of a thiol (mercaptoethylamine) that disrupts the molecule's conjugation, but when

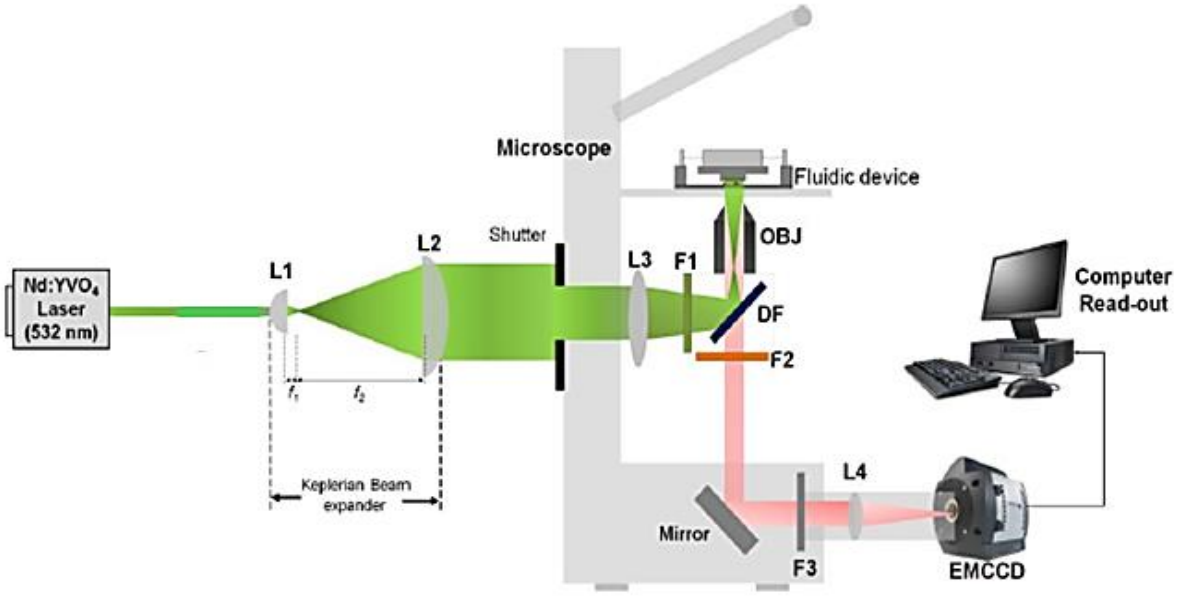

Figure 2–1 Optical set-up of the fluorescence imaging system. The Gaussian beam from the Laser (Nd: VYAG (λex = 532 nm; P = 0.01-5 W; 2.2 mm beam diameter) was expanded 10 times with a Keplerian beam expander (focal lengths were 20 mm and 200 mm for L1 and L2 plano-convex lenses, respectively) and the wings were knocked out with a beam iris that ensured uniform laser intensity in the field-of-view and complete back-filling of the objective (OBJ). The beam was focused through an iris into the back of a 100x oil immersion objective lens (OBJ) using lens (L3) after passing through a 532 nm laser line filter (F1) and being reflected by a dichroic filter (DF). A collimated laser beam impinged upon the polymer nanofluidic device. The fluorescence signal generated from the single fluorescent entities were collected by this same objective, passed through the DF and spectrally selected using a long pass filter (F2). A mirror was used to steer the fluorescence signal onto the EMCCD after passing through a band-pass filter (F3) and focused using a lens (L4).

the fluorophore was exposed to UV light, the thiol was dissociated, conjugation was regenerated, and the molecule can reach the "on" state to generate fluorescence. By suppressing the probability of fluorescence, the centroids of individual fluorescent events can be precisely located with ~20 nm resolution, and the entire surface can be reconstructed by imaging for several minutes and merging the events that are observed throughout the tens of thousands of frames.

For our experiments, we sought to use STORM to probe thermoplastic surfaces that were exposed to UV/O_3 irradiation or O_2 plasma, which can generate surface-confined -COOH groups[178] that are useful for generating EOF as well as immobilizing moieties such as small molecules[199] and/or biomacromolecules.[57] To visualize the surface confined -COOH groups by STORM, we conjugated these groups to a short diamine cross-linker and subsequently labeled the free primary amine with an NHS-ester fluorescent dye, allowing us to monitor the spatial distributions of the dye-labeled -COOH groups. We then captured >10,000 frames as these surface confined fluorophores transitioned between 'on' and 'off' states. There frames were then imported into commercial image processing software and precise parameters were used to localize each fluorophore and render highly resolved STORM images. **Error! R eference source not found.** compares STORM (a) and conventional fluorescence microscopy (b) imaging of 26 μm^2 areas of UV/O_3 treated COC. Specifically, we are imaging dye-labeled, surface-confined -COOH groups generated through UV/O_3 activation. Also shown are line plots of a 1 μm^2 subsection of these images. The conventional fluorescence image had several overlapping spots of various intensities, indicating that densely packed fluorophores could not be resolved (**Error! Reference source not f ound.**d). The benefits of STORM imaging were immediately apparent with the centroid of each fluorophore resolved, even at the higher dose levels where the functional group spacing is low. For example, in the 1 μm^2 subset images of **Error! Reference source not found.** a and **Error! Reference so urce not found.** c, the centroids of 41 different fluorescent events were localized by STORM while an unknown number of fluorophores contributed to the conventional fluorescence image.

However, not all 41 events in **Error! Reference source not found.** a necessarily originated from d ifferent dye molecules. Each fluorescent molecule can cycle through on/off states multiple times throughout the 5 min imaging time; the dye's position can shift slightly between cycles. It is unlikely that movement of the dye molecule relative to the surface would be significant because the diamine linker was only ~1 nm in length, thereby constraining the molecule's movement. Rather, shifts in the fluorophore's image can be attributed to drift of the microscope due to thermal expansion and/or mechanical vibrations. Furthermore, random errors of the fitting procedure, localization accuracy and systematic errors of the microscope can also contribute to the inaccurate localization of molecules.

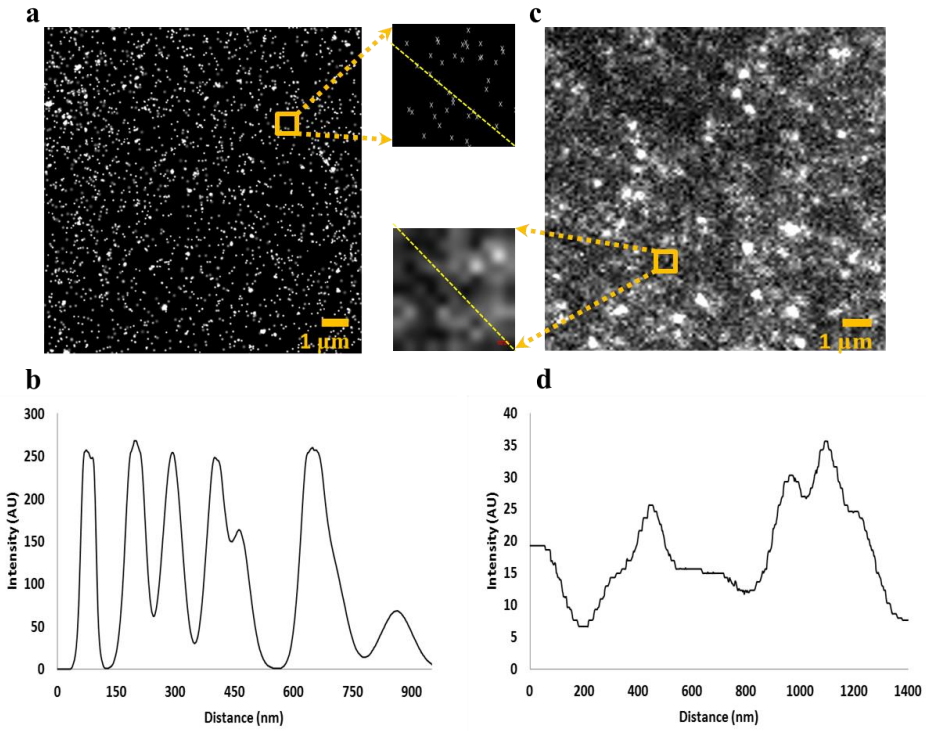

Figure 2–2 (a) STORM image of COC exposed to 1 min UV/O3 radiation (31.1 mW/cm2 λ=254nm) with 1 µm2 in-set, and (b) line plot from top left to bottom right of (a) inset. (c) Conventional microscopy image of COC exposed to the same UV/O3 dosage also with accompanying 1 μm^2 inset, and (d) line plot from dashed line in (c) inset.

To determine the average number of blinking events for a given fluorophore, we examined individual localizations of the STORM images by hierarchal clustering analysis.[222] By fitting the number of clustered blinking events to an exponential distribution (Figure 2–3), we determined a Poisson average of 7 blinks per fluorophore. These results were reproducible across various activated polymers (data not shown). Secondly, the spatial distribution of the clustered blinking events was fit with a Gaussian function (Figure 2–4); each molecule's distribution of localization was characterized by a full width at half maximum of ~40 nm. Two events can be resolved if they are separated by greater than the FWHM. We observed a localization accuracy (i.e. σ of the Gaussian function) of 17 nm. The localization accuracy was determined after all STORM post-processing procedures, including drift correction, thus this value represents the localization accuracy and drift efficiency. Since the experimentally measured localization accuracy is in agreement with the theoretical precision (σ= 20 nm, calculated from the photon count of 800-1000), the efficiency of drift correction was quite high and had little contribution to the overall error in localizations. Nevertheless, STORM enabled the localization of dye-labeled -COOH groups separated by >40 nm, which was not possible using conventional fluorescence microscopy.

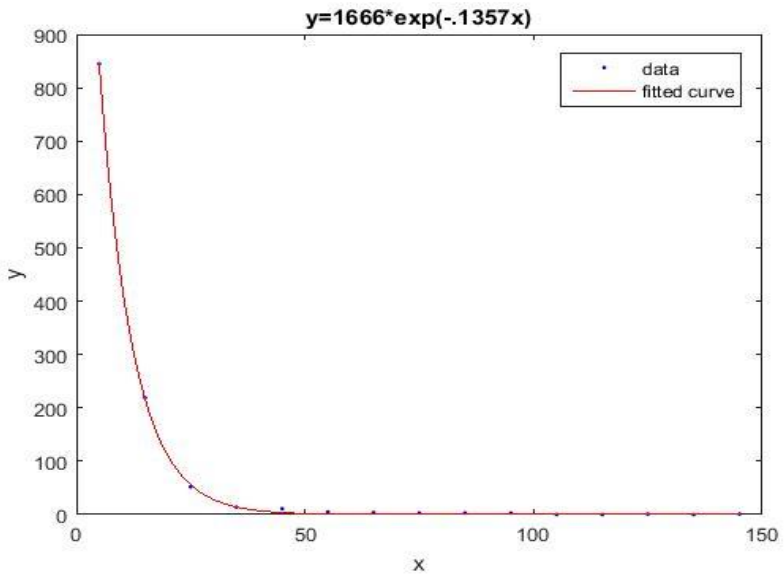

Figure 2–3 MATLAB exponential fitting of the number of blinking events versus counts. Equation of this line was y=1666*exp-.1357x which shows an average number of blinking events to be 7.

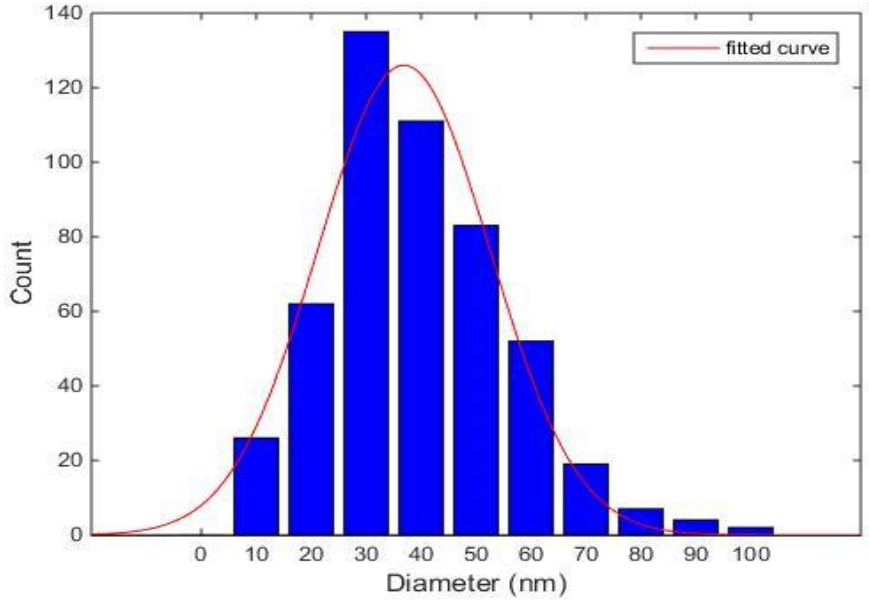

Figure 2–4 Figure S3. Representative Gaussian fit of clustered STORM data to determine the FWHM.

2.3.2 Comparing Relative COOH Density using STORM

STORM imaging was used to investigate the relative changes in the density of dye-labeled -COOH groups on COC and PMMA surfaces that received various doses of UV/O_3 irradiation or O_2 plasma exposure. Representative images, where the centroids of blinking events were plotted, are shown in Figure 2–5 -e for COC and Figure 2–5 f-j for PMMA exposed to UV/O_3 irradiation for different times. While the absolute density of fluorophores could not be assessed due to multiple blinking events per fluorophore, relative changes in the surface density of dye-labeled -COOH groups could be deduced because the experimental conditions (buffer composition, light intensity, *etc.*) were the same throughout all STORM imaging. Thus, the dependence of -COOH surface density due to polymer, activation method and exposure time could be discerned as shown in Figure 2–5 k,l.

There was an increase in -COOH relative density on COC surfaces as UV/O_3 exposure increased up to 15 min. After 20 min exposure, there was a dramatic decrease in the relative -COOH surface density (Figure 2–5 k, solid square). A similar trend was observed for COC exposed to O_2 plasma with an

increase observed up to 10 s exposure times and a drop in the relative density after 30 s exposures (Figure 2–5 l, solid square). The apparent decrease in -COOH density for long exposure times for both UV/O_3 and O_2 plasma activation is most likely due to radical reactions occurring after -COOH generation, which can degrade the -COOH group and lead to effects such as –CO_2 release, scissioning of the polymer chain, and etching of the surface.[200,223] Chemical groups other than –COOH generated by these activation processes are not probed by our fluorescent reporter, which was specific for -COOH groups; however, the authors note that previous research has shown that –COOH functional groups are the dominate species following UV/O_3 or plasma activation protocols performed on PMMA and COC thermoplastics.[57]

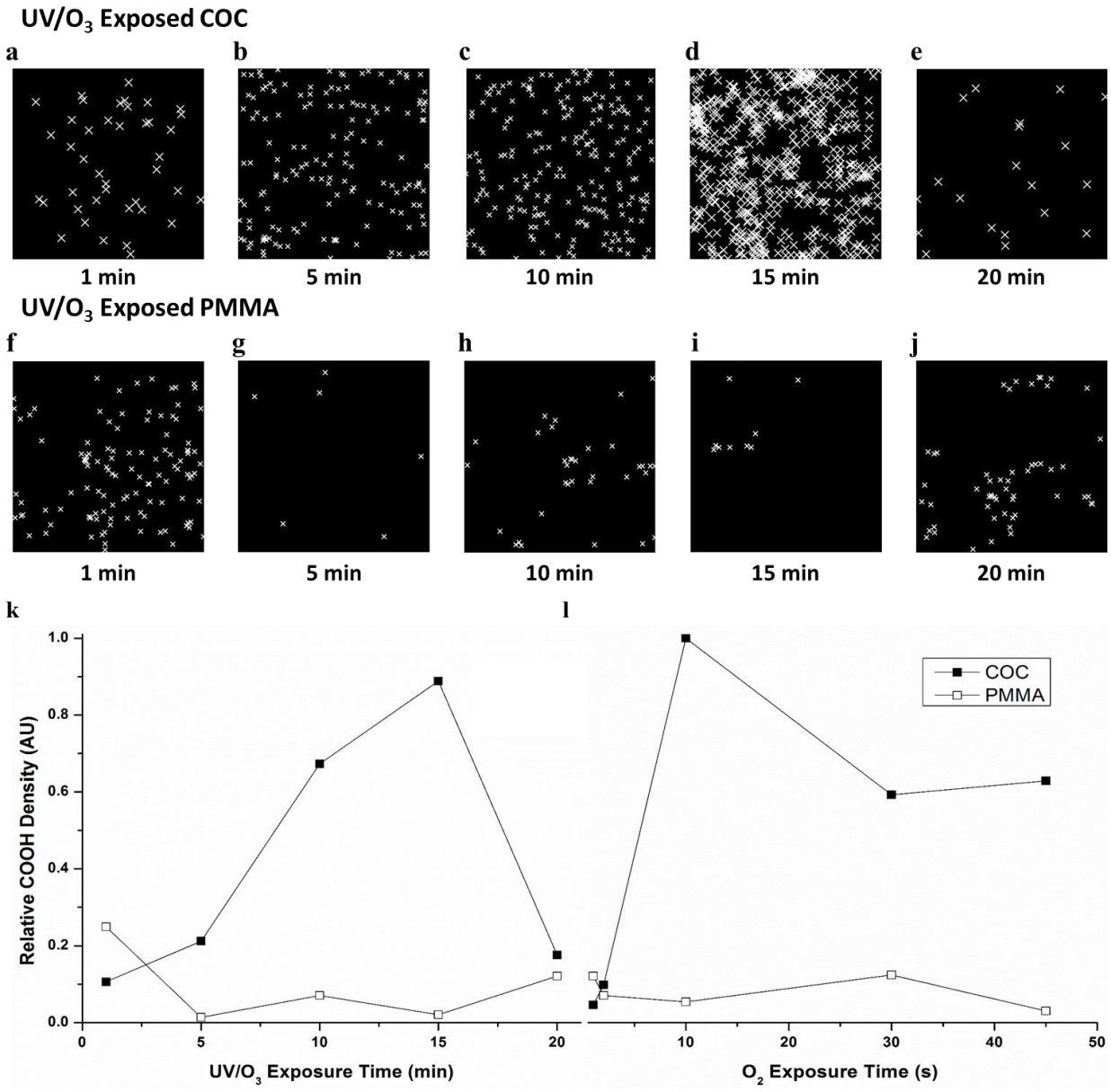

Figure 2–5 Representative STORM images of 1 µm2 (a-e) COC and (f-j) PMMA exposed to 1, 5, 10, 15, and 20 min UV/O3 radiation, respectively. Relative -COOH density versus exposure time for (k) UV/O3 and (l) O2 plasma modified COC (closed squares) and PMMA (open squares). Lines are for visual purposes only. UV/O3 and O2 plasma exposure conditions were kept constant (see text for details). All total localizations were normalized to the greatest localization density, COC exposed to 10 s of O2 plasma.

The density of -COOH functionalities on UV/O_3 activated PMMA surfaces (Figure 2–5 k, open square) was greatest for 1 min exposure with a decrease for longer exposure times until ~20 min, when it was observed that the –COOH relative density slightly increased. A similar trend was seen for O_2 plasma exposed PMMA (l, open square); the greatest -COOH relative densities were observed at 1 s exposure, and the -COOH relative surface density decreased from 2 to 10 s exposure, returned to a relatively high level after 30 s, and then decreased again after 45 s exposure. Two factors contributed to these results. First, -COOH generation is known to be more efficient on COC surfaces compared to PMMA, although –COOH formation dominates for both thermoplastics.[57] Scissioning of PMMA polymer chains throughout UV/O_3 exposure has been suggested to compete with -COOH formation and lead to extensive fragmentation and etching of the polymer, more so than for COC polymers.[57] This provides an explanation for the relatively lower surface densities overall. Secondly, the PMMA contained impact modifiers, cross-linked poly(butylacrylate)[57], which may have a poorer propensity to undergo photooxidation to generate pendant -COOH groups. These impact modifiers can be observed by O_2 plasma exposure in Figure 2–6, which showed surface roughness features on PMMA due to the differences in plasma etch rates between PMMA and poly(butylacrylate).

Overall, two observations can be made from this data: (i) The maximum -COOH relative densities on PMMA substrates were achieved at the shortest activation times, 1 min UV/O_3 and 1 s O_2 plasma treatment. In the case of COC, longer exposure times were required to maximize the relative surface density of the -COOH groups. (ii) The greatest relative density of -COOH groups generated on PMMA by UV/O_3 and O_2 plasma were 25% and 10%, respectively, compared to the densities observed on similarly treated COC substrates.

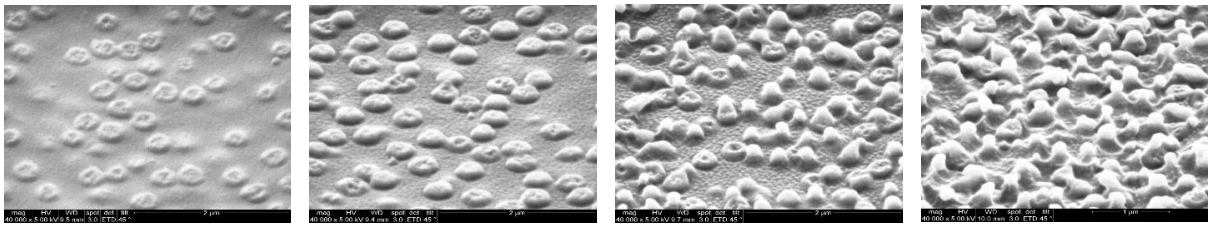

Figure 2–6 SEM Images of PMMA exposed to varying doses of O2 plasma showing the presence of impact modifier (butylacrylate) additives.

With our current localization accuracy of 17 nm and considering the maximum hexagonal packing density of fluorophores, the highest density that could be theoretically localized would be 4 x 10^{11} molecules/cm^2, which is insufficient for a crystalline structure (~1 x 10^{14} molecules/cm^2). However, the maximum number of localization density we encountered was ~5 x 10^{10} molecules/cm^2. Thus, we have not reached the upper spatial resolution detection limit of our current STORM conditions.

2.3.3 Determination of Functional Group Heterogeneity using STORM

The heterogeneous spatial distribution of -COOH groups can have a significant impact in applications such as nanoscale electrophoresis by creating recirculation in the flow field and thus, lowering the efficiency in the separation. The sub-diffraction limit resolution afforded by STORM enabled us to observe these spatial distributions with accuracy not possible by traditional fluorescence microscopy. To determine the heterogeneity in the spatial distribution of -COOH groups on the polymer surface with nm-resolution, the Euclidian distance between each localization determined through STORM was calculated; however, the Euclidean nearest-neighbor distance was confounded by blinking of the fluorophores in time. A given fluorophore will be detected multiple times, shifting slightly in position due to instrument drift and generating nearest-neighbor distances that do not sometimes reflect the true spatial distribution of dye-labeled -COOH groups. Thus, for each fluorescent event we excluded nearest-neighbors within the localization accuracy (17 nm) and assembled the distributions of nearest-neighbor distances for both thermoplastics under all activation conditions (Figure 2–7).

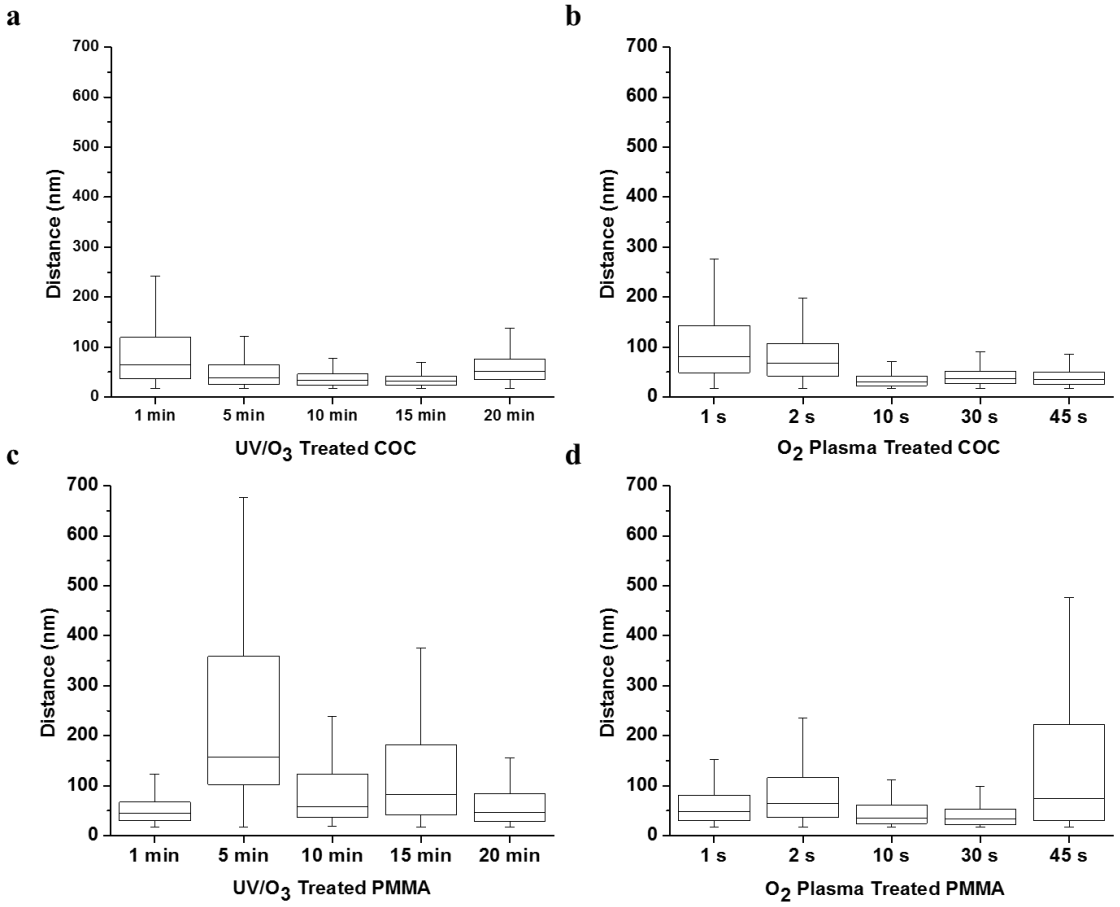

Figure 2–7 Distance between fluorophores in 1 μm^2 subset images (see Figure 2) for (a) UV/O3 modified COC; (b) O2 plasma modified COC; (c) UV/O3 modified PMMA; and (d) O2 plasma modified PMMA. Error bars represent range; upper and lower edges of the boxes indicate the third and first quartiles, respectively, and the mid-line shows the median.

In general, irrespective of the polymer or activation source, increasing -COOH surface relative densities correlated, not surprisingly, with a decreased distance between functional groups. For example, at low doses of UV/O_3 activation, the average nearest-neighbor distance between -COOH groups on COC was large with a median distance of 64 nm after 1 min exposure that decreased to 31 nm after 15 min exposure. The reduced spacing was mirrored by the increase in -COOH relative densities (Figure 2–5 k) and a similar trend was observed for COC surfaces throughout the different O_2 plasma exposure times. Not only did the median functional group distances decrease, but the variance in the distributions

reduced as well. This was evident as the first and third quartiles approached the median spacing after 15 min UV/O_3 exposure as well as a 4-fold decrease in the first and third quartile range from 1 min exposure to 15 min exposure.

Activated PMMA surfaces showed a broader spatial distribution of dye-labeled -COOH groups, although at short exposure times (1 min UV/O_3 treatment and 1 s O_2 plasma activation), the distributions were much narrower than the highly heterogeneous surfaces observed at longer activation conditions. For a PMMA surface activated by 1 min UV/O_3 and 30 s O_2 plasma exposures, the lowest median nearest-neighbor distances were 45 nm and 34 nm, respectively, and the distributions between the first and third quartiles ranged from 30-67 nm and 24-64 nm, respectively.

We note that in this analysis, we only approximated spatial distributions using the nearest-neighbor distance between dye-labeled -COOH groups that was greater than the 17 nm localization accuracy. At high -COOH densities, there appeared to be “patches” of polymer that were unmodified and these effects are not described by the nearest-neighbor analysis. This is especially apparent for COC, that was activated by 15 min UV/O_3 irradiation (Figure 2–5), where the unmodified patches were 100 × 100 nm in size. For PMMA, this may be attributed to the impact modifiers contained within the films (Figure 2–6). However, COC substrates are not known to contain such additives and we do not have sufficient data to source the origin of these unmodified patches.

2.3.4 COMSOL Simulations of EOF Flow with Non-uniform Surface Charge

In glass-based micro- and nanofluidic devices, the homogeneous surface distribution of silanol groups are known to generate uniform and stable EOF profiles.[105] It is also known that the relatively low density of -COOH groups on activated thermoplastic surfaces reduces the EOF magnitude compared to glass.[199] Here, we investigated if the spatial heterogeneity of the charged functional groups on the thermoplastic distort the uniformity of the EOF flow profile.

To this end, we first conducted three-dimensional computational fluid dynamics simulations of

the EOF. The locations of -COOH groups on COC surfaces activated by 5 min of UV/O_3 exposure, which were obtained via STORM imaging, were mapped directly onto the surfaces of a 50 × 50 × 500 nm (w × h × l) nanochannel. Each -COOH group was assigned as a point and given the charge of a single electron, and the EOF profiles generated by these point charges were simulated using a two ion buffer system. Polar functional groups, such as alcohols and other carbonyl-containing moieties, are also known to be generated by either UV/O_3 or O_2 plasma exposure on many thermoplastics; however, to a lesser extent than -COOH.[57] We note that while these non-carboxylate functional groups could be generated using UV/O3 or O2 plasma activation, such as alcohols, aldehydes and/or ketones, these groups would be uncharged at the pH values used in these experiments. Thus, their contribution to the EOF would not be present and would be determined only by the surface -COOH groups that we are monitoring. However, the reactions generating these non-charged functional groups can contribute to the observed –COOH surface heterogeneity.

As a reference, a nanochannel was modeled using a uniform charge density to mimic a silanol-based fused silica nanochannel Figure 2–8 a). One can observe a drop in the applied potential along the nanochannel's length as well as the charged wall's strong negative potential extending into the ionic solution. The resultant EOF profile approached a maximum longitudinal velocity of 40 μm/s in the

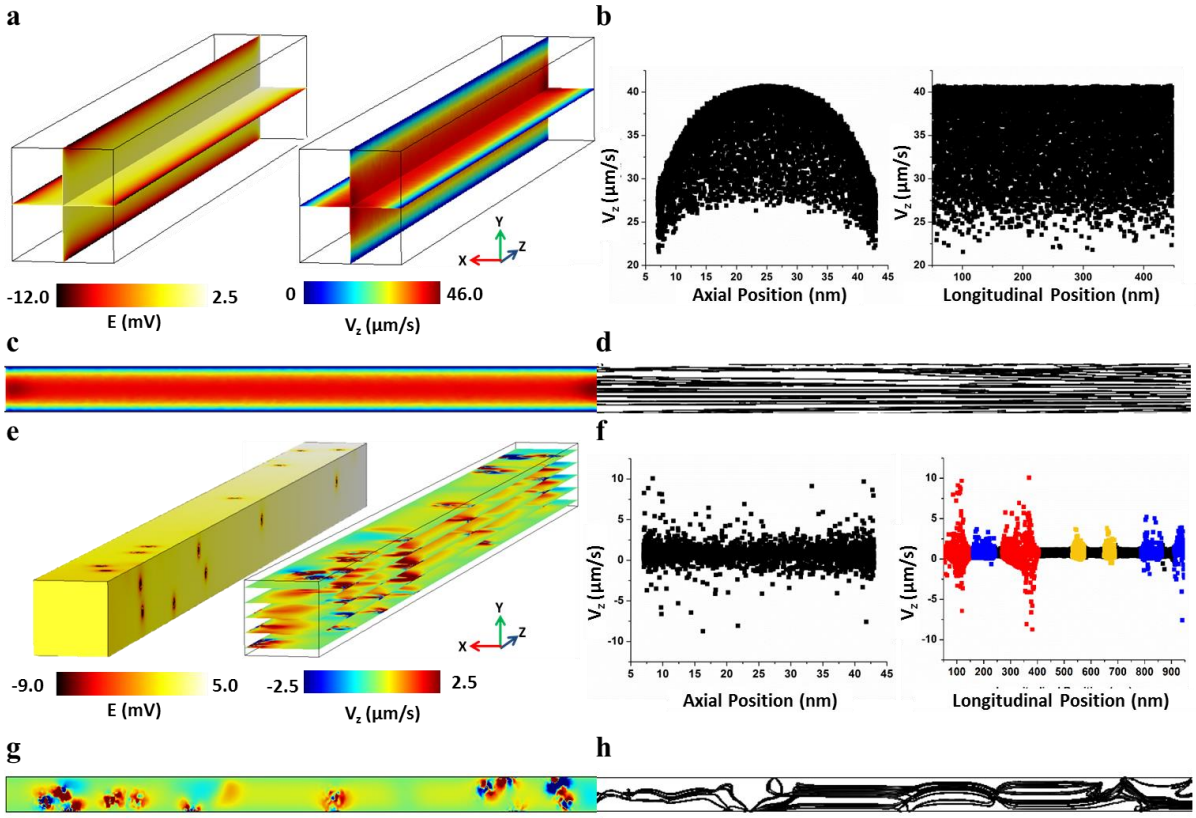

Figure 2–8 (a) COMSOL simulation showing the electric potential (left) and velocity magnitude (right) for a channel with uniform surface charge (b) Velocity vs. Axial (right) and Longitudinal (left) position to show the EOF flow profile for a channel with uniform surface charge (c) One slice of the velocity magnitude of a uniform channel (d) Streamline of the same velocity slice depicted in (c) (e) COMSOL simulation showing the electric potential (left) and velocity magnitude (right) where single point charges are mapped onto the nanochannel surfaces using the –COOH locations (centroids) obtained by STORM analysis of a COC surface exposed to 5 min UV/O3 activation. (f) Velocity vs. Axial (right) and Longitudinal (left) position to show the EOF flow profile for the channel with non-uniform surface charge. The colors in the velocity vs. Z position graph (right) represent an area in the channel with >5 (red), 3-4 (blue) and 1-2(yellow) COOH group(s) within 20 nm of each other (g) One slice of the velocity profile to show fluid flow recirculation (h) Streamline of the same velocity slice depicted in (e) to emphasize the fluid re-circulation at areas with -COOH.

channel's center, but as the 6.9 nm Debye length was close to the nanochannel's physical dimensions, the no-slip condition generated a parabolic flow profile (Figure 2–8b, left panel). Indeed, we are operating in a region with a κa^4 value of 3.7, confirming some EDL overlap. Despite EOF non-uniformity along the axial dimension producing Taylor dispersion, the EOF is highly uniform along the channel's length (Figure 2–8b, right panel and (Figure 2–8c). This is beneficial for electrophoretic separations as

the resulting velocity streamlines are highly reproducible (Figure 8d) and uniform (*i.e.*, no recirculation). Unlike the fused silica nanochannel simulation, the UV/O_3 activated thermoplastic nanochannel generated an irregular EOF profile. The positions of the negative point charges mapped from the STORM image can be seen in the electric potential plot in Figure 2–8e. Near these point charges, the longitudinal velocity profile is highly distorted, being positive within a Debye length of the point charge but also negative elsewhere, which is a strong indication of flow recirculation (Figure 2–8 e,g). Because the -COOH distribution were heterogeneous along the channel's longitudinal axis, there was a distorted velocity pattern along the channel's longitudinal dimension (Figure 2–8f, left panel). The EOF's longitudinal velocity could be correlated to the position of the deprotonated -COOH groups along the channel's length (Figure 2–8f, right panel). Near each point charge, there are both positive and negative velocities, which scale in magnitude with the number of -COOH groups in proximity. The highest local velocities were 3, 7, and 10 μm/s in the regions with 1-2 (yellow), 3-4 (blue) and >5 (red) surface charges in close proximity. These phenomena were evident in the velocity streamline trace (Figure 2–8h), which indicated the trajectories' of non-charged particles in the absence of diffusion. Also, in regions with no -COOH groups, there was a small (2 μm/s) forward velocity due to bulk flow of the buffer.

In summary, the fused silica-based simulation with uniform surface charge generated a non-distorted EOF profile throughout the device, although the flow was parabolic due to EDL overlap. Such parabolic flow can induce Taylor dispersion into an electrophoretic separation, but can offer unique electrophoretic separations not possible without this EDL overlap, such as the free solution separation of double-stranded DNAs.[27] The COC nanochannel, which had non-uniform surface charges that were mapped directly from the STORM images indicated a distorted EOF. However, even regions with relatively high localized EOF would not likely provide a noticeable effect on zonal dispersion resulting from recirculation because the particle's electrophoretic mobility would likely dominate due to the small EOF observed due to the sparsely charged nature of the polymer channel walls.

This provides a unique opportunity for thermoplastic devices because of the ability to selectively and locally activate portions of a nanochannel by exposing to either O_2 plasma or UV/O_3 through a mask without creating global EOF. Also, by selecting the appropriate activating dose, the surface charge density can be controlled, which allows for control of the magnitude of the EOF without requiring surface passivation.

2.3.5 Nanoscale Electrophoresis

To empirically observe the potential effects of EOF distortion arising from a non-uniform distribution of -COOH groups on the nanocolumns' wall, we performed single particle, nano-scale electrophoresis and simultaneously tracked the motion of a single fluorescent polystyrene nanoparticle (20 nm in diameter). A separate fluorescence microscope than the one used for STORM was operated in an epilumination format with a wide field-of-view and uniform laser excitation intensity profile across this field-of-view (see Figure 2–1), which enabled the precise tracking of individual nanoparticles through a nanoslit that was 3 µm wide and 150 nm deep fabricated in COC.[77] The COC nanoslits were activated by 30 s of O_2 plasma exposure then assembled with a thin COC cover plate thermally fusion bonded to the substrate. A nanoslit was chosen in place of a nanochannel here because nanoparticle movements within a 50 nm square nanochannel would occur below the diffraction limit and would require a rapid imaging super-resolution system for tracking the transport process. Similar phenomena, namely fluid recirculation, were expected in the nanoslit and also, the nanoslit's width (3 µm) enabled the detection of axial perturbations in nanoparticle motion that could be followed above the diffraction limit using a high framerate epilumination microscope (Figure 2–1).

Figure 2–9 a shows the distribution of travel times of the fluorescent nanoparticles in the COC nanoslit at two different electric field strengths. The migration of the negatively charged polystyrene nanoparticles was from cathode to anode (*i.e.,* the nanoparticles' electrophoretic mobility was greater than the EOF of the COC). This was anticipated based on the low EOF observed in thermoplastic

devices[199] as well as results from the fluid dynamics simulations (see Figure 2–8) that showed a small EOF due to the low surface charge density produced at the O_2 plasma dosing conditions employed here (see Figure 2–5 l). At 200 V/cm, the average migration time of the particles through the field-of-view (100 µm) was 1.2 ±0.5 s, while the average migration time at 300 V/cm was 0.20 ± 0.02 s. Thus, a 50% increase in field strength generated a 600% decrease in the electrophoretic migration time. Further, the relative standard deviation of migration times was reduced from 40% at 200 V/cm to 8% at 300 V/cm, a 5-fold decrease (Figure 2–9a). We do note that some variance in migration times could be due to the differences in the sizes of the particles; however, this contribution to the overall standard deviation shown in the distribution of migration times for both applied fields would be the same. The relatively high variance noted at the lower electric field strength is most likely due to stick/slip motion. Sticking motions are typically seen at low electric fields, while slip dominates the motion at high electric fields.[199] Stick/slip motion can be due to either solute/wall interactions or dielectrophoretic trapping induced by inhomogeneous electric fields caused by surface roughness. Thus, the zonal variance at 300 V/cm would be less due not only to reductions in the variance arising from longitudinal diffusion, but also reductions in stick/slip motion at the higher electric field.

We did observe transverse motion of the nanoparticles at 200 V/cm and some evidence of recirculation, while the application of 300 V/cm removed these artifacts (Figure 2–9b,c). While both the electrophoretic mobility and EOF should be directly proportional to the electric field strength, we suspect that stick/slip motion provided a non-linear field dependence on the particles mobility, which we noted for the mobility of double-stranded DNA molecules migrating through polymer nanochannels.[199] As these tracking dynamics are currently restricted to nanoslits due to diffraction limits, nanochannel columns (*e.g.*, a 50 × 50 nm nanochannel) may show more particle-wall interactions and increased stick/slip motion. However, even higher electric fields could be used to mitigate stick/slip motion for nanocolumns while avoiding significant Joule heating and zonal dispersion that would classically be

observed in microscale capillary electrophoresis columns.

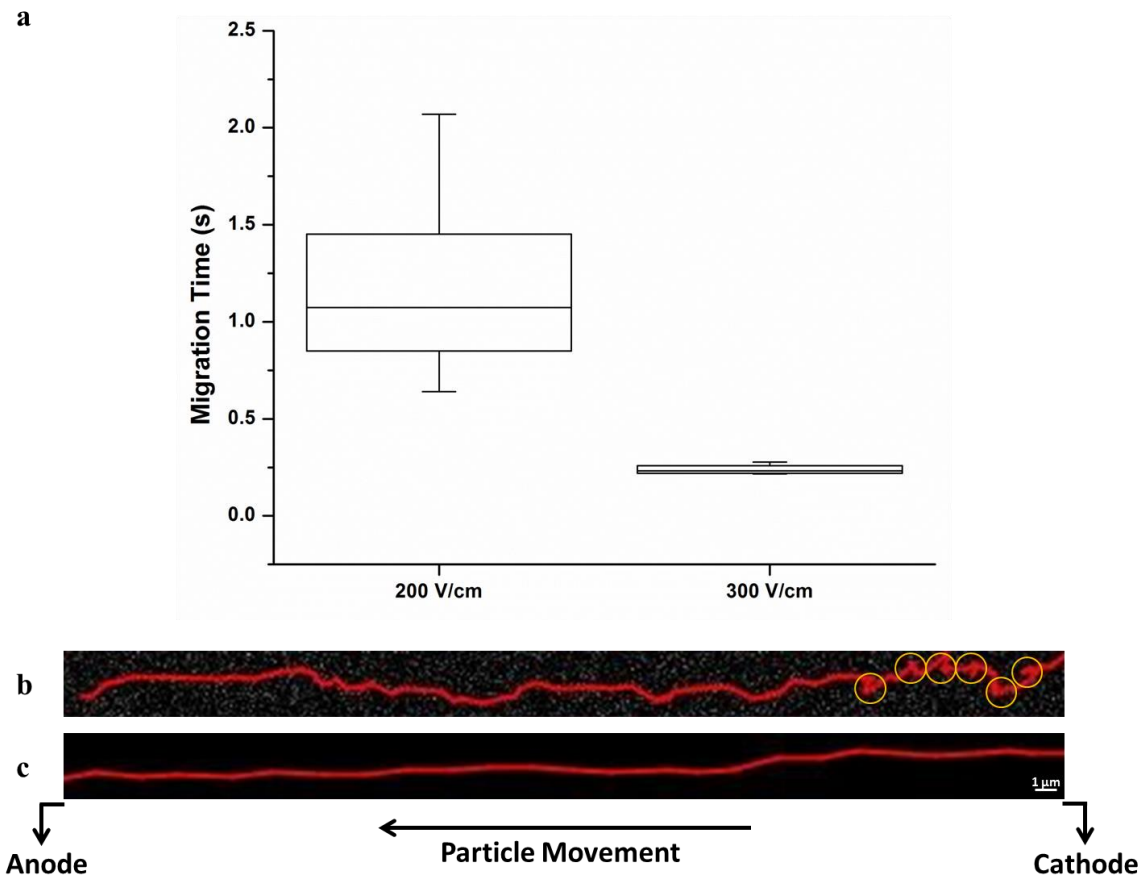

Figure 2–9 a) Box plot comparing the minimum, first quartile, median, third quartile and maximum migration time (s) for polystyrene beads at 200 V/cm and 300 V/cm migrating throughout the entire length (100 µm) of a COC nanoslit b) Trace of a single PS bead translocating a 3 µm x 150 nm x 100 µm (w x d x l) channel under a field strength of 200V/cm. Yellow circles indicate regions of possible recirculation. c) Trace of a single PS bead translocating a 3 µm x 150 nm x 100 µm (w x d x l) channel under a field strength of 300 V/cm. The depth of focus of our 100x objective was large enough to ensure that each PS bead remained in focus since our channel depth was 150 nm.

2.4 Conclusions

Nanoelectrophoresis provides unique phenomena, such as EDL overlap and increased surface effects that can be taken advantage of to generate separations that are difficult to realize using microscale columns. However, factors such as surface charge density and heterogeneity must be understood to predict how nanoscale-induced properties can affect the performance of the analytical process imposed on the nanochannel, especially when using amorphous materials such as

thermoplastics. Previous attempts to characterize thermoplastic surfaces were limited by averaging effects leading to an incomplete view of surface functional group heterogeneity following activation. In this study, we demonstrated a novel approach for characterizing the surface charge density and heterogeneity using super-resolution fluorescence microscopy (STORM). STORM allowed for the precise localization of fluorophores (17 nm) conjugated to –COOH charged surface functional groups allowing for an assessment of charge heterogeneity. Our data indicated that control of the dose used for activation can lead to optimal functional group surface density with higher surface density correlated to lower surface charge heterogeneity.

Furthermore, we utilized COMSOL to reconstruct fluid flow profiles in nanochannels with a heterogeneous distribution of point charges mapped from the STORM images to understand the effects of surface charge heterogeneity on the EOF. The simulations indicated that there were regions of fluid recirculation at point charges leading to both positive and negative velocities; however, the overall EOF magnitude was significantly less than a uniform channel, such as glass, due to the decreased overall surface charge. Our electrophoretic results indicated, however, that when the electric field strength is high (≥300 V/cm), stick/slip motion can be significantly reduced, meaning that any EOF-induced recirculation can be a minimal contribution to the overall zonal variance.

With the results presented herein, it should be feasible to consider the electrophoretic separation of single molecules in nanometer columns of short length (<100 μm) to produce high resolution separations of molecules in sub-10 ms time scales. This can provide the unique opportunity to employ nanoscale electrophoresis to affect the identification of single molecules through mobility matching. This strategy could potentially be envisioned for single-molecule DNA sequencing.[224,225] The generation of single mononucleotides from intact DNAs could be produced from immobilized exonucleases that cleave intact double-stranded DNA molecules.[167]

CHAPTER 3. CHARACTERIZATION OF ACTIVATED CYCLIC OLEFIN COPOLYMER: INFLUENCE OF THE ETHYLENE/NORBORNENE CONTENT ON THE PHYSIOCHEMICAL PROPERTIES

3.1 Introduction

The use of polymer substrates for microfluidic applications have been extensively reported in the literature.[57,58,226-239] In addition, nanofluidics using polymer substrates is a growing area of research due to the unique analytical capabilities offered by nanofluidic channels that are not accessible using microfluidics.[53,77,92,166,199] Some of the applications for both microfluidics and nanofluidics include microarrays,[177,178] solid-phase enzymatic reactors,[167,179,180] solid-phase extractors for nucleic acids and proteins,[181] affinity selection of biological cells,[57,182,183] chromatography,[184] and microchip electrophoresis.[161,185] In all of the aforementioned applications, surface modification was required in order to enable the intended application.

The attractive nature of thermoplastics for micro- and nanofluidic applications include the ability to use a wide variety of different fabrication strategies that are conducive to mass production, the low-cost of the substrate material and also, the wide selection of different substrate materials that can be employed to suite the particular application.[53,77,99] There are two general categories of polymeric materials that have been used in fluidic applications: (1) Elastomers and (2) thermoplastics. Elastomers, such as polydimethylsiloxane (PDMS), are amorphous polymers with a low to moderate number of cross-links between polymer chains. While the low Young's modulus ensures large deformation upon application of an external load, covalent cross-links help elastomers return to their original shape upon release of the load. Thermoplastics, such as poly(methyl methacrylate), PMMA, polycarbonate, PC, and cyclic olefin copolymer, COC, are linear or branched polymers with higher molecular weights and higher Young's moduli compared to PDMS.[77]

Polymers display a wide range of physiochemical properties allowing for the selection of the optimal material to match the needs of a particular application. A summary of the physiochemical characteristics of common polymers can be seen in Table 3-1. The wide range of mechanical properties, such as glass transition temperature (T_g) and coefficient of thermal expansion (CTE), allow for a diverse range of fabrication techniques, such as injection molding and hot embossing, to make the necessary structures in the device.[77] Furthermore, the range of chemical properties, such as refractive index and optical transmissivity, allow for the use of polymers for unique micro- and nanofluidic applications.

Polymers offer the advantage of being amenable to low-cost fabrication modalities leading to the realization of disposable point-of-care testing. PDMS has become a popular material for microfluidics due to its high O_2 and CO_2 permeability and optical transparency (UV to NIR), but it is easily deformable due

Material	T_g (°C)	CTE (α) ppm °C^{-1}	Refractive Index	Young's Modulus/ Gpa	UV Transmissivity	Visible Transmissivity
PDMS	-125	67.3	1.40	0.36-0.87 x10^{-3}	Excellent	Excellent
PC	145-148	60-70	1.584	2.0-2.4	Poor	Excellent
PMMA	100-122	70-150	1.492	1.8-3.1	Good	Excellent
COC	70-170	60-80	1.53	2.6-3.2	Excellent	Excellent

Table 3-1 Common polymers and their physiochemical properties.

to its low Young's modulus (*i.e.*, low compliance), has unstable surface chemistry and is susceptible to swelling in many solvents.[235,240] Thermoplastics, such as PMMA, and PC, possess a higher Young's modulus, are conducive to high scale production using replication based technologies, and their surface chemistry is more stable and can be easily modified using plasmas or UV/O_3 treatments.[53,77]

COC has become a common thermoplastic for many microfluidic applications due to its favorable physical characteristics. COC is highly resistant to organic solvents including polar solvents.[241] This thermoplastic shows low moisture absorption (<0.01%)[241] resulting in high fidelity structures that do not swell. COC also shows excellent optical clarity in the visible and ultraviolet regions of the

electromagnetic spectrum.[241] Furthermore, COC has a range of glass transition temperatures (T_g), low shrinkage and low birefringence.[104,241]

COC is manufactured commercially by several companies under various trade names. Within the literature these materials may be referred to as COC or COP (Cyclic Olefin Polymer). The key distinction is the use of either one monomer (COP) or multiple monomers (COC) to generate the thermoplastic. COC can be produced by chain copolymerization of cyclic monomers with ethylene. The cyclic monomer 8,9,10-triborborn-2-ene (norbornene) is used in TOPAS products while 1,2,3,4,4a,5,8,8a-octahydro-1,4:5,8-dimethanonaphthalene (tetracyclododecane) is used by APEL. Manufacturing techniques for COP include ring opening metathesis polymerization of various cyclic monomers followed by hydrogenation (ARTON, Zeonex and Zeonor).[242] Different types of COC can be produced based upon the composition of the monomer units used in its formulation, all which can affect the copolymer's physiochemical properties (see Table 3-2).

Topas Name	T_g (°C)	Norbornene mol %
8007	75	35.75
6013	130	50.75
6017	170	60.75

Table 3-2 Table showing the glass transition temperature (Tg) as a function of the % norbornene content for commercially available TOPAS COC.

Although COC and other thermoplastics show many favorable properties for fluidic applications, they can be hydrophobic resulting in high surface tension and back pressure, thus making the use of hydrodynamic pumping difficult in micro- and nanofluidic applications. In addition, their surfaces lack functional groups to allow for the covalent attachment of certain biologics to support the intended application. Therefore, activation of the thermoplastic to decrease its hydrophobicity as well as introduce functional groups for surface attachment or modification would be attractive. Studies regarding the hydrophobicity of COC have been explored.[57,243-245] These studies demonstrated that various activation methods (O_2, N_2, Ar plasmas or UV/O_3) can decrease the hydrophobicity of the

surface. The UV/O_3 activation process uses a quartz Hg lamp, which continually generates and destroys O_3 yielding a steady-state concentration of strongly oxidizing atomic O. The Hg lamp generates both 185 nm and 254 nm wavelength light. The 185 nm component splits O_2 resulting in O atoms that can react with O_2 to form O_3 while the 254 nm component breaks O_3 into atomic oxygen and O_2, thus yielding a steady-state concentration of atomic O. At sufficiently high energy, UV exposure and oxidative stress can generate radicals within the thermoplastic, which may break or scission polymer chains into smaller fragments, crosslink polymer chains, cause intramolecular rearrangements, and/or react with water or oxidative species to form carboxyl or other O-containing species.[57]

Plasma activation results in a source of highly energetic and reactive species that can interact with the thermoplastic surface. The electrons, ions, and free radicals generated during high energy irradiation of the plasma can promote breakage of C–H and C–C bonds. This leads to shorter polymer chains, the formation of other molecules through recombination reactions and crosslinking. When oxygen is present, chemical interactions between the oxygen molecules and the radicals in the reactive gas create more active radicals, which rapidly initiate chain reactions and form oxygenated products. These products, which may consist of hydroperoxides, carbonyls, carboxylic acids and peracids, are polar in nature and contribute to the hydrophilic nature of activated COC.[120]

Jackson *et al.* explored UV/O_3 activation of both COC 6013 from TOPAS and PMMA for the introduction of functional scaffolds to allow for the covalent attachment of antibodies for circulating tumor cell isolation.[57] This study showed that the high UV (254 nm) optical clarity of COC 6013 allowed for deeper penetration of the UV light into high aspect ratio microfluidic channels, compared to PMMA, generating a higher surface load of functional groups, such as carboxy groups.[57] Hwang *et al.* explored the surface activation of COC purchased from APEX by O_2 plasma treatment and showed that the COC surface acquired oxygen containing polar functional groups such as C-O and C=O, which increased as the plasma treatment time increased with a change in the water contact angle. The change in surface

functional groups was accompanied by a slight increase in surface roughness.[243] Roy *et al.* compared N_2 plasma to Ar and O_2 plasma for the activation of COC 6015 from TOPAS by evaluating the adhesion properties, electroosmotic flow (EOF) and the antifouling property of the activated surface. Their results showed a greater decrease in the water contact angle for N_2 plasma compared to Ar and O_2 plasma activated COC. They attributed this to the introduction of amide groups to the surface, which has a higher polarity than the oxygen containing species generated by Ar and O_2 plasma.[244]

Despite these studies in to the surface activation of COC, no study has explored the difference in activation based on the different ethylene/norbornene monomer ratios that can be used in the production of this thermoplastic (see Table 3-2). One advantage of COC is the range of physical properties that can be achieved based on the difference in the monomer ratios used in its formulation. For example, it is known that the increase in the T_g of COC is correlated with an increase in the mole fraction of norbornene as given by the following equation (Table 3-2):[241]

$$Norbornene\ mol\ \% = \frac{\left(T_g(Celcius)+65\right)}{4} \qquad (3.1)$$

In copolymers with ≤40% norbornene, the chemical structure of COC is comprised of alternating sequences of norbornene and ethylene units.[242] Higher norbornene contents stiffen the main chain, thus increasing the T_g, tensile strength and decreasing the ductility. Shin *et al.* explored the dependence of T_g on the cyclic monomer content and chemical structure of COC.[242] They reported a linear relationship between the cyclic monomer content and T_g. A difference was observed for COCs with different cyclic monomer units (norbornene or tetracyclododecanediyl). The polycyclic unit, tetracyclododecanediyl, which has a bulkier structure than the bicyclic unit norbornanediyl, leads to a restricted local motion of chain segments and thus higher T_g.

A relationship between norbornene mol% and the refractive index of the substrate has been noted.[246,247] These investigations showed that an increase in the mol% of norbornene increased the refractive index of the thermoplastic. Liu *et al.* also showed that the copolymer composition distribution

had a significant effect on the refractive index and transparency. For the same mol% of norbornene, the transparency of uniform compositions was higher when compared to non-uniform COC.[247]

A clear relationship between the physiochemical properties of COC and its composition has been established; however, the effect of COC composition on the surface properties following activation, either by UV/O_3 or O_2 plasma, has not been explored. This study sought to explore the differences in surface characteristics after activation of varying compositions of COC when exposed to UV/O_3 or O_2 plasma with a comparison made to polyethylene (PE), which does not contain the cyclic monomer, norbornene. Water contact angle (WCA), ATR-FTIR, UV/VIS, Toluidine blue O (TBO) assays, XPS, AFM and TOF-SIMS analyses were performed to thoroughly assess differences in three different monomeric ratios of COC from TOPAS. COC from TOPAS is manufactured by a chain copolymerization reaction of norbornene and ethylene. This study investigated TOPAS's COC 8007, 6013 and 6017 copolymers (see Table 3-2). COC 8007 is described as a clear grade with a T_g of 75°C. COC 8007 has a lower elastic modulus and higher elongation than other TOPAS COC grades.[241] COC 6013 is described as a clear grade with a T_g of 130°C and COC 6017 is a clear grade with a T_g of 170°C.[241] This investigation will present information to understand the effects of the norbornene content on the physiochemical properties of activated COC, which would have profound implications on the performance of micro/nanofluidic devices made for different COC compositions.

3.2 Experimental Methods

3.2.1 Reagents and Materials

Cyclic olefin copolymers (COC 8007, 6013 and 6017) were purchased from TOPAS Advanced Polymers (Florence KY) in either 1.5 mm or 100 μm thick sheets. Polyethylene was purchased from Goodfellow (Coraopolis, PA). Frame-sealed incubation chambers were purchased from Bio-Rad (Hercules, CA). Chemicals and reagents used in these studies included sodium carbonate and

bicarbonate (Fisher Scientific, Houston, TX); acetic acid (Sigma-Aldrich, St. Louis, MO), and toluidine blue O (TBO; Carolina Biological Supply, Burlington, NC).

3.2.2 Activation of COC

UV/O_3 and O_2 plasma activation was conducted on each substrate. UV/O_3 exposure was performed in a home-built UV activation chamber equipped with a quartz, low-pressure Hg lamp at various intensities (21.85 mW/cm^2, 19.43 mW/cm^2 and 16.01 85 mW/cm^2) for 0, 5, 10 and 15 min. Oxygen plasma activation was performed in a FEMTO plasma cleaner from Electronic Diener (Ebhausen, Germany) with a gas flow of 10 sccm at various wattages (30 W, 50 W and 70 W) for 0, 12, 36 and 60 s.

3.2.3 Water Contact Angle Measurements

Water contact angles were obtained using a VCA Optima instrument (AST Products). For each of these measurements, 2.0 µL of NanoPure water (pH 7.5) was deposited onto the surfaces followed by collecting the image and measuring the contact angle using the manufacturer's software. The measurements reported were the average of six replicates at various positions on the substrate.

3.2.4 Attenuated Total Reflectance Fourier Transform Infrared Spectroscopy (ATR-FTIR)

ATR-FTIR measurements were performed on UV/O_3 treated 100 µm thick COC plates. The measurements were not performed on O_2 plasma treated substrates, because the plasma activation only modified the first few monolayers and thus, did not provide sufficient signal for viable observations. ATR-FTIR spectra were acquired from 375–4000 cm^{-1} using an ALPHA FTIR spectrometer and a platinum ATR module (Bruker Optics). Five replicates were performed and spectra were analyzed using Essential FTIR analysis software. Peaks were baseline corrected and total peak area of relevant peaks were assessed.

3.2.5 X-Ray Photoelectron Spectroscopy (XPS)

For XPS measurements, C 1s and O 1s photoelectron signals were acquired using an Axis Ultra DLD X-ray photoelectron spectrometer (Kratos Analytical) under ultra-high vacuum conditions (base pressure 6 x 10^{-9} Torr) with a monochromatic Al Kα X-ray source, 20 eV pass energy, and 0° electron take-off angle. A charge neutralizer was used to prevent charging. Given an inelastic mean free path of 3-4 nm, ~95% of the resultant signal originated 9-12 nm from the surface.[248-250]

3.2.6 Time of Flight- Secondary Ion Mass Spectrometry (TOF-SIMS)

TOF-SIMS analyses were conducted using a TOF SIMS V (ION TOF, Inc. Chestnut Ridge, NY) instrument equipped with a Binm+ (n = 1 - 5, m = 1, 2) liquid metal ion gun, Cs+ sputtering gun and electron flood gun for charge compensation. Both the Bi and Cs ion columns were oriented at 45° with respect to the sample surface normal. The instrument vacuum system consisted of a load lock for rapid sample loading and an analysis chamber separated by the gate valve. The analysis chamber pressure was maintained below 5.0 x 10^{-9} mbar to avoid contamination of the surfaces to be analyzed. For the depth profiles acquired in this study, 10 keV low energy Cs+ with 20 nA current was used to create a 120 µm by 120 µm area, and the middle 50 µm by 50 µm area was analyzed using about 0.3 pA Bi3+ primary ion beam. The negative secondary ion mass spectra were calibrated using H-, C-, O-, C3-, C5- and C7-.

3.2.7 UV/VIS

The transparency for native and activated 100 µm thick COC was measured using an Ultrospec 4000 UV/Vis spectrophotometer (Pharmacia Biotech) and acquired between 200 and 800 nm.

3.2.8 Atomic Force Microscopy (AFM)

The topographies of non-activated and O_2 plasma treated COC with 3 different norbornene contents were investigated. AFM measurements were performed on the same sample before and after O_2 plasma treatment using the Asylum Research MFP-3D Atomic Force Microscope (tip radius ~2 nm) in repulsive tapping mode at a rate of 1.0 Hz. The Tap300A1-G cantilever tips (Ted Pella) had a frequency

of 300 kHz and force constant of 40 N/m. The scans were taken over a 2 x 2 µm area, which were presented in 3D and RMS surface roughness computed using the manufacturer's software.

3.3 Results and Discussion

Activation of thermoplastic surfaces by UV/O_3 or O_2 plasma results in photo-oxidation and chain scissioning of the thermoplastic.[251] Photo-oxidation results in the formation of radicals and chain scissioning leads to the presence of shorter polymer chains compared to the unexposed thermoplastic.[57,251] Prolonged exposure can result in photoablation of the surface as well.[57,251] Activation with oxygen sources typically results in the formation of oxygen containing functional groups on the surface such as alcohols, aldehydes, ketones and carboxyl functional groups. Previous literature has explored the density and distribution of these generated functional groups showing that COC 6013 had greater –COOH surface functional group densities compared to PMMA with a heterogeneous distribution of these groups following activation.[57,252] But, no work has explored differences in the generation of these functional groups between different monomer compositions of COC.

Although most fluidic applications require the activation of the thermoplastic to generate a substrate with higher surface energy, there are different requirements for the degree of activation. For instance, the immobilization of biologics, such as antibodies, onto the surface require the generation of a high number of surface functional groups.[57] However, electrophoresis applications may require a reduced surface charge for the generation of a smaller electroosmotic flow (EOF). Application specific requirements of thermoplastic devices requires a thorough understanding of the effect of substrate composition on the extent of activation. This understanding will allow for the informed and precise selection of a thermoplastic for a specific fluidic application. Thus, we embarked upon looking at different types of COC in terms of the physiochemical properties following UV/O_3 or O_2 plasma activation.

3.3.1 Water Contact Angles of Activated COC and PE

Water contact angle measurements can serve as an assessment tool to survey the hydrophilicity of a surface, although it does not offer functional group identification. For the sessile water contact angle measurements (WCA), NanoPure (pH 7.5) water was deposited (2 µL) onto the surfaces of native and activated substrates and the WCA was determined to evaluate the surface hydrophilicity/hydrophobicity, which is indicative of the formation of polar functional groups on the surface generated by the activation process. UV/O_3 and O_2 plasma activated COC and PE results are shown in Figure 3–1. All native COC and PE surfaces showed high WCAs indicative of a more hydrophobic surface. Upon activation with UV/O_3 (Figure 3–1a-c), the WCA decreased indicating a more hydrophilic surface likely due to the generation of polar surface functional groups as a result of activation. For PE, the minimum WCA was significantly higher, ~60°, compared to all of the COC grades. At 21.85 mW/cm^2 UV/O_3 exposure for 15 min, we did see an increase in the contact angle for PE (Figure 3–1c), which could have arisen from surface ablation or further radical reactions roughening the surface.[243] COC 8007, which has 35.75% norbornene content, showed a minimum contact angle of 41° for 16.01 mW/cm^2 after 10 min of irradiation, 38° for 19.43 mW/cm^2 after 15 min and 37° for 21.85 mW/cm^2 after 5 min. A table showing the specific dose of each treatment can be found in Table 3-3.

Power (mJ/s*cm²)	Exposure Time (s)	Radiance (J/cm²)
16.01	300	4.803
	600	9.606
	900	14.409
19.43	300	5.829
	600	11.658
	900	17.487
21.85	300	6.555
	600	13.11
	900	19.665

Table 3-3 Table of doses for UV/O3 treated COC samples

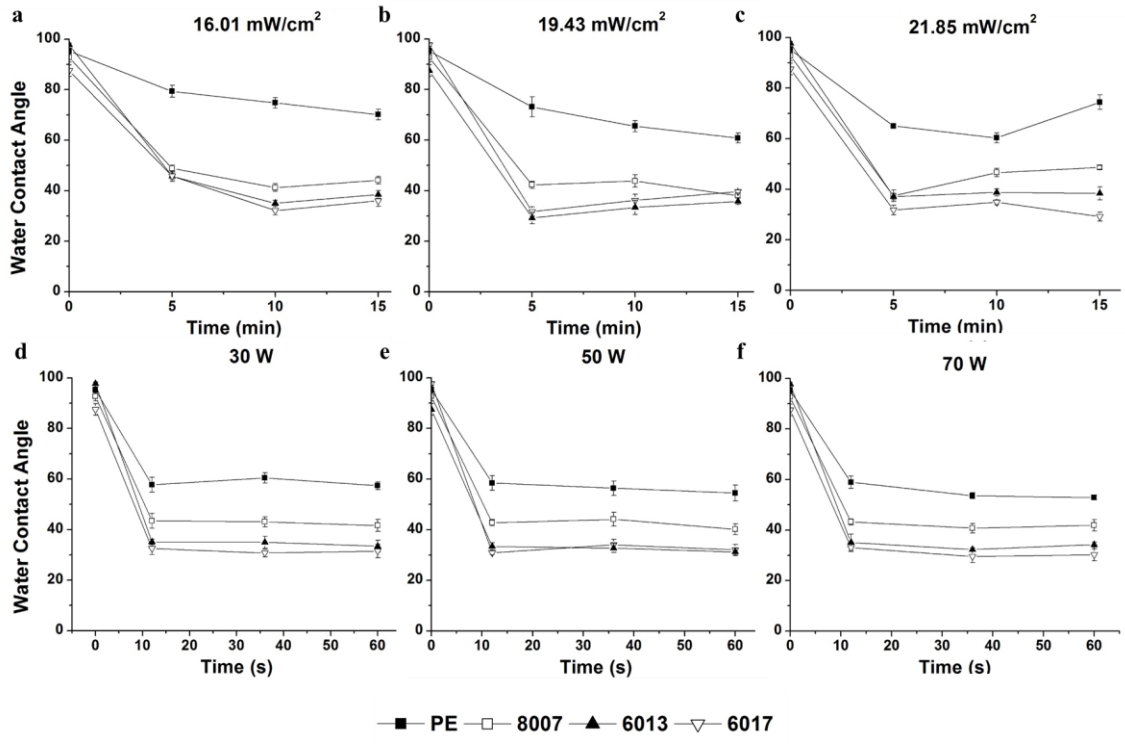

Figure 3–1 Water contact angle for activated TOPAS COC and polyethylene (PE). a) 16.01 mW/cm2 UV/O3 activated COC b) 19.43 mW/cm2 UV/O3 activated COC c) 21.85 mW/cm2 UV/O3 activated COC d) 30 W O2 activated COC e) 50 W O2 activated COC f) 70 W O2 activated COC. Error bars show ±stdev of average WCA n=5

COC 6013, which has a 50.75% norbornene content, showed a minimum contact angle of 34° for 16.01 mW/cm^2 after 10 min, 31° for 19.43 mW/cm^2 after 5 min and 37° for 21.85 mW/cm^2 after 5 min. COC 6017, which has 60.75% norbornene content, showed a minimum WCA of 32° for 16.01 mW/cm^2 after 10 min, 29° for 19.43 mW/cm^2 after 5 min and 29° for 21.85 mW/cm^2 after 15 min. We also noticed an increase in the water contact angle for longer exposure times after the minimum had been reached for COC, most likely due to surface roughening. Overall, COC 8007 showed a significantly higher WCA (more hydrophobic) when compared to COC 6013 and COC 6017. Furthermore, PE, which lacks the cyclic norbornene unit, showed the highest water contact angle after activation. O_2 plasma activated COC and PE results can be seen in Figure 3–1 d-f. Similar trends were observed when compared to the UV/O_3 activated surfaces. A sharp decrease in the WCA occurred after the first 10 s of exposure to O_2 plasma regardless of the wattage. In contrast to UV/O_3 activation, we did not see an increase in the WCA after prolonged exposure. PE had the highest WCA of the substrates investigated with a value of 57°, which was similar to the WCA obtained through UV/O_3 exposure. COC 8007 maintained an average WCA of 41° regardless of the activation dose, which was significantly higher than COC 6013, which had an average water contact angle of 33°. COC 6017 had an average WCA minimum of 31°.

This data indicated that there is a difference in the hydrophilicity of the surface after activation, which is dependent on the norbornene content of the thermoplastic. We note that an increase in surface roughness may contribute to the higher WCAs for activated thermoplastics. Thus, AFM measurements were carried out to deduce these roughening effects (see below). Two different processes could occur during activation irrespective of the activation source; photo-oxidation and chain scissioning reactions. The presence of low molecular weight fragments on the surface may affect the WCA measurement. For example, thermoplastics such as PMMA, have shown a drop in the WCA following activation followed by a higher WCA after being rinsed with a solvent, which removes the low molecular weight fragments.[57] However, literature has shown that the generation of these low molecular

weight fragments occur to a lesser degree in COC compared to PMMA.[57]

3.3.2 ATR-FTIR Analysis of UV/O3 Activated COC and PE

To understand the chemical functional groups responsible for the decrease in the WCA of activated COCs and PE, ATR-FTIR experiments were performed. As stated, ATR-FTIR has penetration depths ranging from 0.5-2 μm into the bulk material.[253] Thus, only UV/O_3 activated surfaces showed sufficient ATR-FTIR signals as the activation process occurs into the bulk of the thermoplastic, whereas O_2 plasma activation occurs only within the first few monolayers of the surface. As an example, ATR-FTIR spectra for all COC types and PE exposed to 21.85 mW/cm^2 UV/O_3 for 15 min can be seen in Figure 3–2a. All samples showed peaks ranging from 2940–2860 cm^{-1}, which corresponded to the -CH stretching mode (ethylenic H and aldehydic H) and a peak at 1454 cm^{-1}, which corresponded to the -CH bending mode; these are in good agreement with previously reported results.[120,254,255] We observed a decrease in the overall peak intensity and peak area in this spectral region for activated substrates compared to the native material. We did observe an increased peak intensity and peak area around 1744 cm^{-1} for all activated substrates with those thermoplastics containing greater norbornene content showing the greatest change. This region is associated with the presence of carbonyl groups that could have been produced from photo-oxidation reactions occurring during activation and can be seen in Figure 3–2b.[244,255] The greatest carbonyl intensity was correlated with the lowest alkane intensity after activation. Furthermore, an ATR-FTIR peak in the 3500–3600 cm^{-1} range was present for the activated substrates. This peak indicated the presence of hydroxyl groups (–OH), which could also contribute to the increased hydrophilic nature of the COC surface following activation and was shown to have the greatest intensity for COC substrates with the highest norbornene content. The native COC and PE substrates did not show absorbance in the carbonyl or hydroxyl regions within the IR spectrum, further supporting that activation results in the generation of oxygen containing functional groups. To quantify the difference in oxygen containing functional groups between the various thermoplastics, the oxygen to carbon ratio for each

thermoplastic was plotted as a function of the exposure time as seen in Figure 3–2c-f. For all substrates, greater O/C ratios were seen for 21.85 mW/cm^2 when compared to 19.43 mW/cm^2 and 16.01 mW/cm^2 for similar exposure times, which is to be expected due to the higher dose. PE showed little change in the O/C ratio with increased dose, with a maximum O/C ratio of 0.03. The maximum O/C ratios were 0.24 for COC 8007, 0.60 for COC 6013 and 0.75 for COC 6017. The greatest O/C ratio was observed for the thermoplastic with the greatest norbornene content, which agreed with the increasing hydrophilicity of thermoplastics with greater norbornene mol% observed with the WCA data. In addition, the increase in the O/C ratio from the native substrate to substrates exposed to 5 min of 21.85 mW/cm^2 UV/O_3 treatment showed a linear relationship (R^2 = 0.99) with the norbornene content (Figure 3–3). After the 5 min exposure, there was still an increase in the O/C ratio, however, the percent increase was not as drastic for all of the substrates as that seen within the first 5 min of activation. For instance, COC 6017 showed a 22-fold increase in the O/C ratio from 0 min to 5 min exposure to 21.85 mW/cm^2 UV/O_3 activation, but only a 2-fold increase from 5 min to 10 min exposure. Figure 3–4 shows the change in the carbonyl peak area for all substrates as a function of the wattage. Once again, there was a significant difference in the carbonyl peak area for all substrates with COC 6017 showing the greatest peak area and PE showing the least. The peak area increases with the norbornene content as observed in the O/C ratio (Figure 3–2c-f).

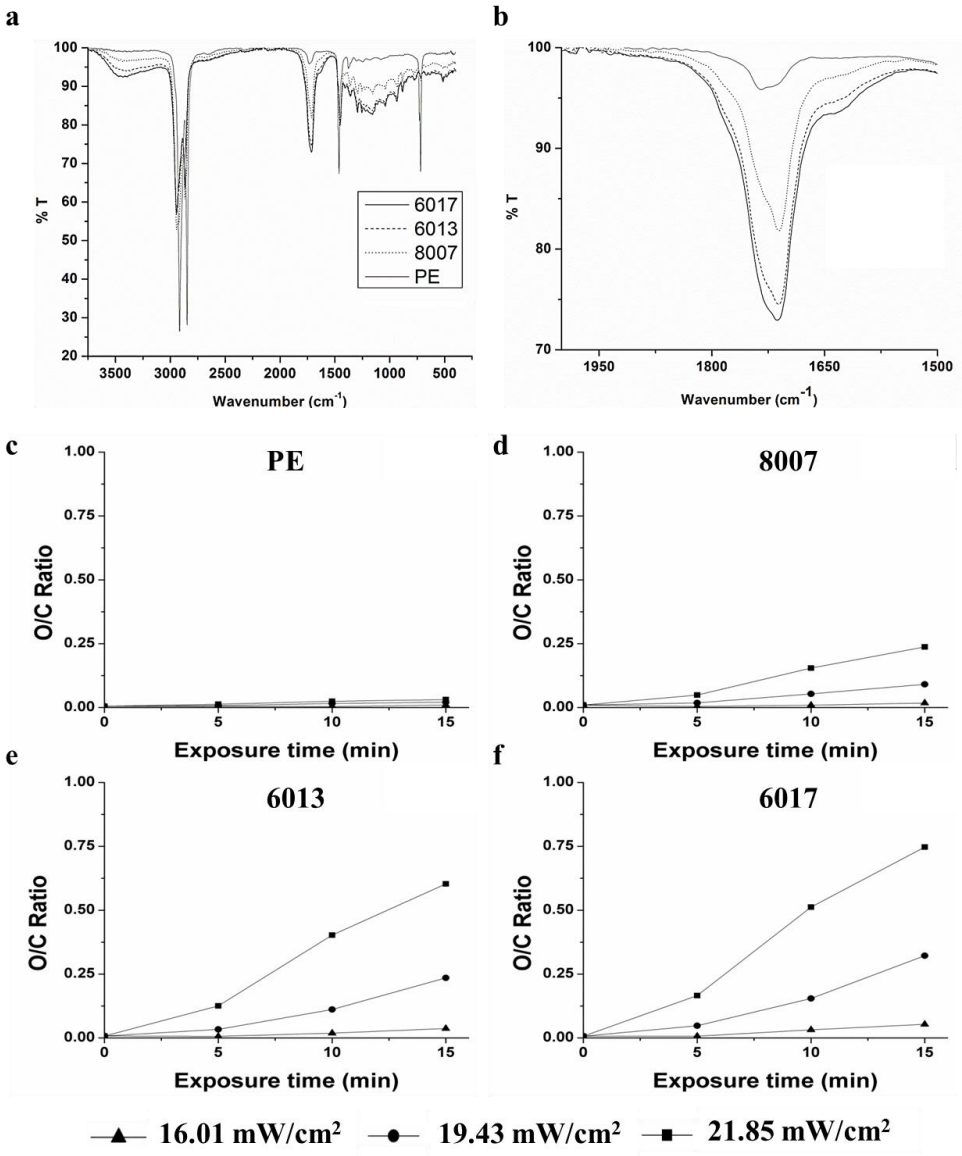

Figure 3–2 ATR-FTIR analysis of UV/O3 activated TOPAS COC and PE. a) ATR-FTIR spectrum of PE and COC exposed to 21.85 mW/cm2 of UV/O3 for 15 min. b) Sub-section of the spectrum seen in (a) showing the carbonyl region of the spectrum c-f) Oxygen to carbon ratio vs. exposure time for various doses of UV/O3 activation for PE, 8007, 6013 and 6017, respectively.

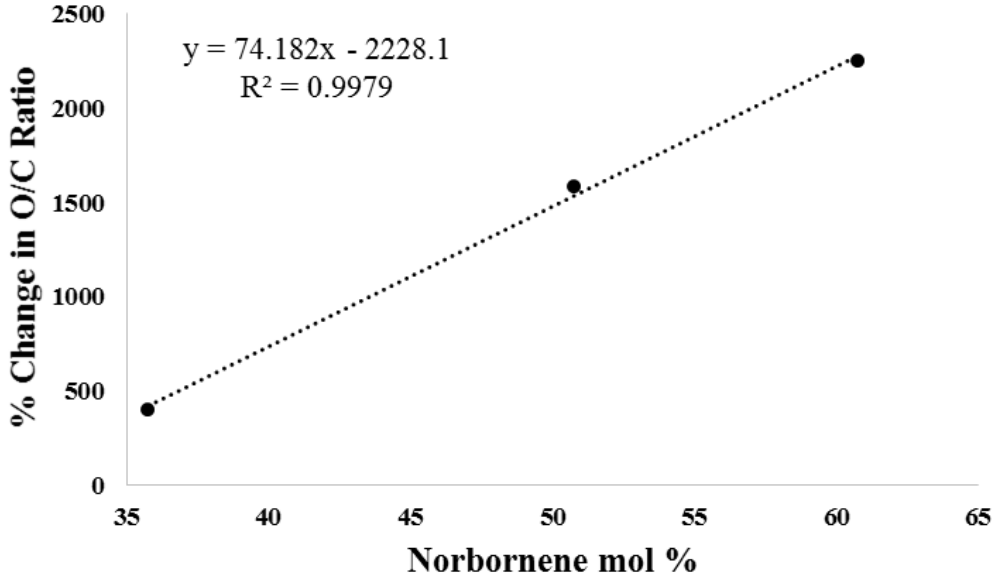

Figure 3–3 Plot showing ATR-FTIR evaluated percent change in O/C ratio for 0 min exposure to 5 min exposure versus the norbornene content for COC substrates exposed to 21.85 mW/cm2 UV/O3. A linear best fit function is shown as the dotted line; R2 = 0.9979.

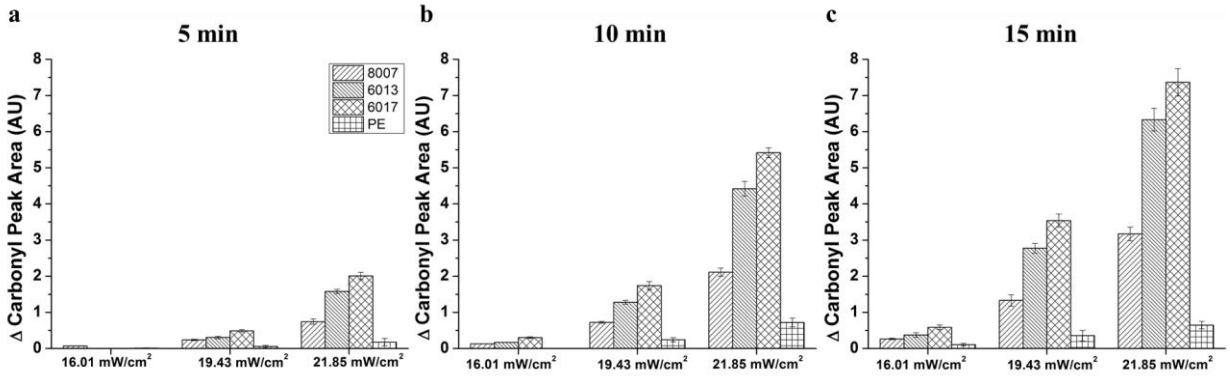

Figure 3–4 Change in the carbonyl peak area vs the UV/O3 activation power for a) 5 min exposure b) 10 min exposure and c) 15 min exposure. Error bars represent ±stdev of the average –COOH peak area, n=5

3.3.3 X-Ray Photoelectron Spectroscopy (XPS)

We further explored the O/C carbon ratio using XPS, which interrogates electrons released from 1-10 nm of the surface and is thus, more surface sensitive compared to ATR-FTIR.

Figure 3–5a shows the high resolution C 1s spectra for COC 8007 and COC 6017 activated with 21.85 mW/cm^2 UV/O_3 for 15 min, while Figure 3–5b shows the O/C ratio versus exposure time for COC and PE samples activated with 21.85 mW/cm^2 UV/O_3 radiation. In the full XPS spectra, we saw almost no oxygen containing functional groups before activation of the thermoplastics, but we did observe a large increase in the oxygen content after activation (Figure 3–6). All samples showed a dramatic increase in the O/C ratio after 5 min exposure with COC 6017 showing a significantly higher O/C when compared to all other samples with a 100-fold increase in the O/C ratio after 5 min exposure. This trend continued with further exposure to UV/O_3 radiation with COC 6017 showing significantly higher O/C ratios for all exposure times as supported by the high resolution C 1s spectra (

Figure 3–5a). The highest O/C ratio achieved for each thermoplastic was 31.6%, 23.7%, 18% and 13% for COC 6017, 6013, 8007 and PE, respectively. The highest O/C ratio was observed after 15 min exposure for all thermoplastics except COC 8007, which showed the greatest O/C ratio after 10 min. This may be due to the greater percentage of ethylene chains within the thermoplastic, which may undergo chain scissioning reactions and further radical reactions, thus potentially removing any generated oxygen containing functional groups.[57] Taken together, both ATR-FTIR and XPS showed significantly higher oxygen containing functional groups for COC containing greater norbornene contents.

3.3.4 UV-VIS Spectroscopy of COC and PE

One attractive property of COC is its excellent optical properties in its non-activated form, making it appropriate for microfluidic or nanofluidic applications requiring optical detection. Activation of the thermoplastic, however, may have an effect on this optical transparency. Our investigations here aimed to determine how the norbornene content affected the optical clarity of the material following

UV/O_3 or O_2 plasma activation. For these measurements, 100 µm thick plates were activated via O_2 plasma (70 W for 60 s) and UV/O_3 (21.85 mW/cm^2 for 15 min) and the percent transmittance was determined using

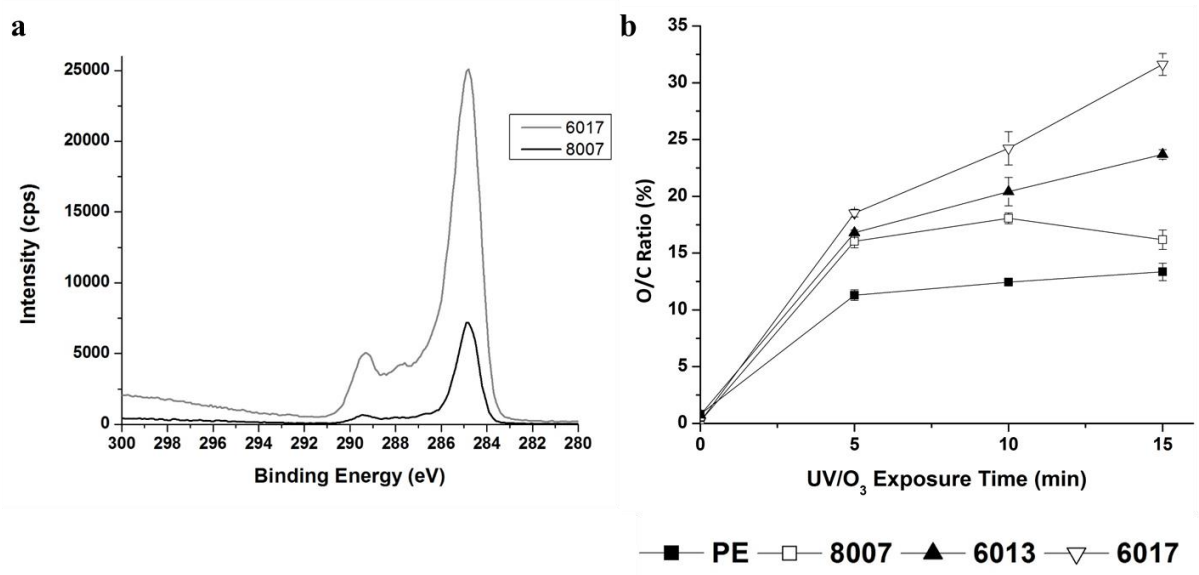

Figure 3–5 a) Sample high resolution C 1s XPS spectra for UV/O3 activated 6017 and 8007 (21.85 mW/cm2 for 15 min) b) O/C ratio versus exposure time for 21.85 mW/cm2 UV/O3 activated PE (filled square), 8007 (open square), 6013 (filled triangle) and 6017 (open triangle). Error bars represent ±stdev of the average O/C ratio n=3

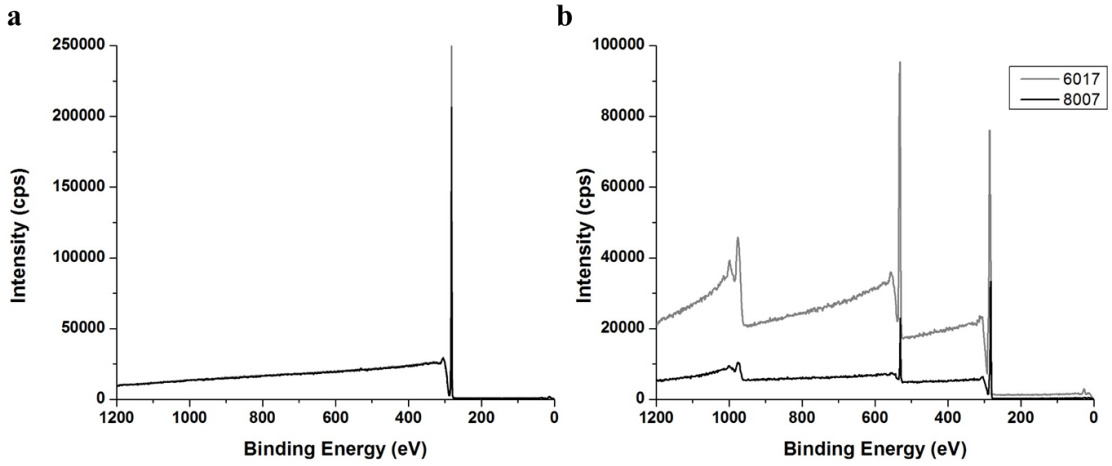

Figure 3–6 Full XPS spectra showing: a) Native COC 6017 and COC 8007 and b) UV/O3 activated COC 6017 and 8007 (21.85 mW/cm2 for 15 min).

UV/VIS spectrophotometry. Percent transmittance is dependent on the thickness of the substrate as observed by Khanarian *et al*.[104] and therefore, we selected a 100 µm thick plate in all cases, which is a thickness typically used as a cover plate for microfluidic devices.[71,74,87,166]

Figure 3–7a shows the percent transmittance as a function of wavelength for O_2 plasma treated COC, while Figure 3–7b shows the percent transmittance as a function of wavelength for UV/O_3 activated COC. Overall, O_2 plasma activated substrates showed no deviation from the native spectra, with 90% transmittance (T) at wavelengths >400 nm while UV/O_3 activated substrates had significant decreases in their %T when compared to the native substrates. Native COC 8007 showed 83% transmittance while native COC 6013 showed 74% and native COC 6017 showed 62% T (Figure 3–8). As stated, these values were not significantly different for O_2 plasma treated substrates; however, UV/O_3 treated COC 8007 had a %T of 69%, 53% for COC 6013 and 38% for COC 6017. All substrates showed a decrease in transmissivity at 254 nm after UV/O_3 exposure with COC 6017 showing the greatest decrease (38.7% decrease) and COC 8007 showing the smallest (16.8 % decrease). Our data indicated that greater surface activation was present with higher norbornene contents, which may be the cause for decreased UV transmissivity. Beyond 475 nm, all substrates regardless of composition or activation showed approximately 90% transparency.

3.3.5 Time-of-Flight Secondary Ion Mass Spectrometry (TOF-SIMS)

It has been speculated that UV/O_3 activation penetrates within the bulk of the substrate due to the UV transparency of COC, but to our knowledge no published data has supported this claim. We sought to investigate the activation depth of COC with UV/O_3 treatment as well as differences between various COC compositions. TOF-SIMS is a highly sensitive surface analytical technique that can secure elemental and molecular information with high spatial and mass resolution.[256] A finely focused, pulsed primary ion beam

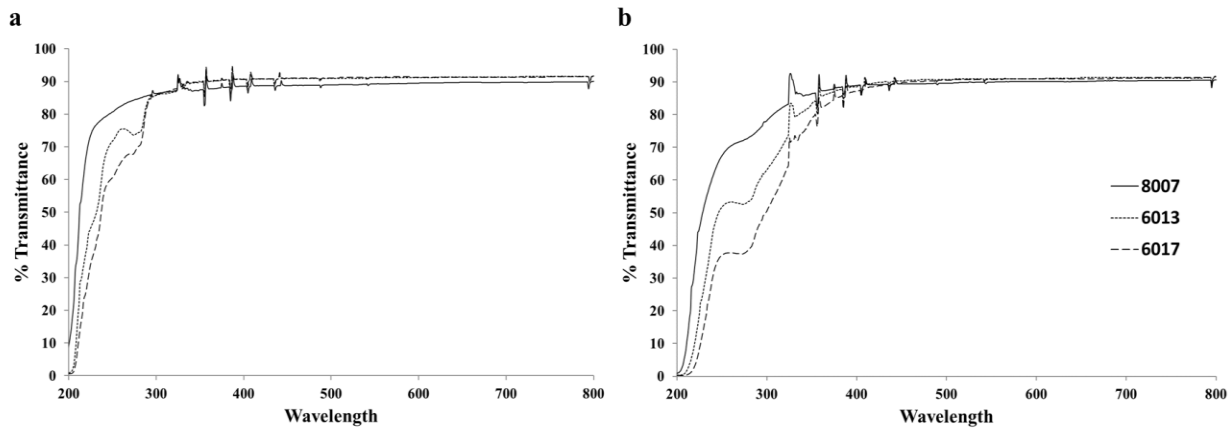

Figure 3–7 UV-VIS spectrum for TOPAS COC after a) 70 W O2 exposure for 60 sec and b) 21.85 mW/cm2 UV/O3 exposure for 15 min. All spectrum show a decrease in the % transmittance when compared to native substrates (Figure 3–8).

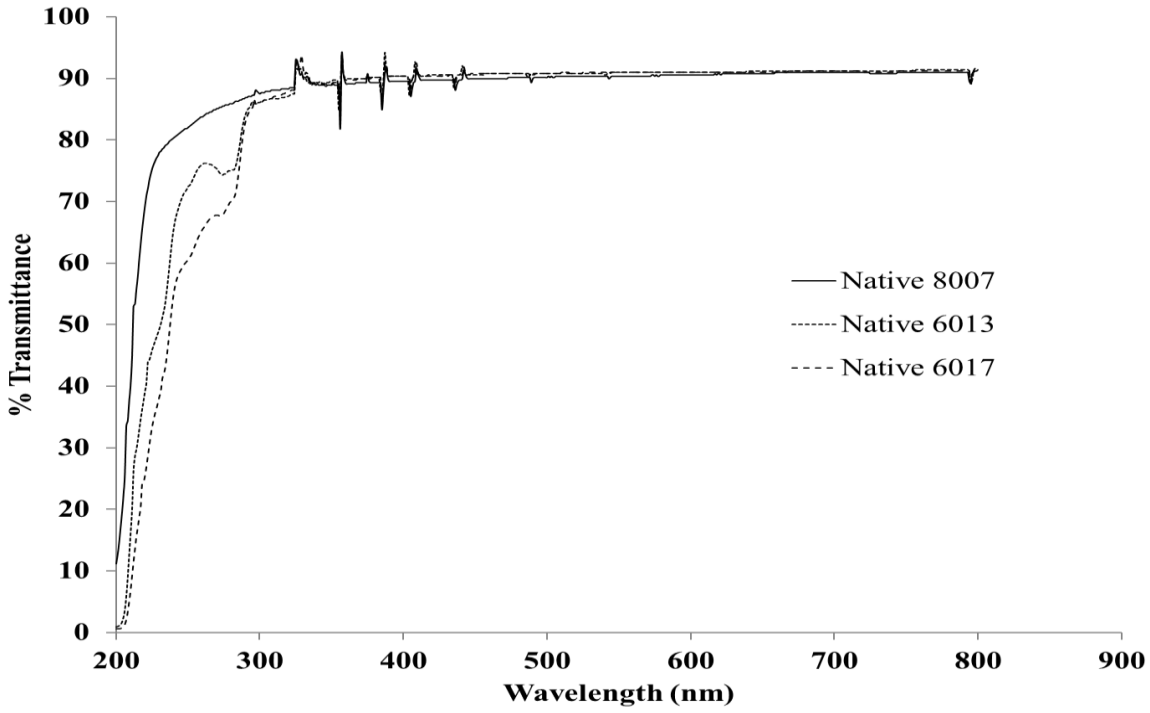

Figure 3–8 UV-Vis spectra for native COC 8007, 6013 and 6017.

is rastered across the surface of the sample and the secondary ions emitted at each pixel are extracted into a time-of-flight mass spectrometer. With dual beam operation, depth profile of ions can be obtained. The Cs+ ion gun ablates the surface (~1 nm/s) while the Bi^{3+} ion gun is used to generate secondary ions for analysis. For the purposes of these experiments, we compared COC 8007 and COC 6017 both activated with 21.85 mW/cm^2 UV/O_3 for 15 min to the native thermoplastic.

As can be seen in Figure 3–9, UV/O_3 activated COC 8007 and COC 6017 showed a significant increase in the O^- content of the substrate compared to the non-activated substrate. The greater degree of oxygen containing functional groups for COC 6017 when compared to COC 8007 was in agreement with both the XPS and ATR-FTIR data. Consistent with our supposition that UV/O_3 activation also produced modifications into the bulk (see the ATR-FTIR data), the presence of oxygen-containing species were found at depths up to 450 nm, albeit with a decrease in the amount of these species as one penetrates deeper into the substrate. TOF-SIMS profiles of O_2 plasma activated COC 8007 and 6017 substrates were investigated as well, but the O^- ion only showed a significant difference from the native COC for the first seconds of sputtering (data not shown) indicating that O_2 plasma activation was restricted to the surface.

It is interesting to note that although native COC 6017 showed 30% less transparency than native COC 8007 at 254 nm, it showed greater O content deeper within the substrate. We would anticipate to see a greater presence of O species for COC 8007 deeper within the bulk polymer because the UV radiation should penetrate deeper into the substrate due to its higher transparency. This may suggest a strong dependence of the norbornene content of the thermoplastic for oxygen implantation.

3.3.6 Assessment of –COOH Surface Functional Group Density on Activated COC using TBO Assay

As previously discussed, the generation of specific functional groups on the surface of thermoplastics during activation is key for various fluidic applications. Of great interest is the generation of surface –COOH groups that can serve as a functional scaffold for the attachment of biological entities, such as antibodies,[57]

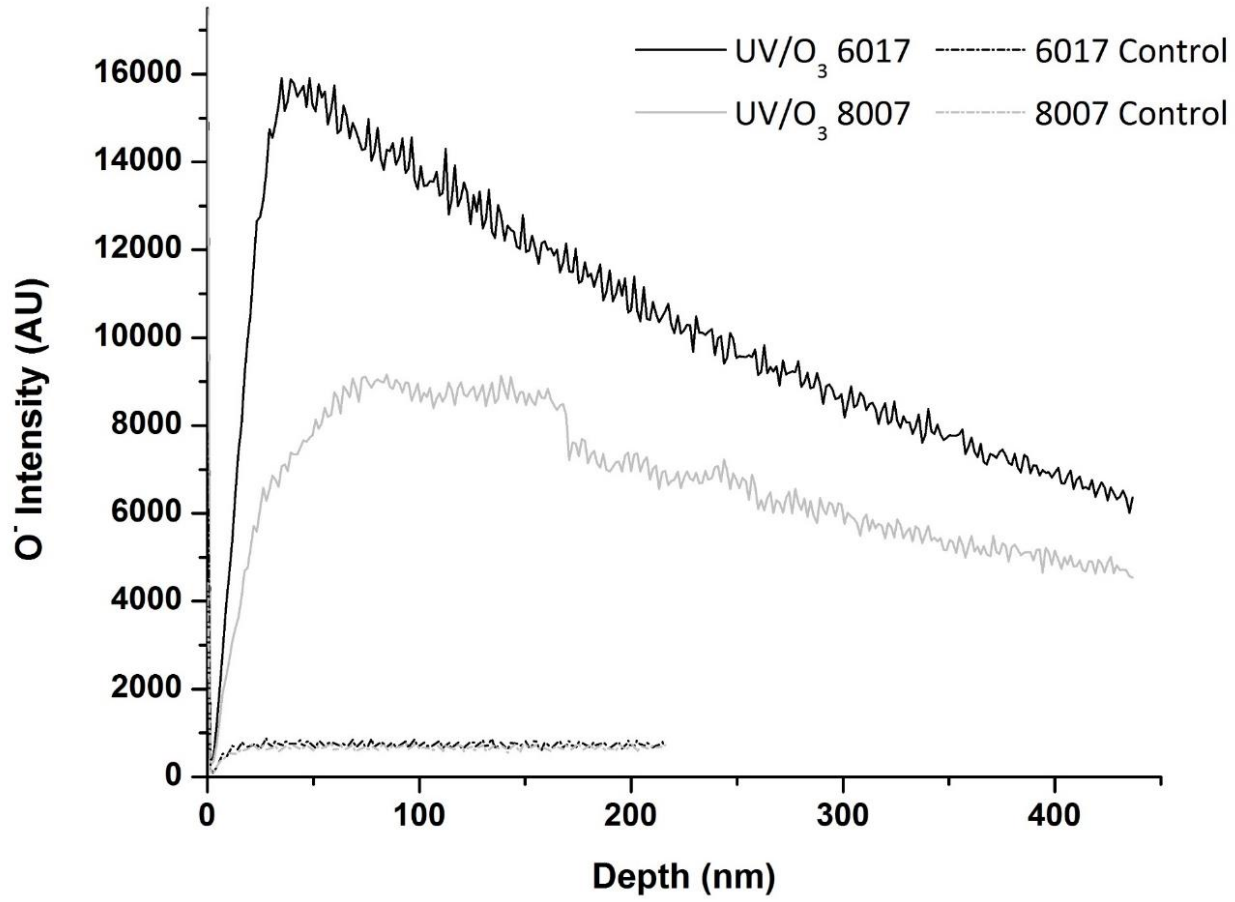

Figure 3–9 TOF-SIMS data showing the intensity of the oxygen ion vs depth for 21.85 mW/cm2 UV/O3 activated 6017 (black) and 8007 (gray) compared to native 6017 (black dash) and native 8007 (gray dash).

or for deprotonation to generate surface charge that can control the electroosmotic flow.[74] Previous literature has shown differences in the surface –COOH functional group density and heterogeneity of COC 6013 compared to PMMA.[57,71] Here, we sought to investigate the differences in various compositions of COC on the surface load of –COOH groups. To investigate these differences, we utilized a colorimetric assay with a cationic dye, TBO, which binds electrostatically (1:1) to deprotonated –COOH groups. COC plates (1.5 mm thick) were activated with 21.85 mW/cm^2 UV/O_3 for 15 min, incubated with a TBO solution, washed, and the electrostatically bound TBO molecules released using acetic acid and the effluent evaluated spectrophotometrically. The TBO assay not only probes surface functional groups, but also can probe molecules in underlying layers due to the generation of a porous surface caused by photofragmentation reactions occurring on surfaces. Consequently, absolute carboxyl surface densities are not reported, rather relative densities are shown (see Figure 3–10). COC 6017 showed higher ($p < 0.001$) –COOH functional group densities compared to COC 6013 and COC 8007. While TBO can penetrate into the bulk of the thermoplastic due to photo-fragmentation, the degree of photo-fragmentation is known to be minimal for COC.[57]

3.3.7 Atomic Force Microscopy (AFM) to Determine Surface Roughness Following Activation

As previously discussed, surface roughness can have an effect on the WCA. Furthermore, surface roughness can be problematic for many fluidic applications, especially for nanofluidics, as it can generate undesired wall interactions or dielectrophoretic trapping.[87] Thus, we explored differences in surface roughness of various activated COC thermoplastics. For these studies, the initial RMS surface roughness of native COC thermoplastics was measured using AFM. Then, each substrate was exposed to 30 s of 50 W O_2 plasma, as this treatment can serve as an effective strategy for thermal fusion bonding cover plates to thermoplastic substrates,[87] and the RMS roughness was re-measured following this treatment. The raw data is presented in

Table 3-4. In Figure 3–11 3D AFM plots of native COC 8007 (Figure 8a) and native COC 6017 (Figure 3–11c) as well as O_2 plasma treated COC 8007 (Figure 3–11)

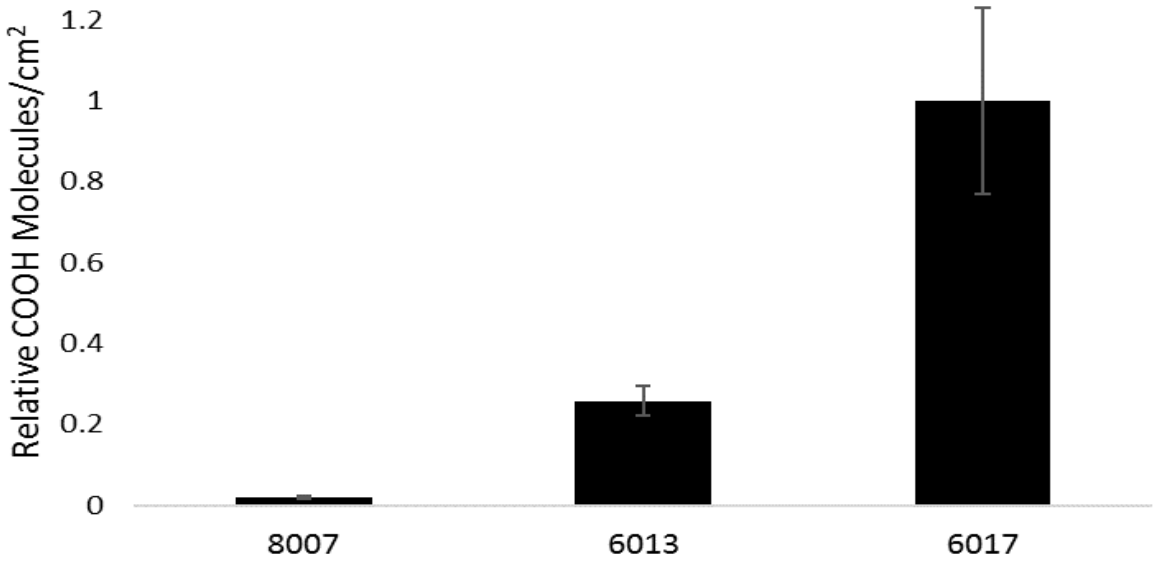

Figure 3–10 Results from TBO assay to probe surface -COOH molecules on various 21.85 mW/cm2 UV/O3 activated thermoplastic substrates. Results show the relative COOH molecules/cm2, normalized to 6017 which showed the highest COOH functional groups. As the norbornene increases the relative COOH amount increases as well. Error bars represent ±stdev of the relative –COOH molecules/cm2 n=3

		Native Polymer RMS Roughness		O_2 Activated Polymer RMS Roughness			
Polymer	**Area Size (µm)**	**Average (nm)**	**Std. Dev (nm)**	**Average (nm)**	**Std. Dev (nm)**	**Δ RMS Roughness**	**Δ RMS Roughness Std.**
COC 8007	2	2.12	0.19	3.07	0.48	0.94	0.52
COC 6013	2	1.23	0.03	2.03	0.54	0.80	0.54
COC 6017	2	2.45	0.08	3.12	0.30	0.67	0.31

Table 3-4 Raw AFM RMS roughness data for native and O_2 plasma treated COC.

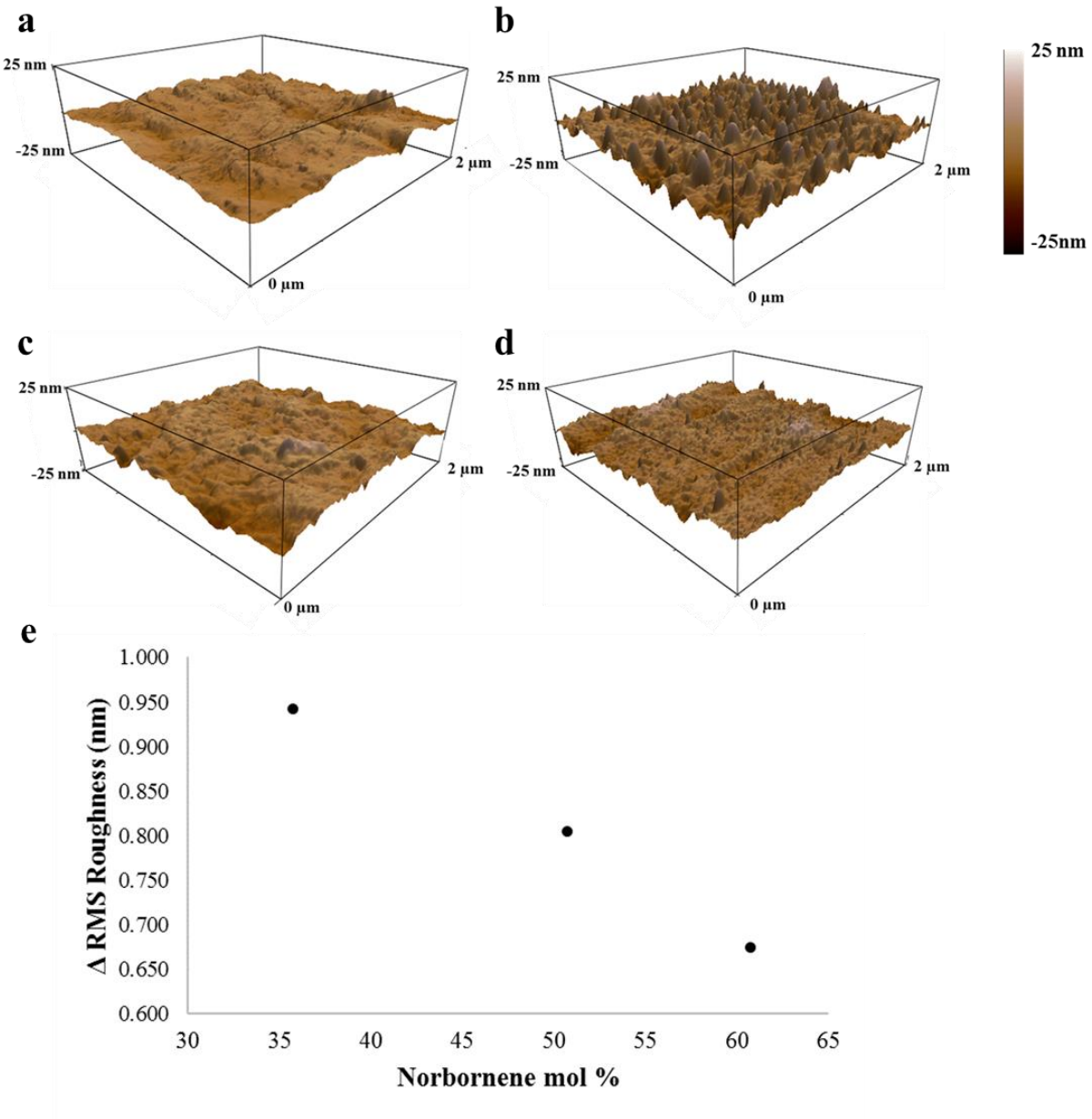

Figure 3–11 Sample 3-D AFM images of COC 8007 a) native and b) 50 W 30 s O2 plasma treated compared with COC 6017 c) native and d) 50 W 30 s O2 plasma treated to show an increase in roughness upon activation for both substrates with greater RMS roughness observed for COC 8007. e) shows the change in the RMS roughness versus the norbornene mol % confirming that an increase in the norbornene mol % shows a decrease in the RMS roughness. Raw data can be found in Table 3-4.

Figure 3–11 and COC 6017 (Figure 3–11 d) substrates are shown. As can be seen, O_2 plasma activation increased the surface roughness of both COC 8007 and COC 6017. Figure 3–11 e plots the difference in the O_2 plasma treated and native substrate RMS roughness as a function of the norbornene mol%, which indicated that as the norbornene mol% increased, a decrease in RMS roughness of the activated surface was seen. The process of O_2 plasma activation promotes the breakage of C–H and C–C bonds leading to the generation of shorter polymer fragments and surface ablation, both of which can roughen the activated surface. Our AFM data indicated that increased norbornene mol% may decrease the chain scissioning observed while the spectroscopy data showed greater formation of oxygenated products for thermoplastics with greater norbornene content.

3.4 Conclusions

COC is an attractive thermoplastic for micro- and nanofluidics due to its resistance to organic solvents, low moisture absorption, optical clarity in the visible and ultraviolet regions of the electromagnetic spectrum, range of glass transition temperatures (T_g), low shrinkage and low birefringence.[104,241] These properties allow for a wide range of fabrication modalities that can be imposed on the material to generate structures across many different length scales with high compliancy. However, due to its hydrophobic nature, activation of COC is required to increase its surface energy allowing for more favorable wettability. Many studies have explored the effects of various activation methods on COC. The physiochemical properties of COC are dependent on the composition of various COC types and our study aimed to investigate differences in these properties following activation.

Several different analytical approaches were used to probe the surface characteristics of activated COC such as the sessile WCA measurements, ATR-FTIR, XPS, TOF-SIMS, UV-VIS, AFM and a colorimetric assay utilizing TBO. WCA analysis showed that increased norbornene content led to a more hydrophilic surface following UV/O_3 or O_2 plasma activation, which was supported by

spectrophotometric analysis (ATR-FTIR and XPS); COC 6017 (60.75% norbornene) had higher oxygen containing functional groups compared to COC 8007 (35.75% norbornene). TBO analyses indicated that COC 6017 contained higher –COOH groups relative to the other COC types, which may be important for fluidic applications requiring large EOFs or functional scaffolds for the attachment of various biologics. Furthermore, TOF-SIMS confirmed that COC 6017 contained O containing groups 450 nm deep into the thermoplastic when activated by UV/O_3, while O_2 plasma only activated the surface of the thermoplastic. AFM results coupled with our ATR-FTIR data indicated that increased O containing groups of COC with greater norbornene content did not necessarily lead to a rougher surface. In fact, greater norbornene content resulted in a decrease in the RMS roughness making COC 6017 an attractive substrate for nanofluidic applications, which requires surfaces that are not prone to excessive wall interactions and/or dielectrophoretic trapping. Despite the greater norbornene content, COC did show a decrease in the UV transparency, especially for UV/O_3 treatment.

Our data provides key insights into the selection of a COC type and activation protocol for particular fluidic applications. Taken together, our data suggests the selection of COC 6017 for applications requiring a high load of –COOH functional groups. But, the attachment of biologics can be limited by: a) The number of –COOH groups for attachment; and b) packing density limitations of the molecule of interest. Thus, the absolute number density of functional groups created by activation may be inconsequential for the immobilization of large biologics due to the limited packing density of such molecules.

Of great importance for the selection of a thermoplastic for fluidic applications is the ability to fabricate the desired structures with high compliance. Leech studied the hot embossing of COC as a function of the norbornene content and found that at temperatures above the T_g, the embossed patterns were independent of the COC grade, indicating that high fidelity structures can be embossed into any COC grade.[257] However, COCs with a higher norbornene content exhibited micro-cracking during embossing at temperatures close to the T_g. Thus, careful selection of embossing parameters are required.[257]

CHAPTER 4. INVESTIGATION IN TO THE NANOSCALE SEPARATION OF DEOXYNUCLEOTIDE MONOPHOSPHATES (DNMPS): TOWARD TIME OF FLIGHT (TOF) DETECTION FOR SINGLE MOLECULE DNA SEQUENCING

4.1 Introduction

Electrophoresis allows for the separation of cations, anions and neutral molecules based on differences in their electrophoretic mobility when placed in an electric field.[105] The electrophoretic mobility of a molecule is determined by its charge to size ratio, as seen in Equation 4.1;

$$\mu_{ep} = \frac{q}{6\pi\eta r} \tag{4.1}$$

where q is the charge on the molecule, η is the viscosity of the buffer and r is the hydrodynamic radius of the molecule. Capillary Zone Electrophoresis (CZE) is a form of electrophoresis and is typically performed in fused silica capillaries with an inner diameter ranging from 50-75 µm.[105] In this process, "zones" of analyte migrate through the capillary with an apparent velocity given by Equation 4.2;

$$v_{app} = \mu_{eof}E + \mu_{ep}E \tag{4.2}$$

where μ_{eof} is the mobility of the electroosmotic flow (EOF) and E is the field strength applied. As can be seen from Equation 4.1, the mobility of the molecule can be manipulated through a change in pH, because this would change the charge on the analyte. Beyond CZE, other electrophoresis separation modes can be utilized, such as Micellar Electrokinetic Chromatography (MEKC), which adds a surfactant to the background electrolyte (BGE) that is typically added at a concentration beyond its critical micelle concentration to create a pseudo-stationary phase. Analytes are separated using MEKC by differential

partitioning between micelles (pseudo-stationary phase) and a surrounding aqueous buffer solution (mobile phase) as well as differences in their electrophoretic mobilities.[105]

Although conventional capillary electrophoresis has had great success in the separation of numerous analytes, there have been recent efforts to perform nanoelectrophoresis due to the unique separations made possible when operating within the nanometer regime.[4,36,67,68,195,196] For example, it has been shown that dsDNA fragments can be separated in nanochannels without the need for a sieving medium when the channel dimensions are on the order of the Debye length (λ_D),[258] which is not possible in microchannels due to the free draining conformation of the DNA molecules.

Electrokinetic transport of molecules on the nanoscale is influenced by several physical parameters such as the electric double layer (EDL) and the surface charge-to-volume ratio. The EDL thickness, known as the Debye length (λ_d) is defined in Equation 4.3, where R is the gas constant ($J \cdot mol^{-1}K^{-1}$), ϵ_r is the dielectric constant of the medium, F is the Faraday constant ($C \cdot m^{-1}$), and T is the temperature (K) and c is the ionic concentration of the electrolyte solution:[4,36,67,68,195,196]

$$\lambda_d = \sqrt{\frac{\varepsilon_o \varepsilon_r RT}{2F^2 c}} \qquad (4.3)$$

As λ_d approaches the column dimensions, EDL overlap occurs, which introduces a parabolic flow profile rather than the classically observed plug like flow typically seen in CZE allowing for unique separations on the nanoscale.[4,67] Furthermore, the increased surface-to-volume ratio allows for the propensity for enhanced molecule/surface interactions, thus allowing for additional separation based on hydrophobic and electrostatic interactions. Potential interactions of analytes with walls can induce “stick-slip” motion and can have dramatic effects on nanoscale separations.[71,166] In addition, “stick-slip” motion can be induced by dielectrophoretic trapping artifacts generated by surface roughness on the nanoscale giving rise to inhomogeneous electrical fields resulting in momentary trapping along the wall.

Weerakoon-Ratnayake *et al.* investigated the separation of silver nanoparticles (AgNP) within nanoscale PMMA columns.[166] Dark field microscopy was used to track the transport of AgNPs within these devices with varying slit dimensions, buffer ionic strengths and applied field strengths. The authors were able to demonstrate the separation of silver nanoparticles (AgNPs) based on size without the addition of buffer additives, which was not possible within microscale columns. The best resolution observed between 60 and 100 nm AgNP was achieved at higher electric field strengths due to the limitations of stick-slip motion at these high fields.

O'Neil *et al.* was able to show differences in the transverse electromigration of 20 nm polystyrene (PS) beads traveling through PMMA nanoslits at varying field strengths.[71] At low electric field strengths (200 V/cm), the PS beads had much greater interaction with the surface resulting in increased electrophoretic migration time and increased standard deviation. However, a 50% increase in the electric field strength (300 V/cm) generated a 600% decrease in the electrophoretic migration time. Further, the relative standard deviation of migration times was reduced from 40% at 200 V/cm to 8% at 300 V/cm, a 5-fold decrease.

Due to the unique advantages offered by nanoelectrophoresis, we sought to explore the ability to separate deoxynucleotide monophosphates (dNMP) with this method. The ability to separate all four dNMPs shows great promise in applications such as DNA sequencing. Recently, single-molecule sequencing (SMS) has been suggested as an attractive alternative to ensemble-based sequencing because it can eliminate the need for polymerases used in traditional sequencing modalities, as well as potentially provide longer read lengths. SMS is accomplished by detecting the four nucleotides comprising the DNA polymer using optical, electrical or magnetic properties.[259] The advantages of SMS are that DNA fragments are not required to be amplified. This removes the time and cost for these amplification processes and the inherent error with polymerases.[260] Furthermore, SMS has other

advantages such as sequencing of large DNA fragments, low sample input requirements, no-labeling and real time readout.

One approach to SMS includes nanopore sequencing, which can use naturally occurring pores such as α-hemolysin or synthetic pores made by nanofabrication techniques. Pores required for DNA sequencing typically require dimensions on the order of 2-5 nm. For nanopore sequencing, each nucleotide of an intact DNA molecule produces a characteristic modulation of ionic current through the nanopore as the DNA molecule is electrically transported through this pore; the order of these modulations reflects the sequence of bases within the starting DNA molecule.[261] However, resolution is insufficient to identify each nucleobase and as such, the base calling accuracy is poor.[262-265] This poor resolution results from similarities in the size and shape of the nucleobases and also, the intrinsic thickness of the pore; the nanopore allows ~15 nucleobases to span the pore at one time, which leads to current modulations arising from multiple nucleotides.[265] Furthermore, the speed at which the DNA is translocated through the pore does not accommodate bandwidth limitations set by the current measuring instrumentation.[261] Synthetic nanopores have recently been employed to circumvent challenges associated with the naturally occurring pores, such as pore stability, fixed pore dimensions and difficulty in isolating a single pore.[264,266-268] Iqbal *et al.* previously demonstrated the ability of solid-state nanopores combined with the appropriate chemistry to sort biomolecules at the single-molecule level.[269] Liang et al. demonstrated the ability to measure electrical conductance changes of a DNA biopolymer moving through an in-plane electrode nanogap (9 nm) for single 1.1 kbp double-stranded DNAs.[33] However, the transport dynamics in the measurement of single nucleotide bases for DNA primary structure determinations has not been demonstrated.

An alternative nanopore approach for SMS involves disassembling the intact biopolymer into its discrete monomer units (*i.e.*, mononucleotides), which provides better spatial resolution addressing the issue with multiple nucleotide occupancy within in single pore. This can be accomplished by the covalent

attachment of an exonuclease to the lip of the pore that can sequentially cleave a single nucleotide base from the intact DNA molecule and directing each nucleotide base, one at a time, through the nanopore for electrical identification.[270] To facilitate readout of the single nucleotide base, an adaptor (cyclodextrin) is included into the natural pore structure for enhancing single nucleotide detection. A challenge with this approach, however, is diffusional misordering.[271] In addition, this single nucleotide detection approach is still limited by high error rates because nucleotide bases are identified using current blockage events, which show poor discrimination of the nucleotide bases.

Limitations of current SMS technologies prevent high base call accuracy (<0.1% error) required for many sequencing applications. To address these issues, we are developing an innovative SMS strategy that cleaves dsDNAs using a processive enzyme to generate individual mononucleotides. As seen in Figure 5–1 the process of DNA sequencing module initiates with the immobilization of enzyme in the nanopillar. To accomplish this task, a clipping enzyme such as λ-exonuclease is tethered to the solid nanopillar support that can processively clip the single nucleotide units from the dsDNA strand in to their monophosphate form. This bioreactor can be activated by the introduction of Mg^{2+} in to the fluidic channel.[272] The released dNMPs are electro kinetically transported through the flight tube (nanochannel) with the travel time determined by the applied electric field, the length of the flight tube and the number of dNTP:channel wall interactions. Identification of the nucleobases is enabled by molecular-dependent flight times of dNMPs within thermoplastic nanochannels. Thus, a thorough understanding of the translocation of dNMPs through thermoplastic nanochannels along with parameters with which we can enhance resolution between dNMPs to allow for high base call accuracy, will be required.

Separation of dNMPs has been achieved through conventional electrophoresis methods by various researchers, most commonly using alkaline solutions for the BGE. Alkaline solutions provide a stable EOF, thus coated capillaries are not needed to eliminate or stabilize the EOF.[273] Sodium borate is

the most commonly used alkaline buffer for dNMP separation.[274-277] Beyond sodium borate, other researchers have used sodium and ammonium carbonate buffers, which provides a stable baseline and adequate resolution.[278] In addition to CZE, MEKC has been used for the separation of nucleotides as well. The most common buffer used is a combination of phosphate and borate salts with 10-100 mM Sodium dodecyl sulfate (SDS) added as a surfactant.[279-281] Surfactants such as cetyltrimethylammonium bromide (CTAB) have been used as well, which reverses the EOF and drastically reduces the separation time.[282]

Although a clear foundation for the separation of dNMPs is reported in the literature, no study to our knowledge, has investigated the separation of dNMPs on the nanoscale or explored differences in separations performed in conventional CE compared to nano-CE. With the goal of Time of Flight (ToF) detection, we sought to investigate the dynamics and various contributions to the zonal dispersion of migration times through nanochannels with different longitudinal voltages, surface chemistries and λ_D values. These observations will allow for an understanding of scale-dependent dispersion effects. Theory and experimental studies for electrokinetic separations in nanochannels has appeared in recent reviews.[66,68] For ion transport with d/λ_D ratios ranging from 1-10, anomalous transport behavior has been observed, such as charge-dependent ion speeds due to TEM resulting from wall/solute electrostatic effects,[70,258,283] with maximum resolution occurring when the column diameter is 1-10 times λ_D.[284] Pennathur and Santiago determined that electrokinetic separations in nanochannels were dependent on ion valence, ζ (zeta potential), ion mobility and λ_D.[258,283] For example, Garcia *et al.* illustrated the electrokinetic separation of the fluorescent dyes Alexa 488 (negatively charged) and rhodamine B (neutral) in Si nanochannels of various widths ranging from 35 to 200 nm.[285] The mobility of the fluorescent dyes was based on their charge and interaction(s) with channel walls. We also investigated how various parameters associated with the BGE would affect the separation of the four naturally occurring nucleotide monophosphates, guanine (dGMP), adenine (dAMP), cytosine (dCMP),

and thymine (dTMP), as well as methylated cytosine (mdCMP). The monophosphate form of these molecules was selected because these are the form generated upon cleavage from dsDNA by λ-exonuclease. Comparisons were also provided between conventional electrophoresis of these nucleotides and nanoelectrophoresis using thermoplastic nanochannels.

4.2 Experimental Methods

4.2.1 Reagents and Materials

Silicon <100> (Si) wafers were purchased from University Wafers (Boston, MA). Poly(methylmethacrylate), PMMA, substrates and cover plates were purchased from Good Fellow (Berwyn, PA) and cyclic olefin copolymer (COC 8007 and 6017) was purchased from TOPAS Advanced Polymers (Florence, KY). An anti-adhesion monolayer of (Tridecafluoro – 1,1,2,2 – Tetrahydrooctyl) Tricholorosilane (T-Silane) was purchased from Gelest, Inc. Tripropylene glycol diacrylate (TPGA), trimethylolpropane triacrylate (TMPA), Irgacure 651 (photo-initiator), 1-ethyl-3-[dimethylaminopropyl] carbodimide hydrochloride (EDC), thymidine 5'-monophophate disodium salt, 5-methylcytosine monophosphate disodium salt, cytidine 5'-monophosphate disodium salt, adenosine 5'-monophosphate disodium salt and guanosine 5'- monophosphate disodium salt, triethylammonium acetate (TEAA), cetyltrimethylammonium bromide (CTAB), (4-(2-hydroxyethyl)-1-piperazineethanesulfonic acid, 2-amino-2-methyl-1-propanol (AMP), methanol (MeOH) were purchased from Sigma-Aldrich (St. Louis, MO). Tris-borate buffer and sodium hydroxide (NaOH) was obtained from Fisher Scientific (Houston, TX). ATTO-532 dye was purchased from Atto-Tec (Siegen, Germany). All required dilutions were performed using 18 MΩ/cm milliQ water (Millipore technologies) and all measurements were performed at 25°C unless specified otherwise.

4.2.2 Electrophoretic Conditions

4.2.2.1 Instrumentation and Capillary Details

Conventional microscale electrophoresis experiments were performed using an Agilent G1600ax instrument equipped with a variable-wavelength detector set to 254 nm. Both CZE and MEKC separations were performed using a 50 µm inner diameter (ID) fused silica capillary that was 64.5 cm in length with an effective length of 56 cm. Pre-conditioning of the fused silica capillaries was performed for 10 min with 0.5 M NaOH, 2 min with H_2O, 5 min with 0.1 M NaOH and finally with the run buffer for 5 min.

4.2.2.2 CZE Separation Conditions

Injections of the mononucleotides was performed using pressure injection (90 mbar*sec). The electrophoresis was then run at 25°C with a run voltage of 25 kV (E = 387 V/cm) utilizing a 1 mM Mg^{2+} and 1X TBE BGE at varying pH values. Mesityl Oxide was used as a neutral marker.

4.2.2.3 MEKC Separation Conditions

Separations conditions were adapted from Hong *et al*.[282] The run voltage was set at -20 kV (310 V/cm) and used a BGE comprised of 75 mM 2-amino-2-methyl-1-propanol (AMP), 20 mM NaCl and 6 mM cetyltrimethylammonium bromide (CTAB) adjusted to pH 9.0.

4.2.3 Fluorescent Labeling of dNMPs

The protocol for the conjugation of ATTO 532 to each dNMP was modified from Cornelius *et al.* [286] The reaction scheme used can be seen in Figure 4–1. In brief, 100 µL of each dNMP (1 mM in 100 mM HEPES pH 6.5) was mixed with 100 µL EDC (300 mM in 100 mM HEPES) and 100 µL of ATTO 532 dye (25 mM in 100 mM HEPES) and reacted overnight while shaking at 37°C. The reaction mixtures were then separated and purified using a Jasco HPLC equipped with a Jasco FP-2020 plus fluorescent detector at λ_{ex}= 532 and λ_{em}= 553.

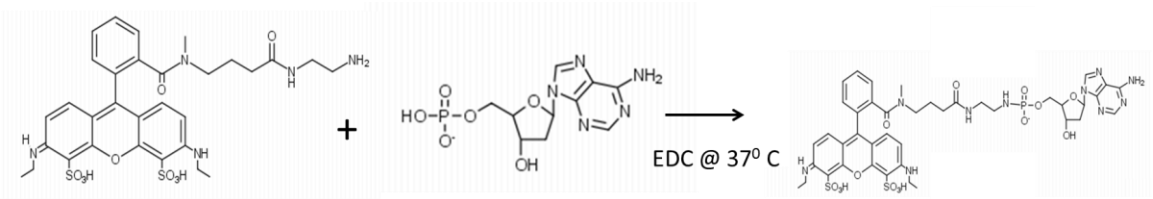

Figure 4–1 Reaction scheme showing the conjugation of Atto 532 to adenosine monophosphate. 100 µL of each dNMP (1 mM in 100 mM HEPES pH 6.5) was mixed with 100 µL EDC (300 mM in 100 mM HEPES) and 100 µL of ATTO 532 dye (25 mM in 100 mM HEPES) and reacted overnight while shaking at 37 °C

The column used was an ODS Hypersil RP 18 column (10 mm ID, 150 mm length, particle size 5 µm) with a linear gradient from 0 to 35 % ACN (1% per min) in 0.1 M triethylammonium acetate (TEAA), pH 7.0 with a flow rate of 5 mL/min. Fractions were then collected and concentrated using an Eppendorf concentrator 5301 set at 30°C with vacuum for 24 h. Samples were then removed and confirmed with ESI-MS using a NanoMate equipped Quattro II mass spectrometer. All samples were then stored at -20°C.

4.2.4 Fabrication of Nanochannel Devices

The fabrication of nanochannels in thermoplastics has been detailed elsewhere.[53,77] Briefly, a silicon master was fabricated by initially patterning two access microfluidic channels (55 µm wide, 12 µm deep, 1.5 cm long) into a Si <100> wafer using standard photolithography followed by anisotropic etching with 45% KOH. Next, 110 nm x 110 nm nanofluidic slits were patterned by FIB milling of the Si wafer using a Helios NanoLab 600 Dual Beam instrument (FEI, Hillsboro, OR). An anti-adhesion monolayer of (Tridecafluoro – 1,1,2,2 – Tetrahydrooctyl) Tricholorosilane (T-Silane) was applied. A resin stamp was then made using UV-NIL from a UV-curable polymeric blend containing 68 wt% TPGA as the base, 28 wt% TMPA as the crosslinking agent and 4 wt% Irgacure 651 as the photo-initiator that was coated onto a rigid COC back plate. The stamp was cured by exposure to 365 nm light (10 J/m^2) through the COC back plate for 7 min in a CL-100 Ultraviolet Crosslinker (UVP, LLC, Upland, CA). The UV-cured resin was gently demolded from the Si master. The stamp was imprinted into a 1.5 mm thick piece of

COC by NIL with access holes used as reservoirs. NIL was performed at a pressure of 2888 kN/m^2 for 120 s with the top and bottom plates maintained at a temperature of 95ºC using a Hex03 thermal imprinter (JenOptik AG, Jena, Germany). Pressure was applied after 30 s and was maintained during imprinting until the system was cooled to 45°C. A 100 µm thick COC sheet of the same type as the substrate was used as the cover plate. Both the COC substrate and cover plate were pre-activated with oxygen plasma at a dose known to generate high loads of –COOH functional groups.[71] Thermal assembly was performed immediately at 70°C for 900 s using 977 kN/m^2 pressure. SEM images of the SI Master, Stamp and Imprinted chip can be seen in Figure 4–2.

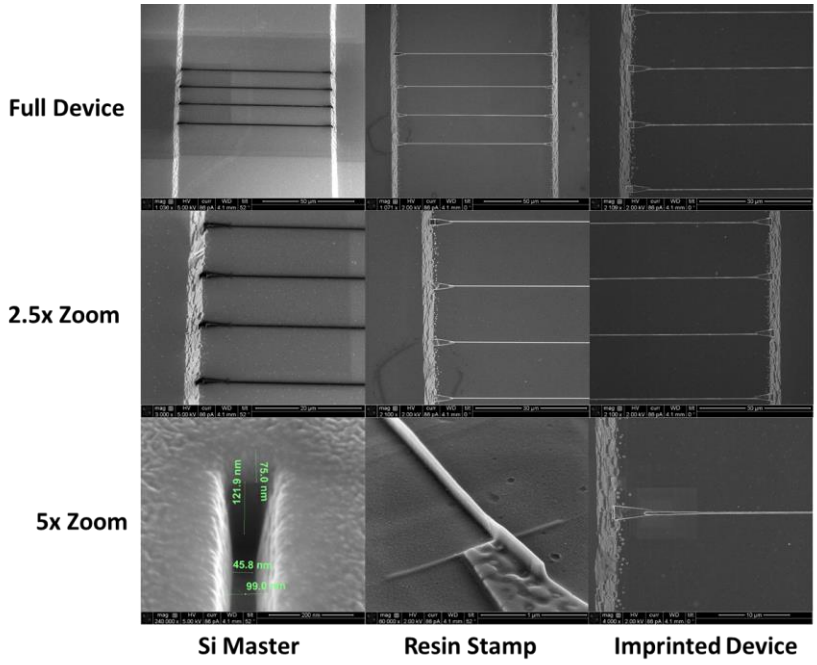

Figure 4–2 SEM images showing the Si master (left panels), Resin stamp (middle panels) and imprinted PMMA device (right panel) used for nanoelectrophoresis experiments.

4.2.5 Imaging System for Nanochannel Electrophoresis

All fluorescence imaging for the nanoelectrophoresis were performed using an Axiovert 35 inverted micro-scope (Carl Zeiss AG, Oberkochen, Germany) equipped with a 100× oil immersion objective (NA 1.3) (Figure 2–1). A Gaussian laser beam (Nd: VYAG; λex = 532 nm; P = 0.01-5 W; 2.2 mm beam diameter) was expanded with a 10X Keplerian beam expander to completely back-fill the objective and the wings were knocked out with an iris to ensure uniform laser intensity in the field-of-view. The beam was focused using a lens into the back of a microscope objective to allow irradiation of the entire field of view and passed through a 532 nm laser line filter and dichroic filter. The emission signal was collected by the objective, passed through a dichroic filter, was spectrally selected using longpass and bandpass filters, and was imaged onto an iXon3 897 EMCCD camera (Andor Technology Ltd., Belfast, United Kingdom) controlled by Metamorph software.

4.2.6 Nanochannel Electrophoresis of Atto 532 labeled dNMPs

Assembled nanochannel devices were activated using 21.85 mW/cm^2 UV/O_3 through the 100 µm cover plate for 15 min. After activation, chips were primed using 50% MeOH for 5 min. Chips were then drained of the MeOH and filled with 50 mM TB buffer at the desired pH and allowed to equilibrate for 10 min. 200 nM samples of ATTO 532-dNMPs were prepared in the BGE and introduction of the sample was done by removing the priming BGE from the reservoir on chip and filled with the analyte solution. BGE was then removed from the opposite reservoir to allow for pressure injection of dye labeled dNMP solution into the access microchannel. Once the microchannel was filled, all reservoirs were filled with equal volumes of the BGE. Electrodes were place in opposite access reservoirs to allow for a drive voltage to drop along the nanochannels. A square wave of varying voltages (V_{pp}) was applied using an ATTEN ATF20B Function waveform generator with a period of 5 s to allow for complete injection and ejection of the dye-labeled dNMP from the nanochannel. Injection and ejection events

were recorded for 5,000 frames allowing for multiple events to be analyzed. Figure 4–3 shows the experimental set up with data analysis.

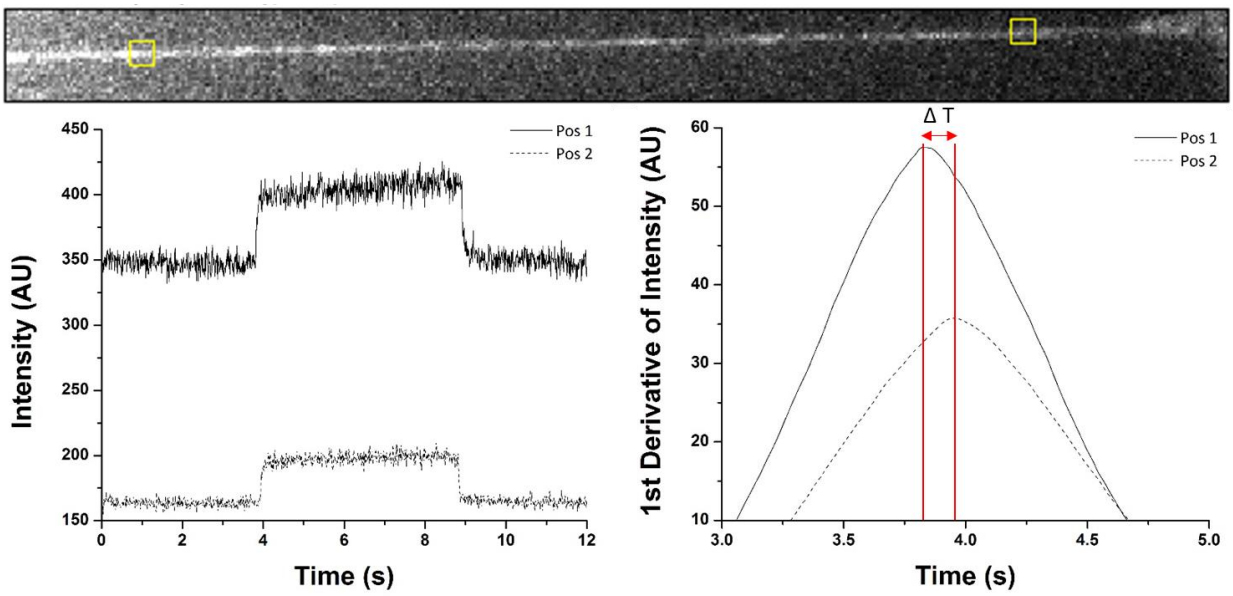

Figure 4–3 Depiction of how the nanoelectrophoresis experiment and data analysis were performed. The top panel shows the fluorescently labeled dNMP being electrokinetically injected in to a nanochannel with the yellow boxes indicating detection area 1 and 2. The bottom left panel shows the fluorescent intensity profile of one injection event at position 1 and 2. The bottom right panel shows the first derivative of the intensity profile to determine the time required for each dNMP to migrate from position 1 to position 2.

4.2.7 Nanochannel Electrophoresis Data Analysis

FiJi software was used to analyze nanoelectrophoresis data. Videos of injection and ejection events were imported in to FiJi and 1 μm^2 "detection windows" were placed at the entrance and exit of the nanochannel. In the FiJi software, these detection windows record the fluorescence intensity over time. This data was exported in to Origin 8.5 and the first derivative was taken of each data set to show two peaks indicating the time at which the maximum intensity was reached at both the entrance and exit of the nanochannel. The time between peak 1 and peak 2 is the ΔT for each dNMP and the electrophoretic mobility can be determined from this value.

4.3 Results and Discussion

Electrophoresis allows for the separation of molecules through differences in their electrophoretic mobility in an electric field. Conventional CE has been employed for the separation of numerous molecules, however, in cases where differences in the electrophoretic mobilities of the analytes do not permit separation, buffer additives must be used to achieve the desired resolution. Literature has shown that nanoelectrophoresis may allow for unique separation mechanisms not possible with conventional CZE. We aimed to explore the use of nanoelectrophoresis for the separation of dNMPs and understand scaling effects associated with these separations. To accomplish this goal, CZE, MEKC, and nanoelectrophoresis was investigated to understand the optimal parameters for the separation of dNMPs. Results from these studies will provide a valuable understanding as to the potential of time-of-flight SMS using nanoscale electrophoresis.

4.3.1 CZE of dNMPs

Changing the pH, thus changing the charge of an analyte as well as the surface charge density of the column wall, is often employed to enhance resolution within CZE experiments. The electrophoretic mobility of a molecule, as described in Equation 4.1, is dependent on the charge to size ratio, thus changing the charge of an analyte of interest can result in a change in the mobility. The charge of a dNMP is complex because there are several ionizable groups with different pK_as (see Figure 4–4).[273] The charge is based on the phosphate group and the partial charge from the nucleotide base and the deoxyribose sugar. The ionization of the only phosphate on dNMPs occurs at such a low pH that all dNMPs are considered to be negatively charged over the pH range of 2-12. The charge on the purine or pyrimidine base that is determined by the pH of the buffer is primarily responsible for the selectivity of the separation between the dNMPs that have the same number of phosphate groups.[273] Guanine and thymine have different pK_as with guanine having a pK_a of 9.24 and thymine having a pK_a pf 10.[273] Due to the potential to enhance resolution with varying pHs, we explored the separation of all 4 dNMPs in a 1

mM Mg^{2+}, 89 mM TBE BGE at varying pHs as can be seen in Figure 4–5a. The dNMPs migrated from anode to cathode in spite of their anionic nature at all pH values due to the high magnitude of the electroosmotic flow, EOF, in the fused silica capillary (EOF = 7.2 x 10^{-4} pH 9.3). We see that, regardless of the pH, a complete separation was not

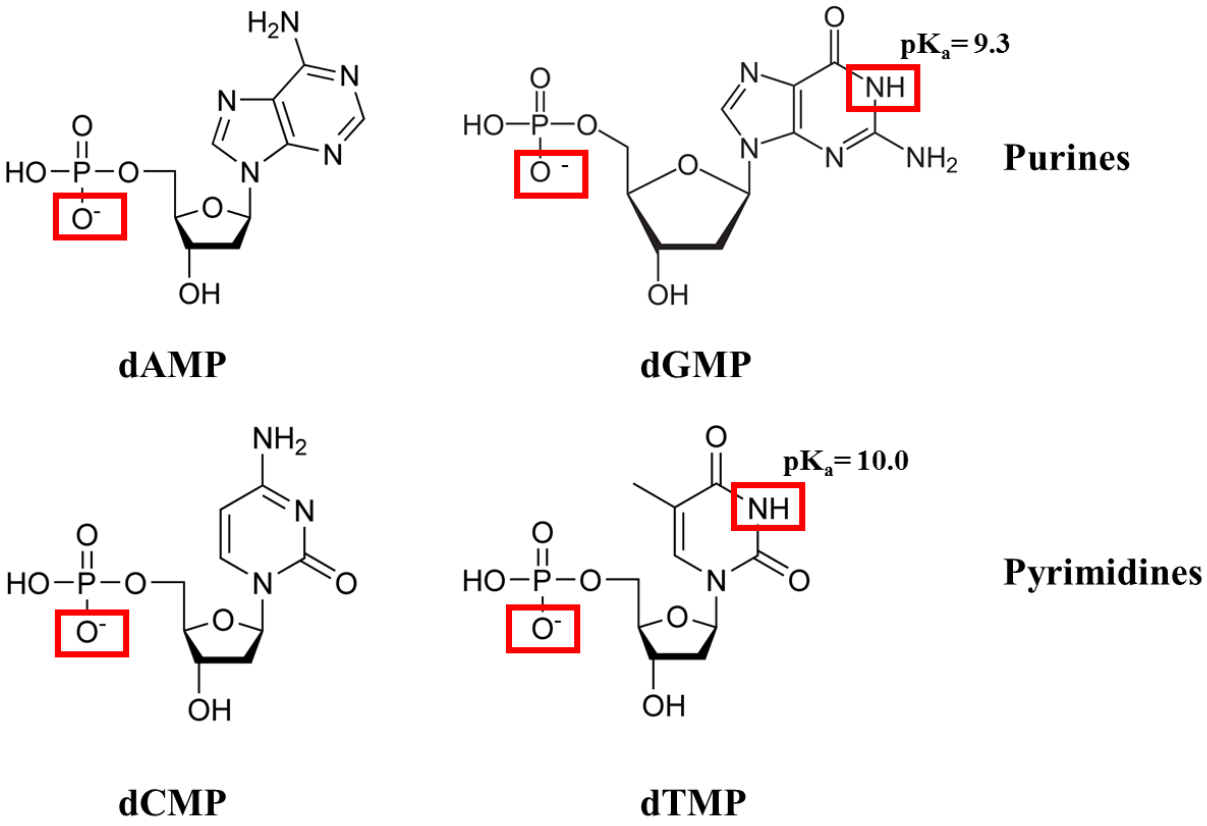

Figure 4–4 Structure of nucleobases of DNA. The red squares indicate the ionizable groups investigated in CZE experiments and their respective pKa values. Phosphate groups ionize above pH below 1.

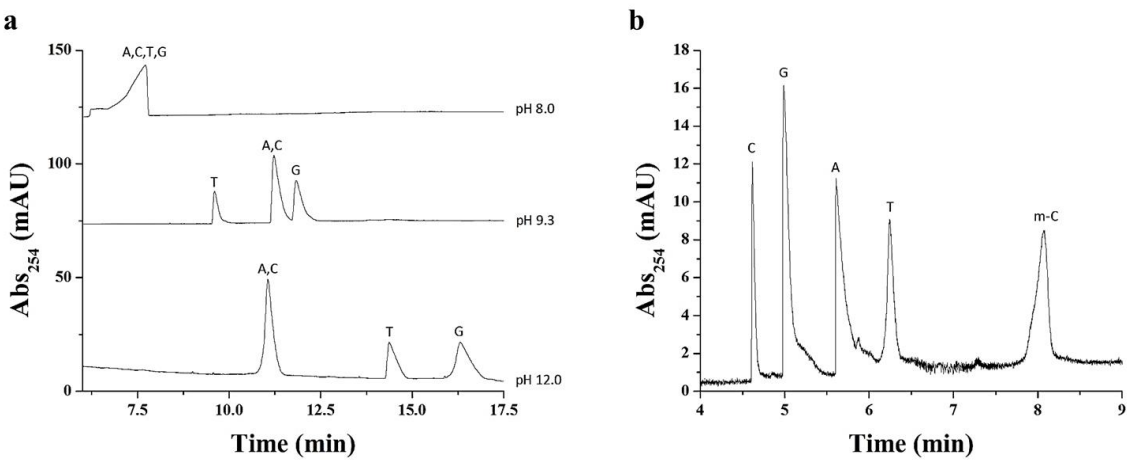

Figure 4–5 a) Capillary zone electrophoresis of dAMP, dCMP, dTMP and dGMP at varying pH values. The electrophoresis was performed using the following conditions: Voltage 25 kV (387 V/cm), BGE 1 mM Mg2+ in 89 mM TBE. b) MEKC separation of dCMP, dGMP, dAMP, dTMP, mdCMP. The electrophoresis used the following conditions: 75 mM AMP, 20 mM NaCl 6 mM CTAB and pH = 8.5. The applied voltage was 20 kV (310 V/cm). Both separations were performed in a silica capillary that possessed an ID = 50 µm, total length = 64.5 cm, effective length = 56 cm, pressure injection at 90 mbar* s, with UV detection at 254 nm. In this case, the nucleotides were not labeled with a chromophore.

obtained between dAMP and dCMP, which has been observed elsewhere and is most likely due to the lack of an pH-sensitive ionizable group on these nucleobases.[287] At pH = 9.3, dGMP showed the highest electrophoretic mobility and thus, migrated the slowest (*i.e.*, dGMP had the lowest apparent mobility). At this pH, guanine's electrophoretic mobility was -3.72 x 10^{-4} $cm^2/V*s$ while thymine had an electrophoretic mobility of -3.22 x 10^{-4} $cm^2/V*s$. When the pH was changed to 12, well above the pKa for both dTMP and dGMP, the electrophoretic mobility increased for both molecules. Guanine's electrophoretic mobility at pH = 12 was -4.55 x 10^{-4} $cm^2/V*s$ and thymine's was -4.35 x 10^{-4} $cm^2/V*s$.

Table 4-1 presents the theoretical plates for the CZE separation performed at both pH values for the dNMPs. Thymine showed the greater efficiency (N) at both pH values. This is to be expected according to the van Deemter equation;

$$\boldsymbol{H = A + \frac{B}{\mu} + C\mu} \qquad (4.4)$$

which shows the factors that contribute to plate height (H) as a function of the longitudinal velocity (**μ**) with **A** being dispersion due to multiple paths, **B** being dispersion due to longitudinal diffusion, **C** being dispersion due to the resistance to mass transfer. Because CZE experiments were performed in open tubular capillaries without partitioning to a stationary phase, the van Deemter equation simplifies to $H = \frac{B}{\mu}$ indicating that band broadening is dominated by longitudinal diffusion. Because thymine elutes before guanine, it has less time for longitudinal spreading resulting from diffusion. Furthermore, the efficiency of the separation decreases for the dNMPs at higher pH values due to increased separation time, and thus, increased diffusional spreading. At all of the pH values investigated, we were unable to separate adenine from cytosine using CZE which has been reported in the literature due to the lack of an ionizable group and insignificant difference in size of these two molecules.[273,282]

	$\Delta G_{tr(w\rightarrow chx)}$ Kcal mol^{-1*}	**CZE Theoretical Plates (m^{-1}) pH 9.3**	**CZE Theoretical Plates (m^{-1}) pH 12.0**	**MEKC Theoretical Plates (m^{-1}) pH9.0**	**Nucleotide Pair**	**MEKC Resolution**
dAMP	2.82	N/A	N/A	113,000	dCMP→ dGMP	6.2
dCMP	6.03	N/A	N/A	443,000	dGMP→ dAMP	7.2
dTMP	2.18	146,000	91,700	109,000	dAMP→ dTMP	6.6
dGMP	6.67	92,900	35,100	104,000	dTMP→ mdCMP	13.0
mdCMP	N/A	N/A	N/A	58,000		

Table 4-1 Theoretical plates calculated from Figure 4–5 for each dNMP. Theoretical plates were calculated using $N= 16(t/w)^2$. Resolution between dNMPs pairs from Figure 4–5b were calculated using $R = \Delta t/w_{avg}$ where Δt is the difference in the migration time for each peak pair and w_{avg} is the average full width of the two peaks.

* ΔG values cited from Shih et al. showing hydrophobicity of nucleobase butyl derivatives

4.3.2 MEKC of dNMPs

It is known that separation of the dNMPs is possible with the addition of a surfactant to the BGE, which generates a separation mechanism known as micellar electrokinetic chromatography (MEKC).[105,282] In addition, smaller development times for the dNMPs could be realized by reversal of the EOF, resulting in negatively charged analytes migrating faster. Reversal of the EOF was achieved by the addition of a cationic surfactant, cetyltrimethylammonium bromide (CTAB), to the BGE serving as a dynamic modifier of the capillary inner surface. We performed separations of all four dNMPs as well as methylated dCMP with a run buffer containing 75 mM 2-amino-2-methyl-1-propanol (AMP), 20 mM NaCl and 6 mM CTAB as can be seen in Figure 4–5b. At pH = 8.5, where all the dNMPs have the same net charge, the dNMPs and the methylated dCMP were separated with the migration order tracking closely the hydrophobicity of the dNMPs;[224,288,289] baseline resolution for all 5 dNMPs was observed. As seen in Table 4-1, we observed resolution values ranging from 6.0-13.0 for the MEKC separation of all 5 dNMPs with theoretical plates up to 443,000 m^{-1}.

4.3.3 Nanoelectrophoresis of ATTO 532 Dye

To initiate the nanoelectrophoresis study, fluorescence tracking of the dye, ATTO 532, was undertaken. Because we intended to use the ATTO 532 dye as a reporter for tracking the electrophoretic motion of the dNMPs through the polymer nanocolumns, we sought to understand the mobility of this dye alone. Nanoelectrophoresis experiments of the dye at varying BGE concentrations were performed (Figure 4–6), because changing the BGE concentration modulates the EDL thickness and can introduce different EOF profiles under certain conditions. As can be seen in Table 4-2, with a BGE concentration of 44.5 mM, the Debye length (λ_d) was 1.25 nm and at a BGE concentration of 0.45 mM λ_d was 12.5 nm. To determine the extent of EDL overlap, κa was used as an operational metric, where a is the channel radius and κ is the inverse of the λ_d (Equation 4.5);

$$\kappa = \sqrt{\frac{8\pi n e^2}{\varepsilon K T}} \quad (4.5)$$

where n is the number of electrons, e is the elementary charge of an election, ε is the dielectric constant, K is Boltzmann's constant and T is temperature. If κa >> 1, there is negligible EDL overlap and thus, the EOF profile should be classic plug like; however for cases where κa ≈ 1, significant EDL overlap occurs and the EOF is predicted to resemble Poiseuille-like flow.[4] For a buffer concentration of 44.5 mM and λ_d of 1.25 nm with the nanochannels possessing a width and height of ~70 nm, the κa value was 44 indicating classic plug-like flow. For a buffer concertation of 0.45 mM and λ_d = 12.5 nm, the κa value was 4.41indicating partial EDL overlap and thus, more parabolic-like flow for the EOF (.

As can be seen in Figure 4–6 for both BGE conditions, a field-dependent apparent mobility of the dye was observed until a critical electric field strength was reached, with this critical electric field depending on the BGE concentration. Conventional CZE theory would predict that the electrophoretic mobility of an analyte is independent of field strength;[105] however, field strength dependency on the mobility has been reported for nanoelectrophoresis arising from stick-slip motion.[71,166] Stick-slip motion typically occurs at lower electric field strengths, where the mobility of the molecular entity becomes a function of the electric field strength. However, at a "critical" electric field strength, the mobility remains constant as anticipated based on classical theory for CZE. As can be seen in Figure 4–6, this critical field strength was dependent on the BGE concentration. For a BGE concentration of 44.5 mM, the critical field strength for the ATTO 532 dye was 479 V/cm, while for a BGE concentration of 0.45 mM, this critical field strength was 273 V/cm. Beyond the critical field strength, the apparent mobility of ATTO 532 was ~5.0 x 10^{-5} cm^2 / V s for both BGE concentrations.

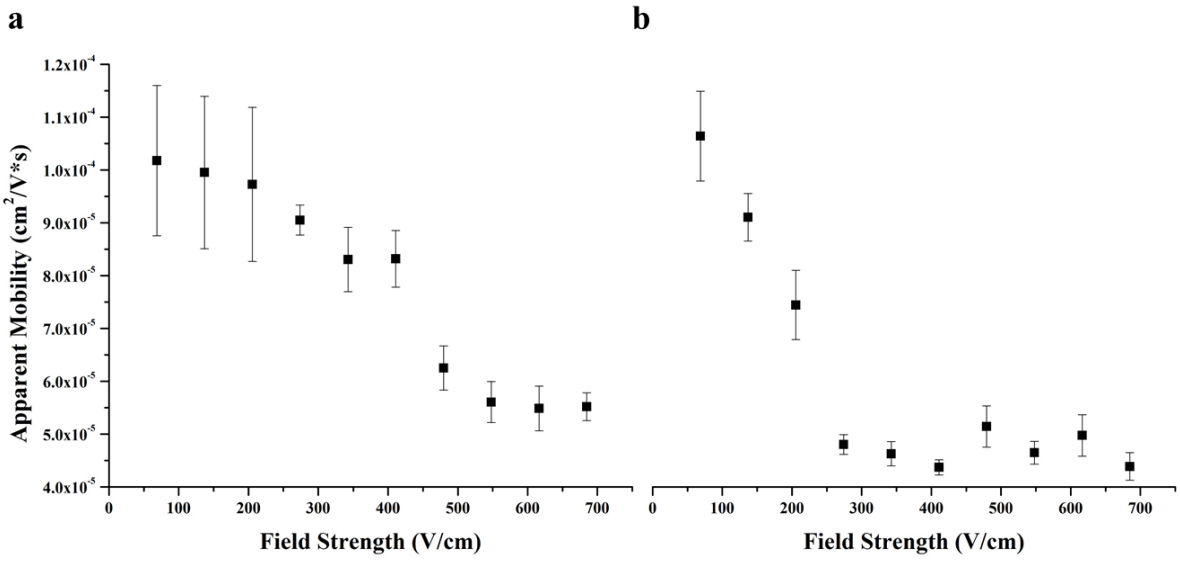

Figure 4–6 Apparent mobility versus field strength for Atto532 dye injected into a nanoscale electrophoresis column that was 70 x 70 nm and consisted of nanochannels that were fabricated in PMMA and possessed a COC cover plate. The nanoscale electrophoresis used two different BGEs consisting of; a) 44.5 mM TB with a pH 8.3 (λd = 1.25 nm); and b) 0.45 mM TB pH 8.3 (λd = 12.5 nm). Errors bars show ± standard deviation of the apparent mobility.

Buffer Concentration (mM)	Debye Length (nm)	Ka
44.5	1.25	44.0
0.45	12.5	4.41

Table 4-2 Debye length and κa values for varying buffer concentration used in nanoelectrophoresis experiments. Ka values are based on a nanochannel that is 100 nm x 100 nm.

4.3.4 Nanoelectrophoresis of dNMPs

Differences in the mobility of the individual dye-labeled dNMPs was due to differences in the electrophoretic mobility of the dNMPs because the same dye reporter was appended to all of the dNMPs. Figure 4–7a shows the apparent mobility versus electric field strength for the 4 dNMPs and m-dCMP using a 110 x 110 nm column with a BGE of 44.5 mM TB at pH 8.3. At this pH, all of the dNMPs would have a net charge of -2, due to the addition of the ATTO 532 dye. We did observe a decrease in the apparent mobility when compared to the dye alone as expected due to the increased charge. As seen in Equation 4.6, the apparent mobility is a function of the EOF (μ_{eof}) and the electrophoretic mobility of the molecule (μ_{ep}):

$$\mu_{app} = \mu_{eof} + -\mu_{ep} \tag{4.6}$$

In this case, the electrophoretic mobility is opposite in direction to that of the EOF and an increase in μ_{ep} results in a decrease in the apparent mobility for this particular condition. As can be observed from Figure 3a, there was differences in the apparent mobilities of the 4 dNMPs and the methylated C. As seen, there was a field strength dependence on the apparent mobility for all of the nucleotides, except m-dCMP. As a note, we are assuming that the EOF does not change as a function of the electric field strength and as such, changes in the apparent mobility arise to differences in the electrophoretic mobility of the analyte. Figure 4–7b shows histograms of the migration times for the ATTO 532 labeled dNMPs at 342 V/cm, which was selected because it provided the optimal resolution between the dNMPs. These histograms were fit to a Gaussian function and the resolution and plate numbers for these dNMPs were determined from these Gaussian functions. The migration order, dCMP<dGMP<dTMP<dAMP<dm-CMP followed very closely with the previously reported MEKC separation (see Figure 4–5b).

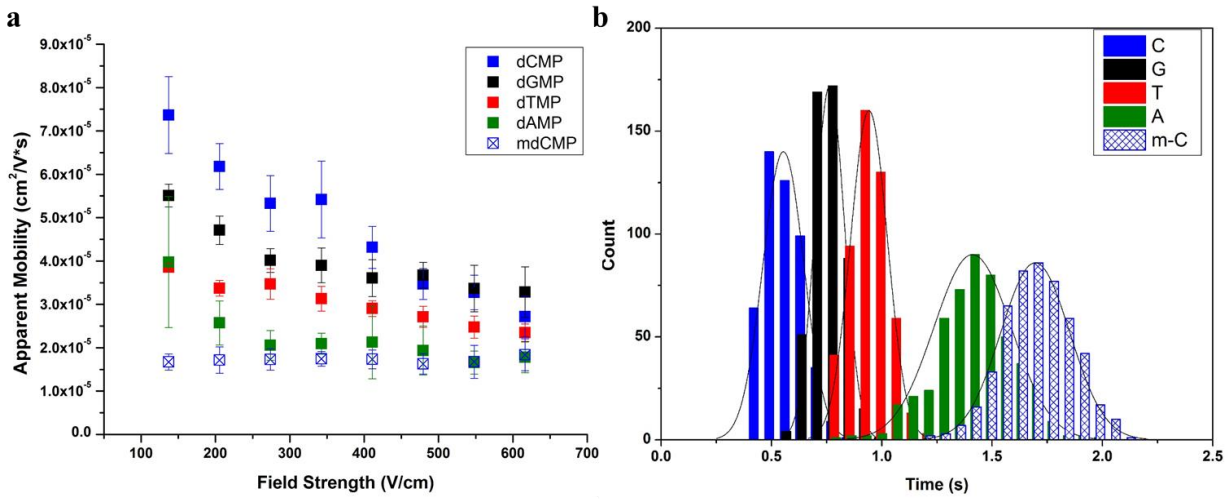

Figure 4–7 a) Apparent mobility versus the electric field strength for Atto532 conjugated to dCMP, dGMP, dTMP, dAMP and mdCMP injected into a nanoscale electrophoresis column that was 100 x 100 nm and used PMMA as the substrate with a COC cover plate. The electrophoresis used a buffer of 44.5 mM TB pH 8.3 (λd = 1.25 nm). b) Histograms of the migration time for the dye-labeled dNMPs with a field strength of 342 V/cm in a 100 µm total length nanochannel. Histograms were fit to Gaussian distributions with each bar representing the migration time (s) of each mononucleotide.

Furthermore, it was in close agreement with molecular dynamic simulations reported for the separation of dNMPs modeled for nanoscale electrophoresis.[224] The nanoelectrophoresis data is in agreement with both the MEKC and MD simulations, thus suggesting that the separations on the nanoscale, under these conditions (pH 8.3, λ_d = 1.25 nm), may depend, at least partially, on hydrophobic differences between the dNMPs. The thin EDL may allow for increased surface interactions, thus more hydrophobic molecules would migrate later, as observed in Figure 4–7**.**

Table 4-3 shows the efficiencies and resolution for this separation. An increase in the number of theoretical plates for the nanoelectrophoresis experiments were observed compared to the CZE and MEKC separations (Table 4-1). As previously discussed, a shorter separation time allowed for less diffusional spreading. The separations reported within the nanochannel were seconds in duration while the CZE and MEKC separation required minutes. With the suspected wall interactions occurring on the nanoscale, we may introduce a "C" term (see van Deemter equation, Equation 4.4) into our

electrophoretic separation. In spite of this additional dispersion term, we still observed theoretical plates (m^{-1}) of 1.87 x 10^6 for dTMP, which was significantly greater than for dTMP (91,700 m^{-1}, see Table 1) when performing CZE, in which no wall interactions were expected.

	Theoretical Plates (m^{-1}) pH 8.3	Theoretical Plates (m^{-1}) pH 9.5	Nucleotide Pair	R @pH 8.3	Base Call Accuracy	Nucleotide Pair	R @ pH 9.5	Base Call Accuracy
dAMP	931,000	10,000,000	dCMP→ dGMP	0.62	76 %	mdCMP→ dTMP	2.0	99 %
dCMP	470,000	1,270,000	dGMP→ dTMP	0.62	76 %	dTMP→ dCMP	0.44	64 %
dTMP	1,870,000	6,520,000	dTMP→ dAMP	0.94	92 %	dCMP→ dAMP	1.2	99 %
dGMP	1,650,000	3,850,000	dAMP→ mdCMP	0.42	62 %	dAMP→ dGMP	2.7	99 %
mdCMP	1,510,000	1,760,000						

Table 4-3 Theoretical plates calculated from Figure 4–7 and Figure 4–9 for each dNMP. Theoretical plates were calculated using $N= 16(t/w)^2$. Resolution between dNMPs pairs from Figure 3b and 4b were calculated using $R = \Delta t/w_{avg}$ where t is the migration time and w_{avg} is the average full width of the two peaks.

Other factors may be considered as well for differences in the efficiency of the plate numbers for micro- versus nanoscale electrophoresis, such as Joule heating.[105,122,290] Heat can only escape from the walls which, in turn, generates a temperature gradient within electrophoresis columns. Taylor dispersion, resulting from Joule heating, contributes to the zonal variance according to Equation 4.7;

$$\sigma^2 = \frac{R_1^2 v_{z,avg}^2 t}{24 D_i} = \frac{R_1^6 E^6 \kappa_e^2 \Omega_t^2 \mu_{app}^2}{1536 D_i k_b^2} t \qquad (4.7)$$

where R_1 is the radius of the capillary, $v_{z,avg}$ is the average linear velocity of the solute across the capillary cross section, t is the migration time, D_i is the diffusion coefficient of the analyte, E is the field strength, κ_e is the electrical conductivity, Ω_t is the temperature coefficient of the electrophoretic mobility defined by $\Omega_t = \frac{\mu(T)-\mu(T_1)}{\mu(T_1)(T-T_1)}$, μ_{app} is the apparent mobility, and k_b is the thermal conductivity of the buffer.

Equation 4.7 shows a strong correlation between zonal variance due to Joule heating and capillary column radius (R_1^6). This dependency results in the optimum field strength for CZE experiments to be only a few hundred V/cm. However, nanoelectrophoresis, with its reduced channel dimensions, allows for the use of much higher field strengths without observing deleterious effects from Joule heating on the separation. The consequence of this also is reduced longitudinal zone spreading due to diffusion as noted in Equation 4.8.[122,290,291]

$$\sigma^2 = 2D_i t = \frac{2D_i L}{\mu_{app} E} \tag{4.8}$$

The plate numbers for electrophoresis can also be deduced from;

$$N = \frac{l^2}{\sigma^2} = \frac{(\mu_{ep} + \mu_{eo})V * l}{2DL} = \frac{(\mu_{ep} + \mu_{eo})V}{2D} \; (for\; L = l) \tag{4.9}$$

where l is the effective column length and L is the total column length. However in cases where $l = L$, the number of theoretical plates is independent of column length. As can be seen here, the plate numbers does depend on the applied voltage, V, and because shorter columns are used for the nanoelectrophoresis (L = 100 µm) compared to CZE (L = 65 cm), smaller applied voltages are used (V = 2.5 V for nanoelectrophoresis; V = 25 KV for CZE). Thus, increasing the voltage should theoretically result in increases in the plate numbers, which was not observed. We attribute this observation to limitations set by the camera used for fluorescence tracking; the camera had a limited frame rate of 97 fps. At the higher applied voltages, which would result in increased molecular velocity, the molecular images become slurred over multiple frames. As such, the optimal applied voltage for our device cannot be determined from the existing system; higher applied voltages may produce better resolution than that observed in Figure 3b.

The use of thermoplastic substrates may also contribute to zonal broadening due to the heterogeneous distribution of surface charged groups following O_2 plasma activation, which has been demonstrated using super-resolution fluorescence microscopy (STORM).[71] The authors showed that control of the dose used for activation can lead to optimal surface charge density with higher surface charge density correlated to lower heterogeneity. Furthermore, utilizing COMSOL simulations to reconstruct fluid flow profiles in nanochannels with a heterogeneous distribution of point charges, the simulations indicated that there were regions of fluid recirculation at point charges leading to both positive and negative velocities; however, irrespective of the plasma dose, the overall EOF magnitude was significantly less than a channel made from glass due to the decreased overall surface charge and thus, any EOF-induced recirculation is a minimal contribution to the overall zonal variance. Their results also indicated that when the electric field strength was high (≥300 V/cm), stick-slip motion was significantly reduced.[71]

Another important metric for the utilization of ToF identification of mononucleotides for SMS is the resolution between the nucleotides, which is directly correlated to the identification accuracy or base call accuracy. With a pH of 8.3, field strength of 342 V/cm and a λ_d of 1.25 nm, the resolutions ranged from 0.42-0.94. As seen Figure 4–8 a resolution of 0.5 has a classification accuracy of 68%, which is based on the degree of overlap in the Gaussian peaks. A resolution of 1.0 has a classification accuracy of 96%. To improve the nanoscale electrophoresis resolution to allow for better classification accuracy as shown in Figure 3b, inspection of equation 4.10 can provide some insight into methods to allow for improvement;[122,291]

$$R = 0.177(\mu_1 - \mu_2)\sqrt{\left\{\frac{V}{(\mu_{avg} + \mu_{EOF})D}\right\}} \qquad (4.10)$$

where μ_1 is the mobility of analyte 1 and μ_2 is the mobility of analyte 2, V is voltage, μ_{avg} is the average mobility of the 2 analytes, μ_{eof} is the electroosmotic mobility and D is the diffusion coefficient. Based on results shown in Figure 4–9b, the pH was modified to improve the selectivity term for the mononucleotides and thus, potentially improve *R* resulting in better classification accuracy.

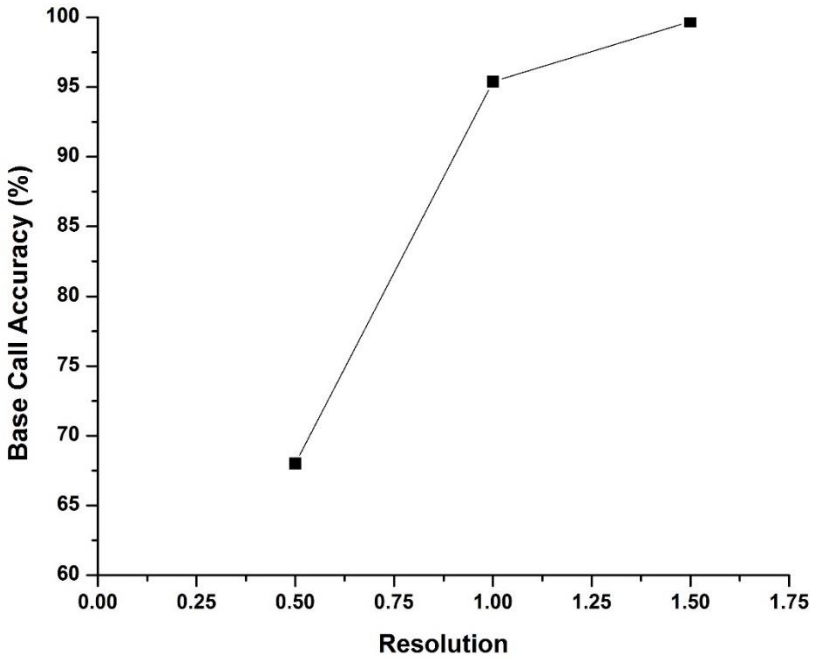

Figure 4–8 Figure showing the base call accuracy vs resolution. This was calculated assuming a Gaussian peak distribution in which the resolution indicated the degree of peak overlap.

4.3.5 Effect of pH on the Nanoelectrophoresis of dNMPs

Figure 4–9 shows the apparent mobility versus field strength for the electrophoretic migration of the dNMPs within a nanochannel with a BGE of 44.5 mM TB at pH 9.5. The migration order at this pH was now m-dCMP < dTMP <dCMP < dAMP < dGMP. The increase in the pH should have a two-fold effect: 1) Increasing the charge on dGMP, thus increasing its mobility; and 2) deprotonating more surface –COOH functional groups on the thermoplastic, thus increasing the magnitude of the EOF. An increase in the μ_{eof} should result in an increase in the apparent mobility observed for the nucleotides as

shown in Equation 4.6, which was observed as well (compare Figures 3 and 4). All nucleotides, except dGMP due to its increased charge, showed a larger apparent mobility at pH 9.5 compared to pH 8.3. Also, the increased pH may account for the change in the migration behavior for mdCMP as well. At this time, we are not certain as to why the mobility of the methylated dCMP was significantly reduced in this case, resulting in a larger apparent mobility given that the EOF is increased in the case of the electrophoretic separation at pH = 8.3.

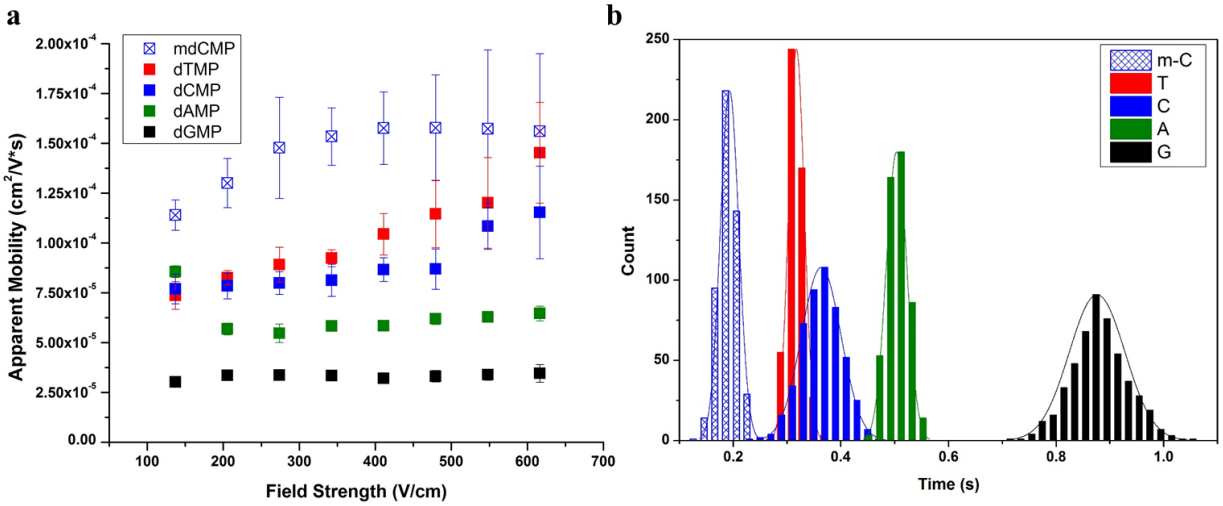

Figure 4–9 a) Apparent mobility versus the electric field strength for Atto532 conjugated to dCMP, dGMP, dTMP, dAMP and mdCMP. The dye-labeled mononucleotides were injected into a 100 x 100 nm nanoscale electrophoresis column that was 100 um in total length. The electrophoresis buffer consisted of 44.5 mM TB pH 9.5 (λd = 1.25 nm). b) Histogram of migration times for the dye labeled dNMPs with a field strength of 342 V/cm in a 100 µm nanochannel. Histograms were fit to Gaussian distributions with each bar representing the migration time (s) of each mononucleotide.

Figure 4–9 b shows a histogram of the migration times for the ATTO 532 labeled dNMPs at 342 V/cm when using a 44.5 mM BGE at pH 9.5. These histograms were fit to Gaussian functions. At this pH value, a decrease in the separation time resulted and also, a larger number of theoretical plates for the nucleotides. Theoretical plates (m^{-1}) at a pH of 9.5 ranged from 1.27 x 10^6 to 10.0 x 10^6.

4.3.6 Effect of EDL Overlap on the Nanoelectrophoresis of dNMPs

In the region of EDL overlap, the flow profile adopts a parabolic-like flow profile.[4,67] On the nanoscale, this parabolic flow profile can be used to enhance electrophoretic separations. On the nanoscale, due to high surface-to-volume ratios, electrostatic forces induced by the charged wall can place a charged particle within a particular stream line allowing for enhanced separations for molecules with different charges or varying size; this is called Transverse Electromigration, TEM.[119,292,293] EDL overlap may also prevent the injection of co-ions in the nanochannel due to concentration polarization effects.[4] To observe how EDL thickness affected the separation of the dye-labeled dNMPs, nanoelectrophoresis of the dNMPs with a BGE of 0.45 mM TB pH 8.3 under varying electric field strengths were undertaken. We did not observe concentration polarization of the dye-labeled nucleotides at this EDL thickness. The overall magnitude of the apparent mobility was higher for the dNMPs when compared to the case of the 44.5 mM BGE, which possessed a thinner EDL. dCMP did show a field strength dependence on its electrophoretic mobility while the other dNMPs did not, which is unexplained at this time.

Furthermore, a decrease in the resolution of the mononucleotides was observed with thicker and partial EDL overlap as compared to the BGE consisting of 44.5 mM and thus, a more compressed double layer. As seen in Figure 4-10b and Table 4-4, the resolution dropped to as low as 0.039 with the highest resolution being 0.44. In addition to the decreased resolution, the efficiency of the separation was reduced as well. Theoretical plates (m^{-1}) ranged from 34,200 to 1,670,000, which was much lower when compared to the thinner EDL results. Thus, EDL overlap resulted in a decrease in the resolution of the dNMPs; careful selection of the BGE molarity and pH will be required for the realization of ToF detection within nanochannels.

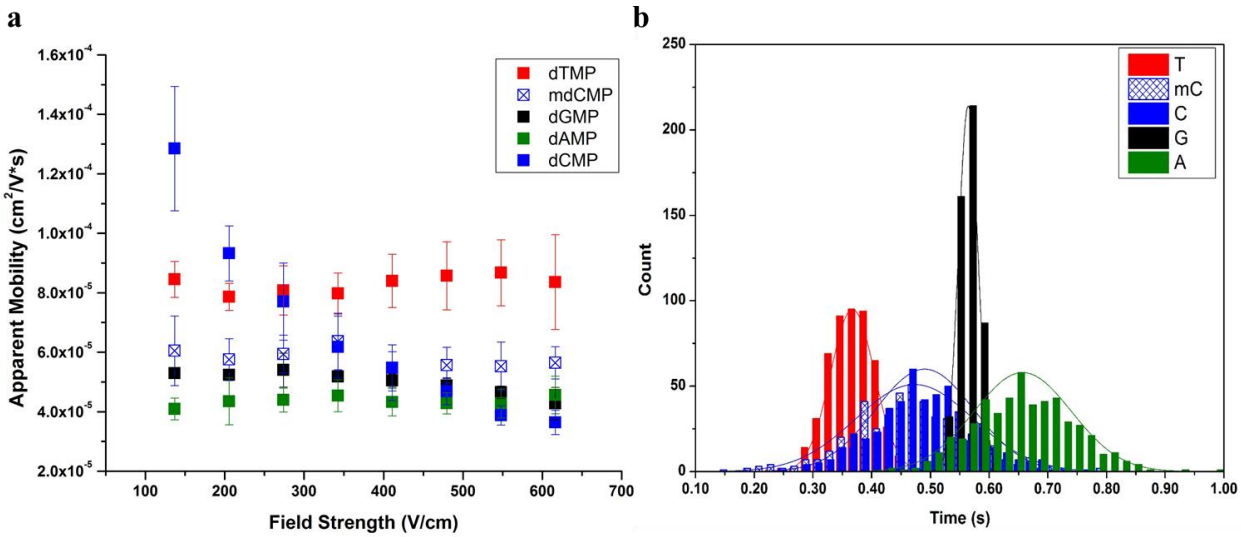

Figure 4–10 a) Apparent mobility versus the electric field strength for Atto532 conjugated to dCMP, dGMP, dTMP, dAMP and mdCMP. The dye-labeled mononucleotides were injected into a 100 x 100 nm nanoscale electrophoresis column that was 100 um in total length. The electrophoresis buffer consisted of .45 mM TB pH 8.3 (λd = 12.5 nm). b) Histogram of migration times for the dye labeled dNMPs with a field strength of 342 V/cm in a 100 µm nanochannel. Histograms were fit to Gaussian distributions with each bar representing the migration time (s) of each mononucleotide.

	Theoretical Plates (M^{-1}) pH 8.3	Nucleotide Pair	R @pH 8.3
dAMP	80,300	dTMP→ mdCMP	0.39
dCMP	45,300	mdCMP→ dCMP	0.039
dTMP	1,440,000	dCMP→ dGMP	0.39
dGMP	1,670,000	dGMP→ dAMP	0.44
mdCMP	34,200		

Table 4-4 Theoretical plates calculated from Figure 4–10 for each dNMP. Theoretical plates were calculated using $N= 16(t/w)^2$. Resolution between dNMPs pairs from Figure 4–10b were calculated using $R = \Delta t/w_{avg}$ where t is the migration time and w_{avg} is the average full width of the two peaks.

4.4 Conclusions

SMS offers advantages over conventional ensemble based sequencing platforms; although, current limitations of existing SMS technologies are preventing the realization of this technology such as poor base call accuracy (typically around 80%).[13,294,295] Our proposed SMS device looks to address these

issues by generating mononucleotides using a processive enzyme from an intact DNA molecule. Identification of the nucleobases would be enabled by molecular-dependent flight times of the dNMPs within nanometer flight tubes; concept termed Time-of-Flight (ToF) identification. This research sought to understand differences in the migration behavior of dNMPs under varying pH, buffer additives, buffer molarity and channel dimensions and how these conditions affected the resolution and ultimately base call accuracy. We determined that nanoscale columns introduces unique nanoscale phenomena that exploit differences in the molecular compositions, although subtle, of the dNMPs. Electrophoretic resolutions ranging from 0.42-0.94 were achieved at pH = 8.3 and with changes in the pH, resolutions to 2.7 were observed when implementing nanoscale electrophoresis; this was not achievable using conventional microscale electrophoresis. Indeed, baseline separation of the 4 dNMPs including the methylated dCMP were possible using nanoelectrophoresis in free solution while the micro-column required MEKC to allow for separation of the mononucleotides. Furthermore, it was determined that buffer concentrations resulting in partial EDL overlap decreased the resolution compared to cases where the EDL was compressed and not significantly overlapped. This result supports the use of ToF detection downstream of λ-exonuclease because this enzyme required high mM solutions to function; thus generating a thin EDL. Ultimately, the use of nanoelectrophoresis could allow for the separation of dNMPs with favorable resolution and the correspondingly high identification accuracy in a SMS strategy.

CHAPTER 5. ONGOING WORK AND FUTURE DIRECTIONS

5.1 Introduction

The future goal of this work to develop an innovative biosensor capable of sequencing biomolecules such as DNA, RNA and proteins in a real-time, rapid and efficient manner. The ability to provide sequence information on complete genomes has implications in areas such as drug discovery, biomarker discovery, diagnostics, preventative medicine and forensics.[13,294,295] Furthermore, the Human Genome Project, completed in 2003, was able to successfully determine the genome sequences of a myriad of organisms, which has facilitated fundamental understandings within biology, medicine and evolution. Beyond determining the sequence of the genome, efforts were set forth to understand gene abnormalities that could be used as biomarkers for in vitro diagnostics. Translating the structure of the genome into information relevant for health and disease is a task pursued by many organizations including the National Human Genome Research Institute (NHGRI).

The final device proposed in this dissertation intends to render primary sequences of nucleic acids so as to recognize base mutations, or identify proteins through peptide sequences. In contrast to current sequencing technologies, our approach aims to determine biopolymer structure through the processive excision of individual monomer units such as nucleotide monophosphates (dNMPs) from a template DNA strand and through the characteristic molecular-dependent migration of these excised units through a polymer nanochannel (Time of Flight (TOF) detection). Our device will utilize a nanosensor chip fabricated in thermoplastics to allow for high fidelity and low-cost production of these devices as well as electrical detection utilizing nanoelectrodes or in plane synthetic nanopores to eliminate the confinements of optical hardware for detection.

Thermoplastics have provided attractive alternatives to glass or silicon due to the materials' diverse range of physiochemical properties, availability of a plethora of fabrication techniques to design prerequisite structures, optical transparency and surface chemistries that can be tailored towards the desired application. The ease of activating thermoplastic surfaces by O_2 plasma and UV/O_3 irradiation makes them attractive for studies related to surface charge effects on the electroosmotic flow (EOF) and transport dynamics of single molecules through nano-confined environments.[296] Additionally, the aforementioned activation protocols allow for the generation of surface-confined carboxylic acid groups, which enables the immobilization of various wall modifiers to change surface charge and the EOF. Using this technology, we envision the generation of further innovative discovery efforts for a broader user community due to the systems' low-cost and simple operation. In addition, highly parallel production modalities will be developed to produce the nanosensors in a cost-effective manner to provide realization of platforms that produce sequencing information at the $1,000 level per genome.

5.2 Background

The aforementioned applications require a rapid, reliable, high throughput and cost-effective sequencing strategy with high data quality (i.e., high base calling accuracy) to realize the full potential of genome information. Several new sequencing strategies have been suggested, such as sequencing-by-synthesis that has significantly increased the throughput and at the same time, reduced the cost of acquiring sequencing data. These technologies include commercial instruments such as those from Illumina. These technologies can sequence one human genome in approximately 1-2 days at a cost of ~$10,000. The technology involves random fragmentation of DNA and ligation of linkers to generate a DNA library. Upon amplification, sequencing is performed as each base is enzymatically incorporated to generate the complementary DNA strand. The limitation of such technologies are the inherent error in DNA polymerase insertion resulting in substitution errors as well as relatively short reads challenging assembly.[295]

Recently, single-molecule sequencing (SMS) has been suggested as an attractive alternative to ensemble-based sequencing because it can eliminate the need for polymerases as well as potentially providing longer read lengths. SMS is accomplished by detecting the four nucleotide molecules comprising the DNA polymer using optical, electrical or magnetic properties.[294] The advantages of SMS are that DNA fragments are not required to be amplified. This removes the time and cost for these amplification processes and the inherent error with polymerases.[260] Furthermore, this approach has many other advantages such as sequencing of large DNA fragments, low sample input requirements, no-labeling and real time readout.

One approach to SMS includes nanopore sequencing. For nanopore technologies, each nucleotide of an intact DNA molecule produces a characteristic modulation of ionic current through the nanopore as the DNA molecule is electrically transported through this pore; the order of these modulations reflects the sequence of bases within the starting DNA molecule.[297] However, resolution is insufficient to resolve single bases due to the intrinsic thickness of the pore.[16,265,298] The size of the nanopore allows ~15 nucleobases to span the pore at one time, which leads to blockade currents due to multiple nucleotides.[265] Furthermore, the speed at which the DNA is translocated through the pore does not resolve single bases due to bandwidth limitations set by the current measuring devices.[297] Synthetic nanopores have recently been employed to circumvent some of these challenges.[266,268,299] In addition, to address the multiple occupancy issue to allow for reading single nucleotides, a covalently attached adaptor can be included into the nature pore structure for improved single base discrimination[300] and the attachment of an exonuclease for sequential cleavage to read each nucleotide base.[301] A challenge with this approach, however, is diffusional misordering.[302] Approaches utilizing nanopore technologies are still limited by issues such as high error rates because nucleotide bases are identified using current blockage events, which shows poor contrast in terms of discriminating nucleotide bases.

Limitations of current SMS technologies prevent high base call accuracy (<0.1% error) required for many sequencing applications. To address these issues, we are developing an innovative SMS strategy that cleaves dsDNAs using a processive enzyme to generate individual mononucleotides. Identification of the bases is enabled by molecular-dependent flight times of dNMPs within nanochannels allowing for a dual detection modality in which the signature time of flight (ToF) and current perturbation can both be used to reliably identify each dNMP.

5.3 Description of Proposed Single Molecule DNA Sequencing Device

As seen in Figure 5–1, the process of DNA sequencing module initiates with the immobilization of enzyme in the nanopillar. To accomplish this task, a clipping enzyme such as λ-exonuclease is tethered to the solid nanopillar support that can processively clip the single nucleotide units from the dsDNA strand. This bioreactor can be activated by the introduction of Mg^{2+} in to the fluidic channel.[272] Before the DNA strand reach the enzyme, its activity is manipulated using an entropic trap, which stores the DNA temporarily. These entropic traps also help DNA to elongate to support the sequencing. The released dNMPs are electro kinetically transported through the flight tube (nanochannel) with the travel time determined by the applied electric field, the length of the flight tube and the number of dNMP: channel wall interactions. As our work has shown, the unique separation conditions afforded by nanoelectrophoresis allows for the signature mobility differences of each dNMP to lead to separation and the identification of one nucleotide versus another.

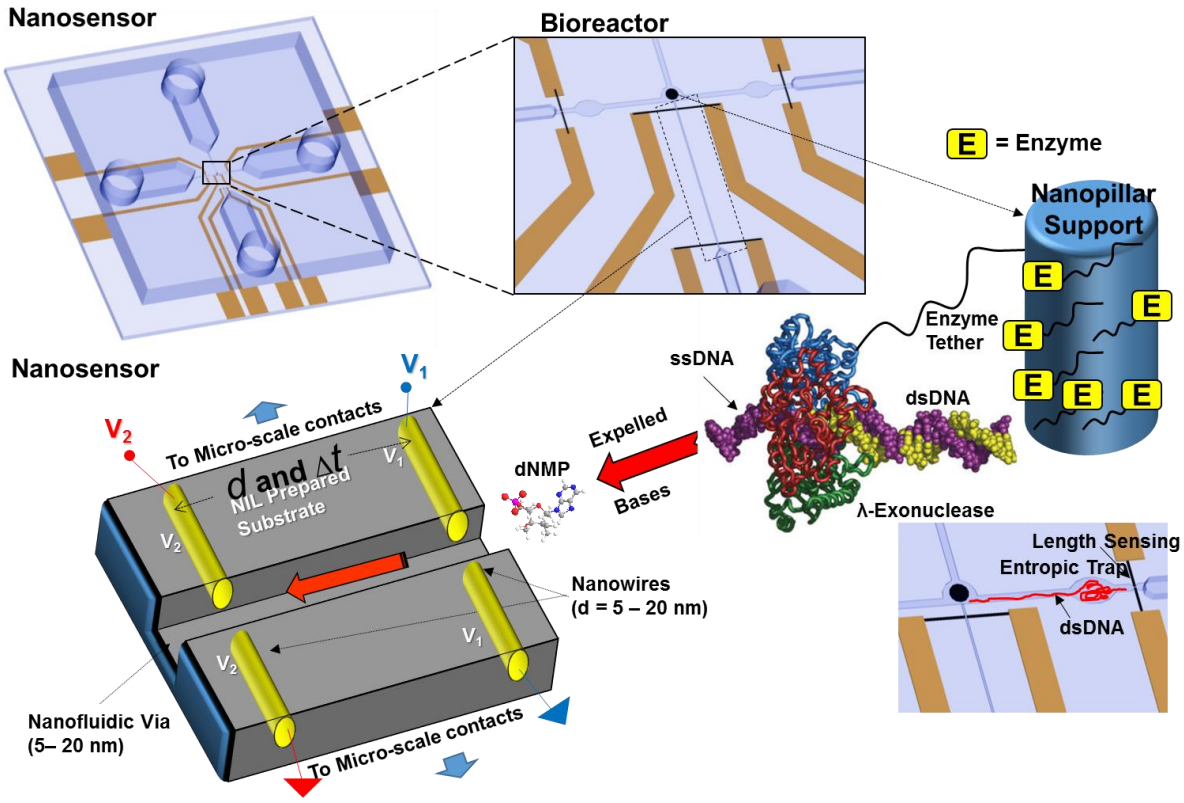

Figure 5–1 Schematic of the nanosensor that accepts dsDNA input molecules and deduces their primary sequence by the sequential clipping of the input dsDNA molecule using an exonuclease enzyme. The single dNMPs generated are moved through a nanochannel that produces a molecular-dependent flight-time used for dNMP identification. The flight-time is measured using a pair of nanoelectrodes poised at the input and output ends of the nanochannel, which is made from the appropriate polymeric material to suit the application need and structured produced via micro- and nano-replication technologies. The nanosensor uses electrical signatures to monitor the input of dsDNA, immobilized exonuclease to complex the dsDNA, entropic traps to stretch the dsDNA and identify the clipped dNMPs using ToF detection through 2-D nanochannels

5.4 Ongoing Developments

5.4.1 Single Molecule dNMP Electrophoresis with optical detection

Current data presented shows the strong potential for the separation of dNMPs within nanochannels due to the unique separations possible on this length scale. However, at this stage, we are performing bulk mobility tracking of dye-labeled dNMPs which does not allow us to truly understand the translocation differences of individual molecules. To accurately determine the ToF of individual dNMPs that have been processively cleaved from dsDNA, we must understand absorption/desorption kinetics, surface interactions and mobility one molecule at a time.

To optically observe the translocation of a single molecule, we will require a fully optimized system with a camera providing a high S/N as well as fast frame rates. Currently, our optical system detects immobile single molecules, as observed in Figure 2–1. However, when the molecule is mobile, the limited photon of a single molecule spreads over several pixels, drastically reducing the S/N. As seen in Figure 5–2, the pixel area covered by a single dye in one exposure time (15 ms), linearly increases with field strength. Thus, we need to increase the S/N over this large pixel area as well as operate at a high enough frame rate to capture the translocation of a single molecule.

Currently, we are using a high powered Nd: VYAG laser which allows for the pumping of single molecules at their highest capacity, ensuring that we are capturing the maximum photons from one dye molecule. At this time, we are utilizing a iXon3 EMCCD camera which does not provide for the highest S/N and frame rate, at this stage. Two options for camera types would be an EMCCD camera or a sCMOS camera. EMCCD cameras are a quantitative digital camera technology that is capable of detecting single photon events whilst maintaining high quantum efficiency, achievable by way of a unique electron multiplying structure built into the sensor. Unlike a conventional CCD, an EMCCD is not limited by the readout noise of the output amplifier, even when operated at high readout speeds. This is achieved by

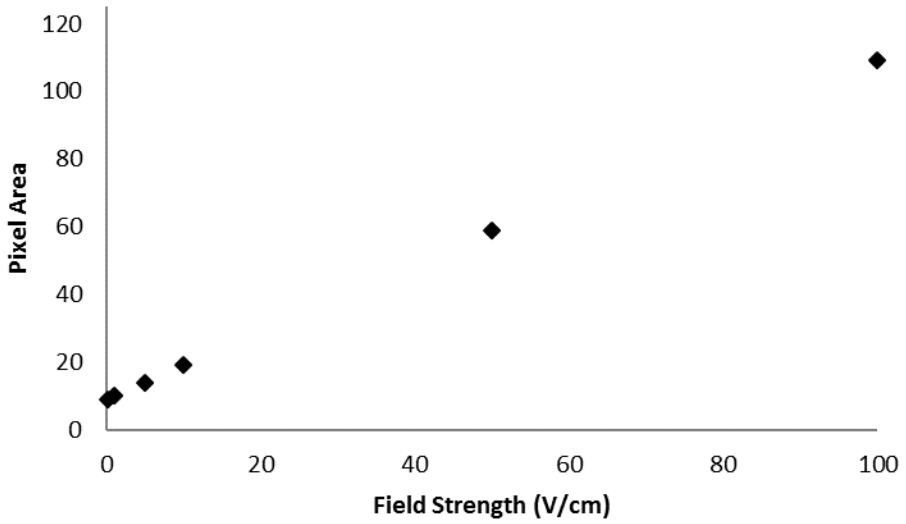

Figure 5–2 Pixel area covered by a single Atto 532 dye molecule vs the Field strength. This plot assumes a field strength of 15 ms and a µapp od 4.0 x 10-5 cm2/V*s. This plot shows the increasing area covered by a single dye molecule as it trans-locates through a nanochannel in an electric field, thus decreasing the SNR.

adding a solid state Electron Multiplying (EM) register to the end of the normal serial register; this register multiplies weak signals before any readout noise is added by the output amplifier, hence rendering the read noise negligible.[303,304] Most wide-field single molecule experiments currently employ Electron-Multiplication Charge Coupled Device (EMCCD) based cameras.

Very recently, scientific imaging sensors based on a Complementary Metal Oxide Semiconductor (CMOS) technology have been introduced with low read noise, high read-out rates, and small pixels, that may significantly improve and simplify single molecule detection systems.[304,305] CMOS sensors convert photoelectrons to voltage on the pixel. These pixel-voltage values are then loaded into column-level amplifiers and analog-to-digital converters. The per-pixel and column-wide gain and digitization can result in more substantial fixed-pattern noise in CMOS sensors[306], but allows for very fast operation. CMOS cameras do not have electron multiplication, so they have higher read noise. However, these sensors have no multiplication noise, a characteristic of EMCCD cameras that reduces the effective quantum yield of the sensor.[304,306]

As can be seen in Figure 5–3 and Figure 5–4 , Saurabh *et al*. compared the S/N ratio for single Cy5 dye molecules, immobilized on glass slides. EMCCD cameras showed much greater S/N compared to sCMOS; however, the S/N ratio for sCMOS was suitable for immobile single molecules. Furthermore, Table X compares key characteristics of cameras used in the study. We see that EMCCD cameras showed a much higher quantum efficiency; however, sCMOS cameras showed much greater frame rates.

For our purpose we need the balance of both high frame rate and high S/N. For this reason, the best compromise may be the Andor iXON Ultra cameras which provide for a unique crop mode, increasing the typically observed slower frame rate when compared to sCMOS cameras. In standard sub-array/ ROI readout mode, each frame still carries the time overhead to readout all pixels to the left and right of the selected area and to vertically shift all pixels above and below the selected area. The charge from these pixels is then dumped before an image is sent from camera to PC. In cropped sensor mode, the number of pixel readout steps outside of that required to readout out the requested sub-array is significantly reduced, resulting in markedly higher frame rates. This may allow EMMCD cameras to approach the fast frame rate observed with sCMOS cameras; while still maintaining the high S/N required for our moving single dye molecules.

5.4.2 Nanopore Devic for the Interrogation of DNA and Abasic Sites

Confinement of DNA in nanochannels or nanopores allows for the potential interrogation of DNA methylation[307-309] or abasic (AP) sites.[310] Elongation of DNA to its full contour length can be achieved through proper selection of nanochannel dimensions and/or the carrier electrolyte solution.[34,127,311,312] Our fluidic biosensor will provide unique capabilities for detecting AP sites as an approach for assessing response to therapy in cancer patients. The integrated system will not only automate the entire sampling

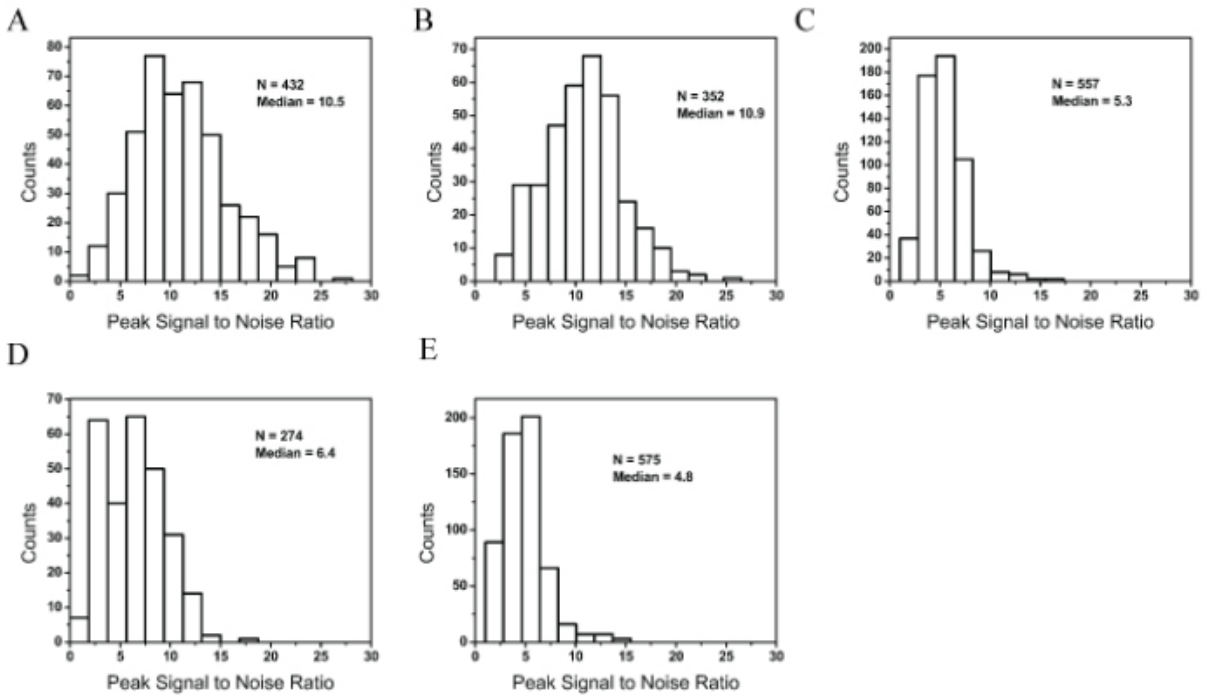

Figure 5–3 Adapted from Saurana et al. Distribution of peak SNR for single Cy5 molecules using A) Evolve 512 EMCCD B) Andor 887 EMCCD C) pco. Edge sCMOS D) Andor Neo sCMOS E) Hamamatsu ORCA Flash 2.8

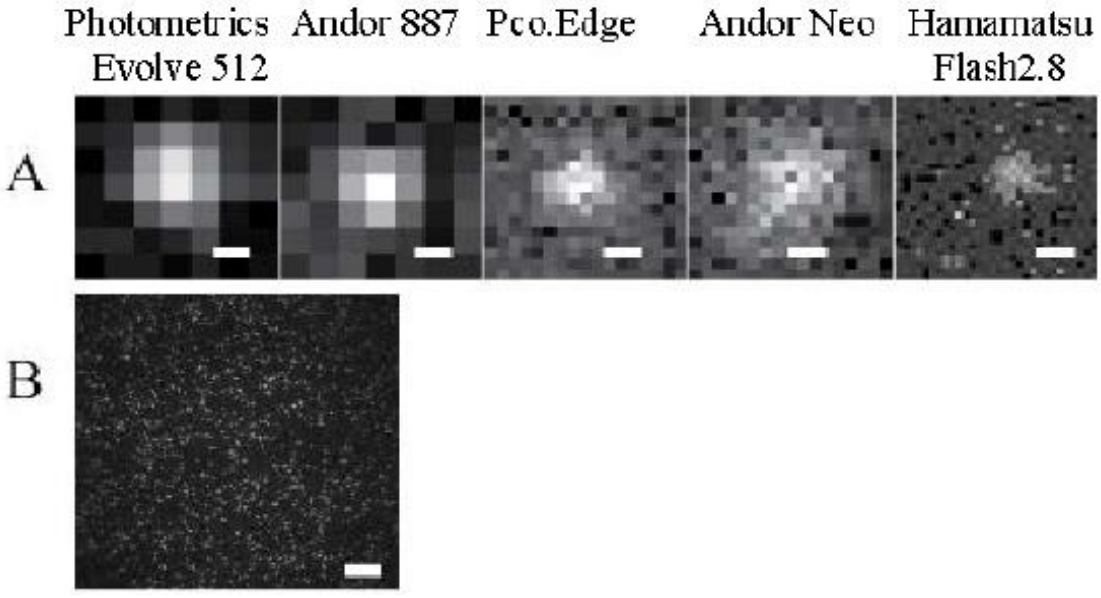

Figure 5–4 Adapted from Saurana et al. A) Single Cy5 molecules imaged using the various sensors (scale bar = 200 µm). B) Single Cy5 molecules sample density imaged using Evolve 512 EMCCD (scale bar = 9 µm).

	Photometrics Evolve 512	Andor 887	Pco. Edge	Andor Neo	Hamamatsu ORCA Flash 2.8
Pixel Size (μm)	16	16	6.5	6.5	3.63
Measured Read noise (e^-/pixel)	0.02*	0.20*	0.78	0.80¥	0.65§
Frame Rate (Full Frame)	33.7	35	100	100	45
Q.E. $_{660}$§§	95%	90%	55%	54%	34%

Table 5-1 Key Characteristics for cameras used in Saurana et al. paper. *Measured read noise with electron multiplication ¥ Measured for pre-amplification gain value of 4 § Measured for gain value of 255 §§ Quantum Efficiency at 660 nm

processing pipeline, but also reduce assay cost and increase throughput. We propose a device design capable of measuring the unique electric signatures of dsDNA and streptavidin labeled AP sites to accomplish the aforementioned assay for DNA damage. Figure 5–5 shows COMSOL simulations for a nanofluidic device design with two nanopores. When dsDNA with abasic sites passes through the nanopore it produces a signal at each pore as the molecule translocates through the nanopores. Furthermore, the elongated DNA will have a signature current trace indicative of the length of the molecule. The perturbation in the electric current due to the streptavidin labeled AP site will be indicative of DNA damage and can be mapped to positions within the DNA. Currently, we are fabricating devices to achieve nanopore dimensions less than 50 nm x 50 nm to allow for AP site detection.

5.5 Future Work

5.5.1 Label Free dNMPs ToF Detection

As previously discussed, we aim to sequence dsDNA through the ToF detection of unlabeled dNMPs. This would allow for a true understanding of the mobility of the native dNMPs since the addition of the Atto 532 may dominant translocation. We must develop a nanosensor for single molecule detection

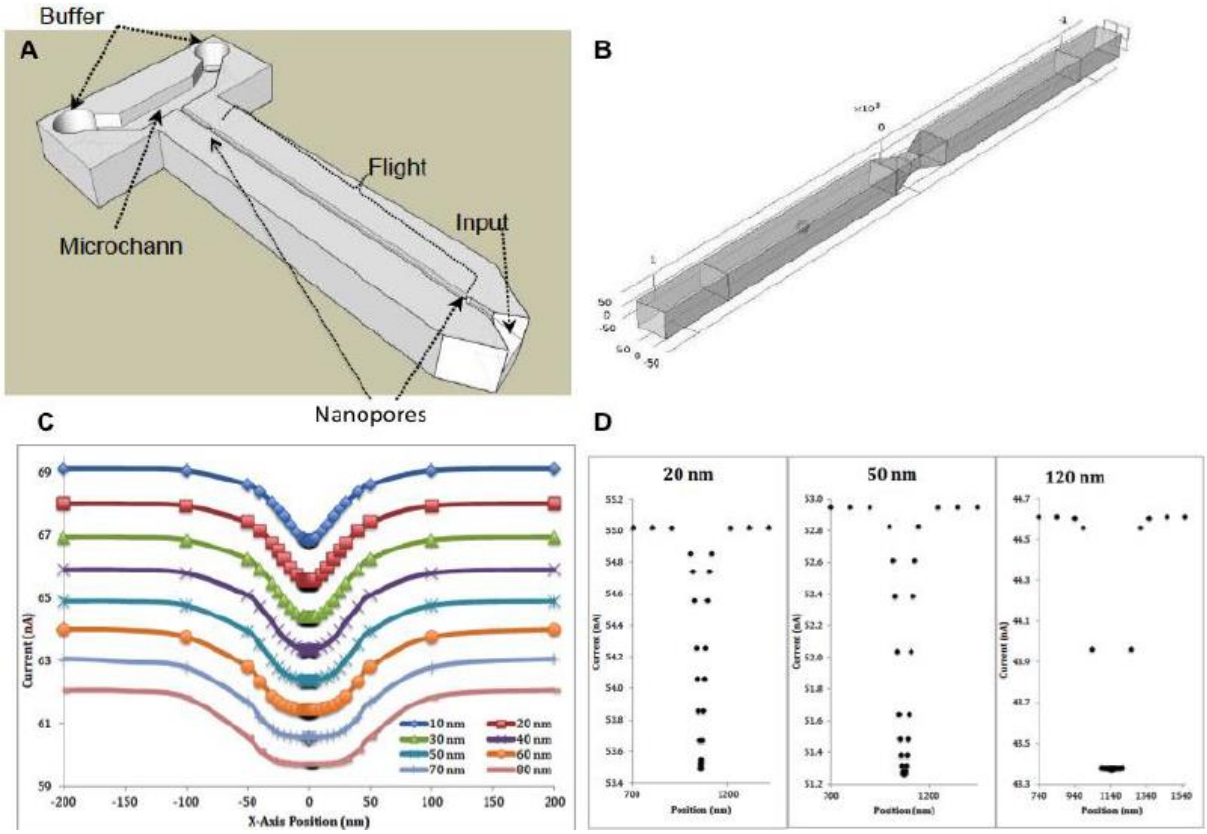

Figure 5–5 6 A) Computer assisted design image of the basic sensor geometry with important structures labeled B) Model for nanopore length simulations in which finer meshes were used to further understand the behavior of the particles and their signals as they passed through the pore. C) Simulation (COMSOL) results showing the effects of pore length on the current response generated. A pore with a cross section of 50 nm × 50 nm was varied in length from 10 nm to 80 nm. For each length a polystyrene bead with a diameter of 40 nm was stepped through positions inside of the pore, the resultant drop in current was recorded. D) Blockage current traces for simulations with 20, 50, ad 120 nm detection pore lengths. The 20 nm pore recorded a current change of 1.52 nA, the 50 nm pore recorded 1.67 nA, and the 120 nm pore recorded 1.23 nA

of these dNMPs and to accomplish this we my employ transverse nanoelectrodes or in plane, solid-state nanopores. Previous work has shown the successful fabrication of a nanosensor in quartz with a nanofluidic channels containing two pairs of transverse Au nanoelectrodes (50 nm^2) poised at the input and output of the nanochannel. This current device is capable of measuring dsDNA; however, preliminary theoretical computations, shown in Figure 5–6, show that nanoelectrodes must be < 10 nm to provide the required SNR for single molecule detection. Furthermore, the gap size between the electrodes will need to be < 3 nm. This may prove to be quite difficult thus alternate methods for single molecule electrical detection will be pursued as well.

Specifically, the use of the previously described solid state, in-plane nanopores may provide the required SNR for single molecule detection and may be easier to fabricate. Harms *et al*. measured the electrophoretic mobilities and particle sizes of individual Hepatitis B Virus (HBV) capsids in nanofluidic channels with two nanopores in series fabricated on glass substrates. The nanopores used for those experiments were 45 nm x 45 nm x 400 nm (w x h x l). Resistive pulse sensing experiments were performed on various HBV capsids with dimensions 32-35 nm in size. This literature provides a guide for the expected size of our nanopores for the detection of single dNMPs. Currently we have fabricated nanopore devices with depths of 7-17 nm and widths of 13-25 nm as seen in Figure 5–7. We will continue to develop new fabrication approaches to ensure the desired SNR is achieved.

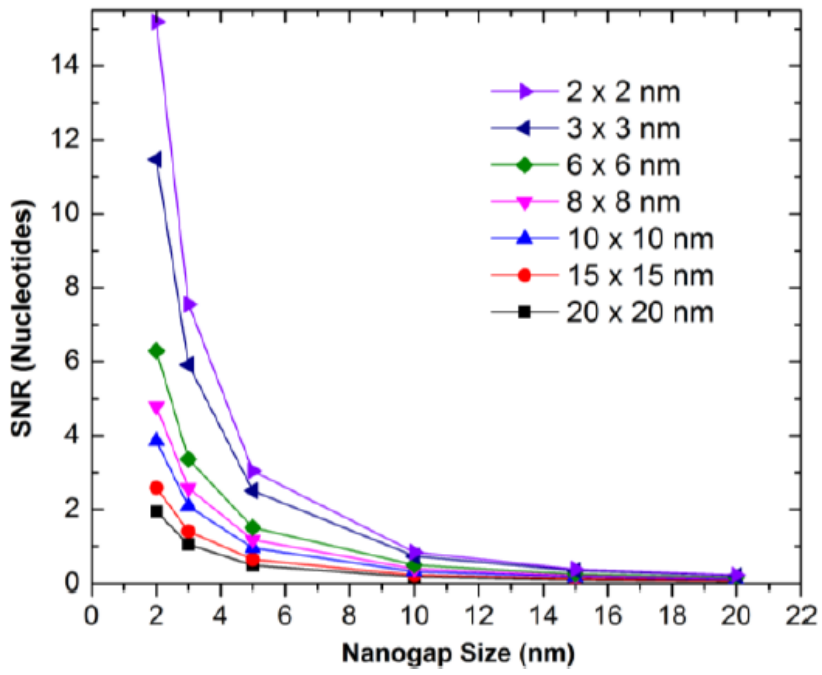

Figure 5–6. Variation between the electrical signal-to-noise (SNR) ratio and the nanogap size for different nanoelectrode areas for single mononucleotide units at 500 mV bias. As the nanoelectrode area reduces, there is a reduction in the detection volume and a corresponding increase in the SNR.

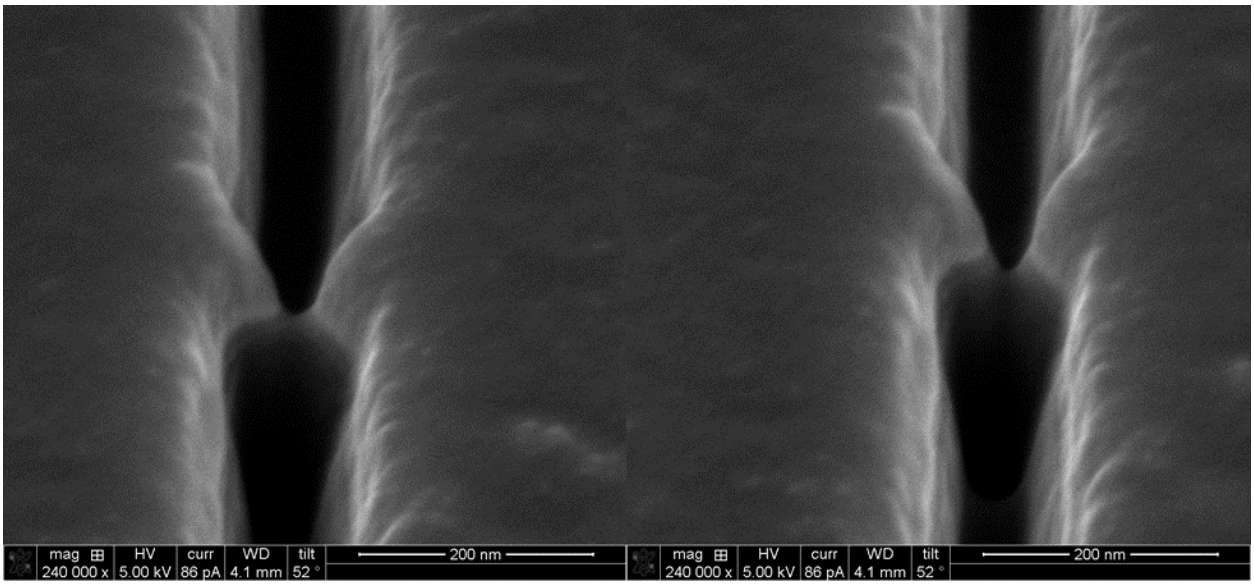

Figure 5–7. SEM images showing FIB milled nanopores within Si with a Cr layer on top. The dimensions of the nanopore are 23 nm x 7 nm (w x d) (left panel) and 28 nm x 18 nm (w x d) (right panel).

REFERENCES

(1) Kim, S. J.; Wang, Y.-C.; Lee, J. H.; Jang, H.; Han, J. *Physical Review Letters* **2007**, *99*, 044501.

(2) Anand, R. K.; Sheridan, E.; Knust, K. N.; Crooks, R. M. *Analytical Chemistry* **2011**, *83*, 2351-2358.

(3) Mani, A.; Zangle, T. A.; Santiago, J. G. *Langmuir* **2009**, *25*, 3898-3908.

(4) Piruska, A.; Gong, M.; Sweedler, J. V.; Bohn, P. W. *Chemical Society Reviews* **2010**, *39*, 1060-1072.

(5) Zangle, T. A.; Mani, A.; Santiago, J. G. *Chemical Society Reviews* **2010**, *39*, 1014-1035.

(6) Kalman, E. B.; Vlassiouk, I.; Siwy, Z. S. *Advanced Materials* **2008**, *20*, 293-297.

(7) Schoch, R. B.; Han, J.; Renaud, P. *Reviews of Modern Physics* **2008**, *80*, 839-883.

(8) van Honschoten, J. W.; Brunets, N.; Tas, N. R. *Chemical Society Reviews* **2010**, *39*, 1096-1114.

(9) Wang, Y.-C.; Stevens, A. L.; Han, J. *Analytical Chemistry* **2005**, *77*, 4293-4299.

(10) Kim, S. J.; Li, L. D.; Han, J. *Langmuir* **2009**, *25*, 7759-7765.

(11) Pu, Q.; Yun, J.; Temkin, H.; Liu, S. *Nano Letters* **2004**, *4*, 1099-1103.

(12) Meller, A.; Nivon, L.; Brandin, E.; Golovchenko, J.; Branton, D. *Proceedings of the National Academy of Sciences of the United States of America* **2000**, *97*, 1079-1084.

(13) Branton, D.; Deamer, D. W.; Marziali, A.; Bayley, H.; Benner, S. A.; Butler, T.; Di Ventra, M.; Garaj, S.; Hibbs, A.; Huang, X.; Jovanovich, S. B.; Krstic, P. S.; Lindsay, S.; Ling, X. S.; Mastrangelo, C. H.; Meller, A.; Oliver, J. S.; Pershin, Y. V.; Ramsey, J. M.; Riehn, R.; Soni, G. V.; Tabard-Cossa, V.; Wanunu, M.; Wiggin, M.; Schloss, J. A. *Nat Biotech* **2008**, *26*, 1146-1153.

(14) Wanunu, M.; Morrison, W.; Rabin, Y.; Grosberg, A. Y.; Meller, A. *Nat Nano* **2010**, *5*, 160-165.

(15) Kasianowicz, J. J.; Henrickson, S. E.; Weetall, H. H.; Robertson, B. *Analytical Chemistry* **2001**, *73*, 2268-2272.

(16) Venkatesan, B. M.; Bashir, R. *Nat Nano* **2011**, *6*, 615-624.

(17) Saleh, O. A.; Sohn, L. L. *Nano Lett.* **2003**, *3*, 37-38.

(18) Mariam, A.; Aleksandar, I.; Jongin, H.; Phillip, K.; Emanuele, I.; Joshua, B. E.; Tim, A. *Journal of Physics: Condensed Matter* **2010**, *22*, 454128.

(19) Clarke, J.; Wu, H.-C.; Jayasinghe, L.; Patel, A.; Reid, S.; Bayley, H. *Nat Nano* **2009**, *4*, 265-270.

(20) Turner, S. W.; Cabodi, M.; Craighead, H. G. *Physical Review Letters* **2002**, *88*, 128103.

(21) Danelon, C.; Santschi, C.; Brugger, J.; Vogel, H. *Langmuir* **2006**, *22*, 10711-10715.

(22) Craighead, H. *Nature (London, U. K.)* **2006**, *442*, 387-393.

(23) Craighead, H. G. *J. Vac. Sci. Technol., A* **2003**, *21*, S216-S221.

(24) Menard, L. D.; Mair, C. E.; Woodson, M. E.; Alarie, J. P.; Ramsey, J. M. *ACS Nano* **2012**, *6*, 9087-9094.

(25) Tsukahara, T.; Mawatari, K.; Kitamori, T. *Chemical Society Reviews* **2010**, *39*, 1000-1013.

(26) Keyser, U. F.; van Dorp, S.; Lemay, S. G. *Chemical Society Reviews* **2010**, *39*, 939-947.

(27) Pennathur, S.; Baldessari, F.; Santiago, J. G.; Kattah, M. G.; Steinman, J. B.; Utz, P. J. *Analytical Chemistry* **2007**, *79*, 8316-8322.

(28) Menard, L. D.; Ramsey, J. M. *Analytical Chemistry* **2013**, *85*, 1146-1153.

(29) Kim, S. J.; Ko, S. H.; Kang, K. H.; Han, J. *Nature Nanotechnology* **2013**, *8*, 609-609.

(30) Cheng, L.-J.; Guo, L. J. *Chemical Society Reviews* **2010**, *39*, 923-938.

(31) Persson, F.; Tegenfeldt, J. O. *Chem. Soc. Rev.* **2010**, *39*, 985-999.

(32) Levy, S. L.; Craighead, H. G. *Chem. Soc. Rev.* **2010**, *39*, 1133-1152.

(33) Liang, X.; Chou, S. Y. *Nano Letters* **2008**, *8*, 1472-1476.

(34) Reccius, C. H.; Mannion, J. T.; Cross, J. D.; Craighead, H. G. *Physical Review Letters* **2005**, *95*, 268101.

(35) Levy, S. L.; Mannion, J. T.; Cheng, J.; Reccius, C. H.; Craighead, H. G. *Nano Letters* **2008**, *8*, 3839-3844.

(36) Daiguji, H. *Chemical Society Reviews* **2010**, *39*, 901-911.

(37) Han, J.; Craighead, H. G. *Science* **2000**, *288*, 1026-1029.

(38) Woods, L. A.; Gandhi, P. U.; Ewing, A. G. *Analytical Chemistry* **2005**, *77*, 1819-1823.

(39) Bayley, H.; Martin, C. R. *Chemical Reviews* **2000**, *100*, 2575-2594.

(40) Kemery, P. J.; Steehler, J. K.; Bohn, P. W. *Langmuir* **1998**, *14*, 2884-2889.

(41) Kuo, T.-C.; Sloan, L. A.; Sweedler, J. V.; Bohn, P. W. *Langmuir* **2001**, *17*, 6298-6303.

(42) Tas, N. R.; Berenschot, J. W.; Mela, P.; Jansen, H. V.; Elwenspoek, M.; van den Berg, A. *Nano Letters* **2002**, *2*, 1031-1032.

(43) Menard, L. D.; Ramsey, J. M. *Nano Letters* **2011**, *11*, 512-517.

(44) Piotter, V.; Hanemann, T.; Ruprecht, R.; Haußelt, J. *Microsystem Technologies* **1997**, *3*, 129-133.

(45) Becker, H.; Heim, U. *Sensors and Actuators A: Physical* **2000**, *83*, 130-135.

(46) Heckele, M.; Schomburg, W. K. *Journal of Micromechanics and Microengineering* **2004**, *14*, R1.

(47) Abgrall, P.; Low, L.-N.; Nguyen, N.-T. *Lab on a Chip* **2007**, *7*, 520-522.

(48) Schift, H.; David, C.; Gabriel, M.; Gobrecht, J.; Heyderman, L. J.; Kaiser, W.; Köppel, S.; Scandella, L. *Microelectronic Engineering* **2000**, *53*, 171-174.

(49) Utko, P.; Persson, F.; Kristensen, A.; Larsen, N. B. *Lab on a Chip* **2011**, *11*, 303-308.

(50) Liang, X.; Morton, K. J.; Austin, R. H.; Chou, S. Y. *Nano Letters* **2007**, *7*, 3774-3780.

(51) Xia, Q.; Morton, K. J.; Austin, R. H.; Chou, S. Y. *Nano Letters* **2008**, *8*, 3830-3833.

(52) Tegenfeldt, J. O.; Prinz, C.; Cao, H.; Huang, R. L.; Austin, R. H.; Chou, S. Y.; Cox, E. C.; Sturm, J. C. *Analytical and Bioanalytical Chemistry* **2004**, *378*, 1678-1692.

(53) Chantiwas, R.; Hupert, M. L.; Pullagurla, S. R.; Balamurugan, S.; Tamarit-Lopez, J.; Park, S.; Datta, P.; Goettert, J.; Cho, Y.-K.; Soper, S. A. *Lab on a Chip* **2010**, *10*, 3255-3264.

(54) Soper, S. A.; Henry, A. C.; Vaidya, B.; Galloway, M.; Wabuyele, M.; McCarley, R. L. *Analytica Chimica Acta* **2002**, *470*, 87-99.

(55) Hawthorne, S. B.; Yang, Y.; Grabanski, C. B.; Miller, D. J.; Lee, M. L. *Anal. Chem.* **2000**, *72*, 642-643.

(56) Llopis, S. L.; Osiri, J.; Soper, S. A. *ELECTROPHORESIS* **2007**, *28*, 984-993.

(57) Jackson, J. M.; Witek, M. A.; Hupert, M. L.; Brady, C.; Pullagurla, S.; Kamande, J.; Aufforth, R. D.; Tignanelli, C. J.; Torphy, R. J.; Yeh, J. J.; Soper, S. A. *Lab on a Chip* **2014**, *14*, 106-117.

(58) Henry, A. C.; Tutt, T. J.; Galloway, M.; Davidson, Y. Y.; McWhorter, C. S.; Soper, S. A.; McCarley, R. L. *Analytical Chemistry* **2000**, *72*, 5331-5337.

(59) Chan, C. M.; Ko, T. M.; Hiraoka, H. *Surface Science Reports* **1996**, *24*, 1-54.

(60) Chai, J.; Lu, F.; Li, B.; Kwok, D. Y. *Langmuir* **2004**, *20*, 10919-10927.

(61) Wei, S.; Vaidya, B.; Patel, A. B.; Soper, S. A.; McCarley, R. L. *J. Phys. Chem. B* **2005**, *109*, 16988-16996.

(62) Xu, F.; Datta, P.; Wang, H.; Gurung, S.; Hashimoto, M.; Wei, S.; Goettert, J.; McCarley, R. L.; Soper, S. A. *Analytical Chemistry* **2007**, *79*, 9007-9013.

(63) Abgrall, P.; Nguyen, N. T. *Analytical Chemistry* **2008**, *80*, 2326-2341.

(64) Gad-el-Hak, M. *Journal of Fluids Engineering-Transactions of the Asme* **1999**, *121*, 5-33.

(65) Conlisk, A. T. *ELECTROPHORESIS* **2005**, *26*, 1896-1912.

(66) Yuan, Z.; Garcia, A. L.; Lopez, G. P.; Petsev, D. N. *Electrophoresis* **2007**, *28*, 595-610.

(67) Pennathur, S.; Santiago, J. *Anal Chem* **2005**, *77*, 6772 - 6781.

(68) Baldessari, F.; Santiago, J. *Journal of Nanobiotechnology* **2006**, *4*, 12.

(69) Movahed, S.; Li, D. *Electrophoresis* **2011**, *32*, 1259-1267.

(70) Xuan, X. L., D. . *Electrophoresis* **2006**, *27*, 5020-5031.

(71) Oneil, C. E.; Jackson, J. M.; Shim, S.-H.; Soper, S. A. *Analytical Chemistry* **2016**.

(72) Kaji, N.; Ogawa, R.; Oki, A.; Horiike, Y.; Tokeshi, M.; Baba, Y. *Analytical & Bioanalytical Chemistry* **2006**, *386*, 759-764.

(73) Moran, W.; Chi-Chang, C.; Yang, R.-J. *Journal of Chemical Physics* **2010**, *132*, 024701.

(74) Uba, F. I.; Pullagurla, S.; Sirasunthorn, N.; Wu, J.; Park, S.; Chantiwas, R.; Cho, Y.-K.; Shin, H.; Soper, S. A. *Analyst* **2014**, *139*.

(75) Xia, D.; Yan, J.; Hou, S. *Small* **2012**, *8*, 2787-2801.

(76) de la Escosura-Muñiz, A.; Merkoçi, A. *ACS Nano* **2012**, *6*, 7556-7583.

(77) Chantiwas, R.; Park, S.; Soper, S. A.; Kim, B. C.; Takayama, S.; Sunkara, V.; Hwang, H.; Cho, Y.-K. *Chemical Society Reviews* **2011**, *40*, 3677-3702.

(78) Douville, N.; Huh, D.; Takayama, S. *Analytical and Bioanalytical Chemistry* **2008**, *391*, 2395-2409.

(79) Mijatovic, D.; Eijkel, J. C. T.; van den Berg, A. *Lab on a Chip* **2005**, *5*, 492-500.

(80) Duan, C.; Wang, W.; Xie, Q. *Biomicrofluidics* **2013**, *7*, -.

(81) Tegenfeldt, J. O.; Prinz, C.; Cao, H.; Chou, S.; Reisner, W. W.; Riehn, R.; Wang, Y. M.; Cox, E. C.; Sturm, J. C.; Silberzan, P.; Austin, R. H. *Proceedings of the National Academy of Sciences of the United States of America* **2004**, *101*, 10979-10983.

(82) Levy, S. L.; Craighead, H. G. *Chemical Society Reviews* **2010**, *39*, 1133-1152.

(83) Cabodi, M.; Turner, S. W. P.; Craighead, H. G. *Analytical Chemistry* **2002**, *74*, 5169-5174.

(84) Kyo Seon, C.; Seungwook, K.; Haegeun, C.; Joon-Ho, O.; Tae-Yeon, S.; Boo Hyun, A.; Young Keun, K.; Jae Hyoung, P.; Young Rag, D.; Woong, K. *Nanotechnology* **2010**, *21*, 425302.

(85) Tan, S.; Klein, K.; Shima, D.; Livengood, R.; Mutunga, E.; Vladar, A. *Journal of Vacuum Science & Technology B* **2014**, *32*, 06FA01.

(86) Yang, J.; Ferranti, D. C.; Stern, L. A.; Sanford, C. A.; Huang, J.; Ren, Z.; Qin, L.-C.; Hall, A. R. *Nanotechnology* **2011**, *22*, 285310.

(87) Uba, F. I.; Hu, B.; Weerakoon-Ratnayake, K.; Oliver-Calixte, N.; Soper, S. A. *Lab on a Chip* **2015**, *15*, 1038-1049.

(88) Chou, S. Y.; Krauss, P. R.; Renstrom, P. J. *Applied Physics Letters* **1995**, *67*, 3114-3116.

(89) Chou, S. Y.; Krauss, P. R.; Renstrom, P. J. *Journal of Vacuum Science & Technology B* **1996**, *14*, 4129-4133.

(90) Chou, S. Y.; Krauss, P. R. *Microelectronic Engineering* **1997**, *35*, 237-240.

(91) Shao, P. E.; van Kan, A.; Wang, L. P.; Ansari, K.; Bettiol, A. A.; Watt, F. *Applied Physics Letters* **2006**, *88*, -.

(92) Sivanesan, P.; Okamoto, K.; English, D.; Lee, C. S.; DeVoe, D. L. *Analytical Chemistry* **2005**, *77*, 2252-2258.

(93) Li, J.-M.; Liu, C.; Ke, X.; Duan, Y.-j.; Fan, Y.; Li, M.; Zhang, K.-p.; Xu, Z.; Wang, L.-d. *Microsystem Technologies* **2013**, *19*, 1845-1850.

(94) Cheng, E.; Zou, H.; Yin, Z.; Jurcicek, P.; Zhang, X. *Journal of Micromechanics and Microengineering* **2013**, *23*.

(95) Junshan, L.; Hongchao, Q.; Zheng, X.; Chong, L.; Junyao, W.; Liqun, D.; Xi, Z.; Liding, W. *Micro & Nano Letters, IET* **2012**, *7*, 159-162.

(96) Liu, J.; Jin, X.; Sun, T.; Xu, Z.; Liu, C.; Wang, J.; Chen, L.; Wang, L. *Microsystem Technologies* **2013**, *19*, 629-634.

(97) Li, J.-m.; Liu, C.; Ke, X.; Xu, Z.; Duan, Y.-j.; Fan, Y.; Li, M.; Zhang, K.-p.; Wang, L.-d. *Lab on a Chip* **2012**, *12*, 4059-4062.

(98) Zhang, L.; Gu, F.; Tong, L.; Yin, X. *Microfluidics and Nanofluidics* **2008**, *5*, 727-732.

(99) Wu, J.; Chantiwas, R.; Amirsadeghi, A.; Soper, S. A.; Park, S. *Lab on a Chip* **2011**, *11*, 2984-2989.

(100) Cho, Y. H.; Park, J.; Park, H.; Cheng, X.; Kim, B. J.; Han, A. *Microfluidics and Nanofluidics* **2010**, *9*, 163-170.

(101) Lasse, H. T.; Anna, K.; Anders, K. *Nanotechnology* **2008**, *19*, 125301.

(102) Hu, X.; He, Q.; Zhang, X.; Chen, H. *Microfluidics and Nanofluidics* **2011**, *10*, 1223-1232.

(103) Piruska, A.; Nikcevic, I.; Lee, S. H.; Ahn, C.; Heineman, W. R.; Limbach, P. A.; Seliskar, C. J. *Lab on a Chip* **2005**, *5*, 1348-1354.

(104) Khanarian, G.; Celanese, H. *Optical Engineering* **2001**, *40*, 1024-1029.

(105) Baker, D. *Capillary Electrophoresis*; John Wiley and Sons Inc: New York, NY, 1995.

(106) Kirby, B. J.; Hasselbrink, E. F. *ELECTROPHORESIS* **2004**, *25*, 187-202.

(107) Ross, D.; Gaitan, M.; Locascio, L. E. *Analytical Chemistry* **2001**, *73*, 4117-4123.

(108) Erickson, D.; Li, D. *Langmuir* **2003**, *19*, 5421-5430.

(109) Reischl, M.; Stana-Kleinschek, K.; Ribitsch, V. In *Advanced Materials Forum Iii, Pts 1 and 2*, Vilarinho, P. M., Ed., 2006, pp 1374-1378.

(110) Werner, C.; König, U.; Augsburg, A.; Arnhold, C.; Körber, H.; Zimmermann, R.; Jacobasch, H. J. *Colloids and Surfaces A: Physicochemical and Engineering Aspects* **1999**, *159*, 519-529.

(111) Werner, C.; Jacobasch, H. J. *International Journal of Artificial Organs* **1999**, *22*, 160-176.

(112) Minerick, A. R.; Ostafin, A. E.; Chang, H.-C. *ELECTROPHORESIS* **2002**, *23*, 2165-2173.

(113) Oddy, M. H.; Santiago, J. G. *Journal of Colloid and Interface Science* **2004**, *269*, 192-204.

(114) Alkafeef, S. F.; Alajmi, A. F. *Colloids and Surfaces A: Physicochemical and Engineering Aspects* **2006**, *289*, 141-148.

(115) Werner, C.; Körber, H.; Zimmermann, R.; Dukhin, S.; Jacobasch, H.-J. *Journal of Colloid and Interface Science* **1998**, *208*, 329-346.

(116) Sze, A.; Erickson, D.; Ren, L. Q.; Li, D. Q. *Journal of Colloid and Interface Science* **2003**, *261*, 402-410.

(117) Schoch, R. B.; Renaud, P. *Applied Physics Letters* **2005**, *86*, 25311 25311-25313.

(118) Martins, D. C.; Chu, V.; Conde, J. P. *Biomicrofluidics* **2013**, *7*, -.

(119) Stein, D.; Kruithof, M.; Dekker, C. *Physical Review Letters* **2004**, *93*, 035901.

(120) Roy, S.; Yue, C. Y.; Lam, Y. C.; Wang, Z. Y.; Hu, H. *Sensors and Actuators B: Chemical* **2010**, *150*, 537-549.

(121) Vesel, A.; Mozetic, M. *Vacuum* **2012**, *86*, 634-637.

(122) Jorgenson, J. W.; Lukacs, K. D. *Analytical Chemistry* **1981**, *53*, 1298-1302.

(123) Rice, C. L.; Whitehead, R. *The Journal of Physical Chemistry* **1965**, *69*, 4017-4024.

(124) Paul, P. H.; Garguilo, M. G.; Rakestraw, D. J. *Analytical Chemistry* **1998**, *70*, 2459-2467.

(125) Slater, G.; Tessier, F.; Kopecka, K. In *Microengineering in Biotechnology*, Hughes, M. P.; Hoettges, K. F., Eds.; Humana Press, 2010, pp 121-134.

(126) Huang, X.; Gordon, M. J.; Zare, R. N. *Anal. Chem.* **1988**, *60*, 1837-1838.

(127) Mannion, J. T.; Reccius, C. H.; Cross, J. D.; Craighead, H. G. *Biophysical Journal* **2006**, *90*, 4538-4545.

(128) Turner, S. W. P.; Cabodi, M.; Craighead, H. G. *Physical Review Letters* **2002**, *88*, 128103.

(129) Cao, H.; Tegenfeldt, J. O.; Austin, R. H.; Chou, S. Y. *Applied Physics Letters* **2002**, *81*, 3058-3060.

(130) Huh, D.; Mills, K. L.; Zhu, X. Y.; Burns, M. A.; Thouless, M. D.; Takayama, S. *Nature Materials* **2007**, *6*, 424-428.

(131) Matsuoka, T.; Kim, B. C.; Huang, J.; Douville, N. J.; Thouless, M. D.; Takayama, S. *Nano Letters* **2012**, *12*, 6480-6484.

(132) Reisner, W.; Morton, K. J.; Riehn, R.; Wang, Y. M.; Yu, Z.; Rosen, M.; Sturm, J. C.; Chou, S. Y.; Frey, E.; Austin, R. H. *Physical Review Letters* **2005**, *94*, 196101.

(133) Manning, G. S. *Biophysical Journal* **2006**, *91*, 3607-3616.

(134) Orland, H. *Journal De Physique I* **1994**, *4*, 101-114.

(135) Baumgärtner, A. *Polymer* **1982**, *23*, 334-335.

(136) Schaefer, D. W.; Joanny, J. F.; Pincus, P. *Macromolecules* **1980**, *13*, 1280-1289.

(137) Reisner, W.; Beech, J. P.; Larsen, N. B.; Flyvbjerg, H.; Kristensen, A.; Tegenfeldt, J. O. *Physical Review Letters* **2007**, *99*.

(138) Chu, B. *Journal of the American Chemical Society* **1983**, *105*, 5169-5169.

(139) Odijk, T. *Journal of Chemical Physics* **2006**, *125*.

(140) Odijk, T. *Macromolecules* **1983**, *16*, 1340-1344.

(141) Walter, R.; Jonas, N. P.; Robert, H. A. *Reports on Progress in Physics* **2012**, *75*, 106601.

(142) Dai, L.; van der Maarel, J.; Doyle, P. S. *Macromolecules* **2014**, *47*, 2445-2450.

(143) Baumann, C. G.; Smith, S. B.; Bloomfield, V. A.; Bustamante, C. *Proceedings of the National Academy of Sciences* **1997**, *94*, 6185-6190.

(144) Krishnan, M.; Mönch, I.; Schwille, P. *Nano Letters* **2007**, *7*, 1270-1275.

(145) Guo, L. J.; Cheng, X.; Chou, C.-F. *Nano Letters* **2003**, *4*, 69-73.

(146) Takayama, S.; Thouless, M. D.; Huh, D.; Mills, K. L.; Douville, N. J.; Google Patents, 2015.

(147) Angeli, E.; Manneschi, C.; Repetto, L.; Firpo, G.; Valbusa, U. *Lab on a Chip* **2011**, *11*, 2625-2629.

(148) Fanzio, P.; Manneschi, C.; Angeli, E.; Mussi, V.; Firpo, G.; Ceseracciu, L.; Repetto, L.; Valbusa, U. *Scientific reports* **2012**, *2*.

(149) Fanzio, P.; Mussi, V.; Manneschi, C.; Angeli, E.; Firpo, G.; Repetto, L.; Valbusa, U. *Lab on a Chip* **2011**, *11*, 2961-2966.

(150) Manneschi, C.; Angeli, E.; Ala-Nissila, T.; Repetto, L.; Firpo, G.; Valbusa, U. *Macromolecules* **2013**, *46*, 4198-4206.

(151) Manneschi, C.; Fanzio, P.; Ala-Nissila, T.; Angeli, E.; Repetto, L.; Firpo, G.; Valbusa, U. *Biomicrofluidics* **2014**, *8*, 064121.

(152) Han, J.; Craighead, H. G. *Journal of Vacuum Science & Technology A* **1999**, *17*, 2142-2147.

(153) Han, J.; Turner, S. W.; Craighead, H. G. *Physical Review Letters* **1999**, *83*, 1688-1691.

(154) Thamdrup, L. H.; Klukowska, A.; Kristensen, A. *Nanotechnology* **2008**, *19*, 125301.

(155) Bellan, L. M.; Cross, J. D.; Strychalski, E. A.; Moran-Mirabal, J.; Craighead, H. G. *Nano Letters* **2006**, *6*, 2526-2530.

(156) Michaeli, Y.; Ebenstein, Y. *Nat Biotech* **2012**, *30*, 762-763.

(157) Levy-Sakin, M.; Ebenstein, Y. *Current Opinion in Biotechnology* **2013**, *24*, 690-698.

(158) Lam, E. T.; Hastie, A.; Lin, C.; Ehrlich, D.; Das, S. K.; Austin, M. D.; Deshpande, P.; Cao, H.; Nagarajan, N.; Xiao, M.; Kwok, P.-Y. *Nat Biotech* **2012**, *30*, 771-776.

(159) Cao, H.; Hastie, A. R.; Cao, D.; Lam, E. T.; Sun, Y.; Huang, H.; Liu, X.; Lin, L.; Andrews, W.; Chan, S. *GigaScience* **2014**, *3*, 1-11.

(160) Das, S. K.; Austin, M. D.; Akana, M. C.; Deshpande, P.; Cao, H.; Xiao, M. *Nucleic Acids Research* **2010**, *38*, e177.

(161) Shadpour, H.; Musyimi, H.; Chen, J.; Soper, S. A. *Journal of Chromatography A* **2006**, *1111*, 238-251.

(162) Hou, G.; Zhang, H.; Xie, G.; Xiao, K.; Wen, L.; Li, S.; Tian, Y.; Jiang, L. *Journal of Materials Chemistry A* **2014**, *2*, 19131-19135.

(163) Hou, X.; Yang, F.; Li, L.; Song, Y.; Jiang, L.; Zhu, D. *Journal of the American Chemical Society* **2010**, *132*, 11736-11742.

(164) Ali, M.; Yameen, B.; Neumann, R.; Ensinger, W.; Knoll, W.; Azzaroni, O. *Journal of the American Chemical Society* **2008**, *130*, 16351-16357.

(165) Zeng, L.; Yang, Z.; Zhang, H.; Hou, X.; Tian, Y.; Yang, F.; Zhou, J.; Li, L.; Jiang, L. *Small* **2014**, *10*, 793-801.

(166) Weerakoon Ratnayake, K. M.; Uba, F. I.; Oliver-Calixte, N. J.; Soper, S. A. *Analytical Chemistry* **2016**.

(167) Oliver-Calixte, N. J.; Uba, F. I.; Battle, K. N.; Weerakoon-Ratnayake, K. M.; Soper, S. A. *Analytical Chemistry* **2014**, *86*, 4447-4454.

(168) Novak, B. R.; Moldovan, D.; Nikitopoulos, D. E.; Soper, S. A. *The Journal of Physical Chemistry B* **2013**, *117*, 3271-3279.

(169) Xia, K.; Novak, B. R.; Weerakoon-Ratnayake, K. M.; Soper, S. A.; Nikitopoulos, D. E.; Moldovan, D. *The Journal of Physical Chemistry B* **2015**, *119*, 11443-11458.

(170) Liu, J.; Wang, L.; Ouyang, W.; Wang, W.; Qin, J.; Xu, Z.; Xu, S.; Ge, D.; Wang, L.; Liu, C. *Biosensors and Bioelectronics* **2015**, *72*, 288-293.

(171) Wang, C.; Ye, D.-K.; Wang, Y.-Y.; Lu, T.; Xia, X.-H. *Lab on a Chip* **2013**, *13*, 1546-1553.

(172) Yang, S. Y.; Son, S.; Jang, S.; Kim, H.; Jeon, G.; Kim, W. J.; Kim, J. K. *Nano Letters* **2011**, *11*, 1032-1035.

(173) Nunes, P.; Ohlsson, P.; Ordeig, O.; Kutter, J. *Microfluidics and Nanofluidics* **2010**, *9*, 145-161.

(174) *Lab on a Chip* **2002**, *2*, 31N-36N.

(175) Soper, S. A.; Ford, S. M.; Qi, S.; McCarley, R. L.; Kelly, K.; Murphy, M. C. *Analytical Chemistry* **2000**, *72*, 642 A-651 A.

(176) Tsao, C.-W.; DeVoe, D. *Microfluidics and Nanofluidics* **2009**, *6*, 1-16.

(177) Roy, E.; Stewart, G.; Mounier, M.; Malic, L.; Peytavi, R.; Clime, L.; Madou, M.; Bossinot, M.; Bergeron, M. G.; Veres, T. *Lab on a Chip* **2015**, *15*, 406-416.

(178) Soper, S. A.; Hashimoto, M.; Situma, C.; Murphy, M. C.; McCarley, R. L.; Cheng, Y.-W.; Barany, F. *Methods* **2005**, *37*, 103-113.

(179) Lee, J.; Soper, S. A.; Murray, K. K. *Rapid Communications in Mass Spectrometry* **2011**, *25*, 693-699.

(180) Chen, G.; McCarley, R. L.; Soper, S. A.; Situma, C.; Bolivar, J. G. *Chemistry of Materials* **2007**, *19*, 3855-3857.

(181) Battle, K. N.; Jackson, J. M.; Witek, M. A.; Hupert, M. L.; Hunsucker, S. A.; Armistead, P. M.; Soper, S. A. *Analyst* **2014**, *139*, 1355-1363.

(182) Torphy, R. J.; Kamande, J. W.; Tignanelli, C. J.; Moffit, R. A.; Soper, S. A.; Yeh, J. *Journal of Surgical Research*, *179*, 340.

(183) Dharmasiri, U.; Njoroge, S. K.; Witek, M. A.; Adebiyi, M. G.; Kamande, J. W.; Hupert, M. L.; Barany, F.; Soper, S. A. *Analytical Chemistry* **2011**, *83*, 2301-2309.

(184) Xia, H.; Murray, K.; Soper, S.; Feng, J. *Biomedical Microdevices* **2012**, *14*, 67-81.

(185) Njoroge, S. K.; Witek, M. A.; Battle, K. N.; Immethun, V. E.; Hupert, M. L.; Soper, S. A. *Electrophoresis* **2011**, *32*, 3221-3232.

(186) Lacher, N. A.; Garrison, K. E.; Martin, R. S.; Lunte, S. M. *Electrophoresis* **2001**, *22*, 2526-2536.

(187) Dolník, V.; Liu, S.; Jovanovich, S. *Electrophoresis* **2000**, *21*, 41-54.

(188) Kitagawa, F.; Otsuka, K. *Journal of Pharmaceutical and Biomedical Analysis* **2011**, *55*, 668-678.

(189) Pumera, M.; Wang, J.; Grushka, E.; Polsky, R. *Analytical Chemistry* **2001**, *73*, 5625-5628.

(190) Kinsella, A.; Minteer, S. In *Molecular Biomethods Handbook*, Walker, J.; Rapley, R., Eds.; Humana Press, 2008, pp 851-859.

(191) Nilsson, C.; Birnbaum, S.; Nilsson, S. *Journal of Chromatography A* **2007**, *1168*, 212-224.

(192) Osiri, J. K.; Shadpour, H.; Park, S.; Snowden, B. C.; Chen, Z.-Y.; Soper, S. A. *Electrophoresis* **2008**, *29*, 4984-4992.

(193) Osiri, J.; Shadpour, H.; Soper, S. *Analytical and Bioanalytical Chemistry* **2010**, *398*, 489-498.

(194) Lin, C.-H.; Lee, G.-B.; Chen, S.-H.; Chang, G.-L. *Sensors and Actuators A: Physical* **2003**, *107*, 125-131.

(195) Pennathur, S.; Santiago, J. *Anal Chem* **2005**, *77*, 6782 - 6789.

(196) Garcia, A.; Ista, L.; Petsev, D.; O'Brien, M.; Bisong, P.; Mammoli, A.; Brueck, S.; Lopez, G. *Lab on a Chip* **2005**, *5*, 1271 - 1276.

(197) Schoch, R. B.; Bertsch, A.; Renaud, P. *Nano Letters* **2006**, *6*, 543-547.

(198) Menard, L. D.; Ramsey, J. M. *Nano Letters* **2010**, *11*, 512-517.

(199) Uba, F. I.; Pullagurla, S. R.; Sirasunthorn, N.; Wu, J.; Park, S.; Chantiwas, R.; Cho, Y.-K.; Shin, H.; Soper, S. A. *Analyst* **2015**, *140*, 113-126.

(200) Wei, S.; Vaidya, B.; Patel, A. B.; Soper, S. A.; McCarley, R. L. *The Journal of Physical Chemistry B* **2005**, *109*, 16988-16996.

(201) Herr, A. E.; Molho, J. I.; Santiago, J. G.; Mungal, M. G.; Kenny, T. W.; Garguilo, M. G. *Analytical Chemistry* **2000**, *72*, 1053-1057.

(202) Datta, R.; Kotamarthi, V. *Aiche Journal ;* **1990**, *36*, 916 - 926.

(203) Anderson, J. L. *Journal of Colloid and Interface Science* **1985**, *105*, 45-54.

(204) Brotherton, C. M.; Davis, R. H. *Journal of Colloid and Interface Science* **2004**, *270*, 242-246.

(205) Keely, C. A.; van de Goor, T. A. A. M.; McManigill, D. *Analytical Chemistry* **1994**, *66*, 4236-4242.

(206) Ajdari, A. *Physical Review Letters* **1995**, *75*, 755-758.

(207) Fu, L. M.; Lin, J. Y.; Yang, R. J. *Journal of Colloid and Interface Science* **2003**, *258*, 266-275.

(208) Long, D.; Stone, H. A.; Ajdari, A. *Journal of Colloid and Interface Science* **1999**, *212*, 338-349.

(209) Chen, L.; Conlisk, A. T. *Biomedical Microdevices* **2009**, *11*, 251-258.

(210) Rasmussen, J. R.; Stedronsky, E. R.; Whitesides, G. M. *Journal of the American Chemical Society* **1977**, *99*, 4736-4745.

(211) Bates, M., ; Jones, A. S.; Zhuang, X. *Cold Spring Harbor Protocols* **2013**, 498-520.

(212) Patterson, G.; Davidson, M.; Manley, S.; Lippincott-Schwartz, J. *Annual review of physical chemistry* **2010**, *61*, 345-367.

(213) Huang, B.; Wang, W.; Bates, M.; Zhuang, X. *Science (New York, N.Y.)* **2008**, *319*, 810-813.

(214) Huang, B.; Bates, M.; Zhuang, X. *Annual review of biochemistry* **2009**, *78*, 993-1016.

(215) Xu, K.; Shim, S.-H.; Zhuang, X. In *Far-Field Optical Nanoscopy*, Tinnefeld, P.; Eggeling, C.; Hell, W. S., Eds.; Springer Berlin Heidelberg: Berlin, Heidelberg, 2015, pp 27-64.

(216) Gramlich, M. W.; Bae, J.; Hayward, R. C.; Ross, J. L. *Optics Express* **2014**, *22*, 8438-8450.

(217) Lin, H.; Centeno, S. P.; Su, L.; Kenens, B.; Rocha, S.; Sliwa, M.; Hofkens, J.; Uji-i, H. *ChemPhysChem* **2012**, *13*, 973-981.

(218) Kazoe, Y.; Mawatari, K.; Sugii, Y.; Kitamori, T. *Analytical Chemistry* **2011**, *83*, 8152-8157.

(219) Bates, M.; Blosser, T. R.; Zhuang, X. *Physical Review Letters* **2005**, *94*, 108101.

(220) Jones, S. A. S., S. H.; He, J.; Zhuang, X. *Nature Methods* **2011**, *8*, 499-505.

(221) Geisler, C.; Hotz, T.; Schönle, A.; Hell, S. W.; Munk, A.; Egner, A. *Optics Express* **2012**, *20*, 7274-7289.

(222) Shim, S. H. X., C.; Zhong, G.; Babcock, H.; Vaughan, J.; Huang, B.; Wang, X.; Xu, C.; Bi, G. Q.; Zhuang, X. *Proceedings of the National Academy of Sciences of the United States of America* **2012**, *109*, 13978-13983.

(223) Ozgen, O.; Aksoy, E. A.; Hasirci, V.; Hasirci, N. *Surface and Interface Analysis* **2013**, *45*, 844-853.

(224) Novak, B. R.; Moldovan, D.; Nikitopoulos, D. E.; Soper, S. A. *Journal of Physical Chemistry B* **2013**, *117*, 3271-3279.

(225) Xia, K.; Novak, B. R.; Weerakoon-Ratnayake, K. M.; Soper, S. A.; Nikitopoulos, D. E.; Moldovan, D. *Journal of Physical Chemistry B* **2015**, *119*, 11443-11448.

(226) Ahn, C. H.; Jin-Woo, C.; Beaucage, G.; Nevin, J. H.; Jeong-Bong, L.; Puntambekar, A.; Lee, J. Y. *Proceedings of the IEEE* **2004**, *92*, 154-173.

(227) Benetton, S.; Kameoka, J.; Tan, A.; Wachs, T.; Craighead, H.; Henion, J. D. *Analytical Chemistry* **2003**, *75*, 6430-6436.

(228) Bhattacharyya, A.; Klapperich, C. M. *Analytical Chemistry* **2006**, *78*, 788-792.

(229) Bliss, C. L.; McMullin, J. N.; Backhouse, C. J. *Lab on a Chip* **2007**, *7*, 1280-1287.

(230) Choi, S.; Kim, D.; Kwon, T. *Microsystem Technologies* **2009**, *15*, 309-316.

(231) Do, J.; Ahn, C. H. *Lab on a Chip* **2008**, *8*, 542-549.

(232) Pullagurla, S. R.; Witek, M. A.; Jackson, J. M.; Lindell, M. A. M.; Hupert, M. L.; Nesterova, I. V.; Baird, A. E.; Soper, S. A. *Analytical Chemistry* **2014**.

(233) Gulliksen, A.; Anders Solli, L.; Stefan Drese, K.; Sorensen, O.; Karlsen, F.; Rogne, H.; Hovig, E.; Sirevag, R. *Lab on a Chip* **2005**, *5*, 416-420.

(234) Kameoka, J.; Craighead, H. G.; Zhang, H.; Henion, J. *Analytical Chemistry* **2001**, *73*, 1935-1941.

(235) McDonald, J. C.; Duffy, D. C.; Anderson, J. R.; Chiu, D. T.; Wu, H.; Schueller, O. J. A.; Whitesides, G. M. *Electrophoresis* **2000**, *21*, 27-40.

(236) Park, S.; Lee, J.; Yoon, H.; Kim, B.; Sim, S.; Chae, H.; Yang, S. *Biomedical Microdevices* **2008**, *10*, 859-868.

(237) Pu, Q.; Elazazy, M. S.; Alvarez, J. C. *Analytical Chemistry* **2008**, *80*, 6532-6536.

(238) Tan, H. Y.; Loke, W. K.; Tan, Y. T.; Nguyen, N.-T. *Lab on a Chip* **2008**, *8*, 885-891.

(239) Wang, Y.-X.; Zhou, Y.; Balgley, B. M.; Cooper, J. W.; Lee, C. S.; DeVoe, D. L. *Electrophoresis* **2005**, *26*, 3631-3640.

(240) Sia, S. K.; Whitesides, G. M. *Electrophoresis* **2003**, *24*, 3563-3576.

(241) TOPAS. 2011.

(242) Ju Young Shin, J. Y. P., Chenyang Liu, Jiason He, Sung Chul Kim. *Pure and Applied Chemistry* **2005**, *77*, 801-814.

(243) Hwang, S.-J.; Tseng, M.-C.; Shu, J.-R.; Her Yu, H. *Surface and Coatings Technology* **2008**, *202*, 3669-3674.

(244) Roy, S.; Yue, C. Y. *Plasma Processes and Polymers* **2011**, *8*, 432-443.

(245) Tsao, C. W.; Hromada, L.; Liu, J.; Kumar, P.; DeVoe, D. L. *Lab on a Chip* **2007**, *7*, 499-505.

(246) McKnight, A. L.; Waymouth, R. M. *Macromolecules* **1999**, *32*, 2816-2825.

(247) Liu, S.; Yao, Z.; Chen, L.; Dai, B.-B.; Cao, K.; Li, B.-G.; Zhu, S. *Journal of Applied Polymer Science* **2011**, *121*, 707-710.

(248) Seah, M. P.; Dench, W. A. *Surface and Interface Analysis* **1979**, *1*, 2-11.

(249) Mitchell, D. F.; Clark, K. B.; Bardwell, J. A.; Lennard, W. N.; Massoumi, G. R.; Mitchell, I. V. *Surface and Interface Analysis* **1994**, *21*, 44-50.

(250) Powell, C. J.; Jablonski, A.; Tanuma, S.; Penn, D. R. *Journal of Electron Spectroscopy and Related Phenomena* **1994**, *68*, 605-616.

(251) Rabek, B. G. R. a. J. F. *Photodegradation, photooxidation, and photostabilization of polymers, principles and applications*; Wiley: London, New York, 1975.

(252) Oneil, C. E.; Jackson, J. M.; Shim, S.-H.; Soper, S. A. *Analytical Chemistry* **2016**, *88*, 3686-3696.

(253) Mirabella, F. M. *Internal reflection spectroscopy: theory and applications*; Marcel Dekker: New York, 1993.

(254) Yang, T. C. K.; Lin, S. S. Y.; Chuang, T.-H. *Polymer Degradation and Stability* **2002**, *78*, 525-532.

(255) Forsyth, J.; Pereña, J. M.; Benavente, R.; Pérez, E.; Tritto, I.; Boggioni, L.; Brintzinger, H.-H. *Macromolecular Chemistry and Physics* **2001**, *202*, 614-620.

(256) Belu, A. M.; Graham, D. J.; Castner, D. G. *Biomaterials* **2003**, *24*, 3635-3653.

(257) Leech, P. W. *Journal of Micromechanics and Microengineering* **2009**, *19*, 055008.

(258) Pennathur, S.; Santiago, J. G. *Analytical Chemistry* **2005**, *77*, 6782-6789.

(259) Xu, M.; Xu, M. S.; Fujita, D.; Hanagata, N. *Small (Weinheim an der Bergstrasse, Germany)* **2009**, *5*, 2638-2649.

(260) Pienaar, E.; Theron, M.; Nelson, M.; Viljoen, H. J. *Computational Biology and Chemistry* **2006**, *30*, 102-111.

(261) Branton, D. e. a. *Nature Biotechnology* **2008**, *26*, 1146-1153.

(262) Deamer, D. W.; Akeson, M. *Trends in Biotechnology* **2000**, *18*, 147-151.

(263) Meller, A. B., D. *Electrophoresis* **2002**, *23*, 2583-2591.

(264) Storm, A. J. C., H.; Ling, S.; Zandbergen, W.; Dekker, C. *Nature Materials* **2003**, *2*.

(265) Deamer, D. W.; Branton, D. *Accounts of Chemical Research* **2002**, *35*, 817-825.

(266) Heng, J. B.; Aksimentiev, A.; Ho, C.; Marks, P.; Grinkova, Y. V.; Sligar, S.; Schulten, K.; Timp, G. *Biophysical Journal* **2006**, *90*, 1098-1106.

(267) Lagerqvist, J.; Zwolak, M.; Di Ventra, M. *Biophysical Journal* **2007**, *93*, 2384-2390.

(268) Lagerqvist, J.; Zwolak, M.; Di Ventra, M. *Nano Letters* **2006**, *6*, 779-782.

(269) Iqbal, S. M.; Akin, D.; Bashir, R. *Nat Nano* **2007**, *2*, 243-248.

(270) Clarke, J. W., H.C.; Jayasinghe, L.; Patel, A.; Reid, S.; Bayley, H. *Nature Nanotechnology* **2009**, *4*, 265-270.

(271) Reiner, J. E.; Balijepalli, A.; Robertson, J. W. F.; Drown, B. S.; Burden, D. L.; Kasianowicz, J. J. *The Journal of Chemical Physics* **2012**, *137*, -.

(272) Werner, J. H.; Cai, H.; Keller, R. A.; Goodwin, P. M. *Biophysical Journal* **2005**, *88*, 1403-1412.

(273) Geldart, S. E.; Brown, P. R. *Journal of Chromatography A* **1998**, *828*, 317-336.

(274) Li, W.; Moussa, A.; Giese, R. W. *Journal of Chromatography A* **1992**, *608*, 171-174.

(275) Ng, M.; Blaschke, T. F.; Arias, A. A.; Zare, R. N. *Analytical Chemistry* **1992**, *64*, 1682-1684.

(276) Liu, H.; Qi, S.; Zhang, Y.; Huang, A.; Sun, Y. *Journal of High Resolution Chromatography* **1997**, *20*, 242-244.

(277) Uhrová, M.; Deyl, Z.; Suchánek, M. *Journal of Chromatography B: Biomedical Sciences and Applications* **1996**, *681*, 99-105.

(278) Deforce, D. L. D.; Ryniers, F. P. K.; Van den Eeckhout, E. G.; Lemière, F.; Esmans, E. L. *Analytical Chemistry* **1996**, *68*, 3575-3584.

(279) Lecoq, A.-F.; Di Biase, S.; Montanarella, L. *Journal of Chromatography A* **1993**, *638*, 363-373.

(280) Dawson, J. R.; Nichols, S. C.; Taylor, G. E. *Journal of Chromatography A* **1995**, *700*, 163-172.

(281) Ho Row, K.; Griest, W. H.; Maskarinec, M. P. *Journal of Chromatography A* **1987**, *409*, 193-203.

(282) Hong, N.-S.; Shi, L. H.; Jeong, J. S.; Yang, I.; Kim, S.-K.; Park, S.-R. *Analytical and Bioanalytical Chemistry* **2011**, *400*, 2131-2140.

(283) Pennathur, S.; Santiago, J. G. *Analytical Chemistry* **2005**, *77*, 6772-6781.

(284) Xuan, X. *Electrophoresis* **2008**, *29*, 3737-3743.

(285) Garcia, A. L.; Ista, L. K.; Petsev, D. N.; O'Brien, M. J.; Bisong, P.; Mammoli, A. A.; Brueck, S. R. J.; Lopez, G. P. *Lab on a Chip* **2005**, *5*, 1271 - 1276.

(286) Cornelius, M.; Cornelius, M.; Worth, C. G. C.; Kliem, H. C.; Wiessler, M. *Electrophoresis* **2005**, *26*, 2591-2598.

(287) McKeown, A. P.; Nicholas Shaw, P.; Barrett, D. A. *Electrophoresis* **2001**, *22*, 1119-1126.

(288) Muñoz-Muriedas, J.; Barril, X.; López, J. M.; Orozco, M.; Luque, F. J. *Journal of Molecular Modeling* **2007**, *13*, 357-365.

(289) Shih, P.; Pedersen, L. G.; Gibbs, P. R.; Wolfenden, R. *Journal of Molecular Biology* **1998**, *280*, 421-430.

(290) Grossman, P. D. In *Capillary Electrophoresis*; Academic Press: San Diego, 1992, pp 3-43.

(291) Jorgenson, J. W.; Lukacs, K. D. *Science* **1983**, *222*, 266-272.

(292) Napoli, M.; Eijkel, J. C. T.; Pennathur, S. *Lab on a Chip* **2010**, *10*, 957-985.

(293) Stein, D.; van der Heyden, F. H. J.; Koopmans, W. J. A.; Dekker, C. *Proceedings of the National Academy of Sciences* **2006**, *103*, 15853-15858.

(294) M. Xu, D. F. a. N. H. *Small* **2009**, 2638-2649.

(295) Mardis, E. R. *Nature* **2011**, *470*, 198-203.

(296) Xuan, X.; Li, D. *ELECTROPHORESIS* **2006**, *27*, 5020-5031.

(297) Manrao, E. A.; Derrington, I. M.; Laszlo, A. H.; Langford, K. W.; Hopper, M. K.; Gillgren, N.; Pavlenok, M.; Niederweis, M.; Gundlach, J. H. *Nat Biotech* **2012**, *30*, 349-353.

(298) Schneider, G. F.; Dekker, C. *Nat Biotech* **2012**, *30*, 326-328.

(299) Krems, M.; Zwolak, M.; Pershin, Y. V.; Di Ventra, M. *Biophysical Journal* **2009**, *97*, 1990-1996.

(300) Wu, H.-C.; Astier, Y.; Maglia, G.; Mikhailova, E.; Bayley, H. *Journal of the American Chemical Society* **2007**, *129*, 16142-16148.

(301) Huang, S.; He, J.; Chang, S.; Zhang, P.; Liang, F.; Li, S.; Tuchband, M.; Fuhrman, A.; Ros, R.; Lindsay, S. *Nature nanotechnology* **2010**, *5*, 868-873.

(302) Reiner, J. E.; Balijepalli, A.; Robertson, J. W. F.; Drown, B. S.; Burden, D. L.; Kasianowicz, J. J. *The Journal of Chemical Physics* **2012**, *137*, 214903.

(303) Beier, H. T.; Ibey, B. L. *PLoS ONE* **2014**, *9*, e84614.

(304) Saurabh, S.; Maji, S.; Bruchez, M. P. *Optics Express* **2012**, *20*, 7338-7349.

(305) Bigas, M.; Cabruja, E.; Forest, J.; Salvi, J. *Microelectronics Journal* **2006**, *37*, 433-451.

(306) Joseph, D.; Collins, S. In *Instrumentation and Measurement Technology Conference, 2001. IMTC 2001. Proceedings of the 18th IEEE*, 2001, pp 1296-1301 vol.1292.

(307) Cipriany, B. R.; Zhao, R.; Murphy, P. J.; Levy, S. L.; Tan, C. P.; Craighead, H. G.; Soloway, P. D. *Analytical Chemistry* **2010**, *82*, 2480-2487.

(308) Fang Lim, S.; Karpusenko, A.; Sakon, J. J.; Hook, J. A.; Lamar, T. A.; Riehn, R. *Biomicrofluidics* **2011**, *5*, 034106-034106-034108.

(309) Mirsaidov, U.; Timp, W.; Zou, X.; Dimitrov, V.; Schulten, K.; Feinberg, A. P.; Timp, G. *Biophysical Journal* **2009**, *96*, L32-L34.

(310) An, N.; Fleming, A. M.; White, H. S.; Burrows, C. J. *Proceedings of the National Academy of Sciences* **2012**, *109*, 11504-11509.

(311) Kim, Y.; Kim, K. S.; Kounovsky, K. L.; Chang, R.; Jung, G. Y.; dePablo, J. J.; Jo, K.; Schwartz, D. C. *Lab on a Chip* **2011**, *11*, 1721-1729.

(312) Reccius, C. H.; Stavis, S. M.; Mannion, J. T.; Walker, L. P.; Craighead, H. G. *Biophysical Journal* **2008**, *95*, 273-286.